

Analysis and Design Optimization of Offshore Wind Turbine Support Structures



JEPPE BJØRN JØRGENSEN
CHRISTIAN FLØE NISSEN
MASTER THESIS
DESIGN OF MECHANICAL SYSTEMS
AALBORG UNIVERSITY
THE 4TH OF JUNE 2013



**Study Board of Industry and
Global Business Development**
Fibigerstraede 16
DK - 9220 Aalborg East
Phone +45 99 40 93 09
lft@m-tech.aau.dk
www.ses.aau.dk

Title: Analysis and Design Optimization of
Offshore Wind Turbine Support Structures
Semester: Master Thesis
Semester theme: Design of Mechanical Systems
Project period: 1/2 2013 - 4/6 2013
ECTS: 30 ECTS
Supervisors: Erik Lund and Lars Chr. T. Overgaard
Project group: DMS 4, 40.

Christian Fløe Nissen

Jeppe Bjørn Jørgensen

Number printed: 5 Pieces
Pages: 111Pages
Appendix: 13
Enclosures: CD

SYNOPSIS:

The main purpose of this project is to investigate different methods for performing a size optimization of offshore wind turbine support structures w.r.t. fatigue. A generic jacket model and a load case have been provided and it is desired to minimize the mass with fatigue as a constraint by using gradient based optimization methods. The main focus is a development of analytical Design Sensitivity Analysis (DSA) for fatigue constraints with non-proportional load spectra.

A 3D MATLAB FE program is developed in order to perform the structural analysis and determine the accumulated damage.

Small benchmark examples are used to investigate and determine the most suitable methods for damage estimation, optimization, and the analytical DSA.

The DSA is made both numerically and analytically by the adjoint- and direct differentiation method in order to obtain the gradients of the fatigue constraint functions w.r.t. design changes.

Parametric studies and optimization have been performed with the selected methods. A SLP algorithm is used and an adaptive move limit strategy is developed to obtain successful results.

It can be concluded, that the developed methods have a great potential for use in structural optimization since they performed well for the optimization of the jacket structure.

Furthermore, the optimization and analytical DSA of fatigue have proven its potential for future work.

By signing this document, each member of the group confirms participation on equal terms in the process of writing the project. Thus, each member of the group is responsible for the all contents in the project.

Preface

This report is written by Christian Fløe Nissen and Jeppe Bjørn Jørgensen, students at fourth semester of the master program 'Design of Mechanical Systems' at Aalborg University. The project has been supervised by professor Erik Lund and associate professor Lars Chr. T. Overgaard.

Reading Guide

Throughout the report references will be used according to the Harvard method. At the end of the report a full list is compiled with the complete details such as title, authors, ISBN, publisher, etc.

Figures and tables are numbered according to the chapter where they are presented, such that the first figure in Chapter 7 is called Figure 7.1 etc. Figures and tables have captions with explanatory text. Equation references are numbered the same way, but they also include a second index with cross reference to the section number in the chapter. Equations are written inside a parenthesis. Matrices are denoted with a bold symbol and an overline is used for vector notation. The notation is presented in the nomenclature and acronym list before the content of the report.

Throughout the report both global and local coordinate systems are used. The global coordinate system will be denoted using capital letters (X,Y,Z) and a local coordinate system will be written as (x',y',z') .

Appendices are placed at the end of the report, and can be seen as supplementary reporting on applied theories, methods, benchmarks etc. included for the reader to gain more in-depth knowledge on the subject.

A CD is attached to the report containing referenced literature that has been downloaded from the Internet, the report in PDF format as well as MATLAB and ANSYS scripts. The MATLAB scripts includes the DSA and optimization scripts.

Resumé

Formålet med dette projekt er at udvikle en metode til gradientbaseret strukturel optimering med hensyntagen til udmattelse. Der lægges stor vægt på at bestemme designfølsomhederne analytisk, da der i litteraturen ikke er fundet udviklede metoder til dette.

Projektet tager udgangspunkt i simple bjælkemodeller samt en generisk model af et offshore vindmølle-fundament udviklet til vanddybder på mellem 30-50 m med tilhørende lastserier. Et vindmøllefundament designet som en gitterstruktur anvendes, da designet i høj grad er styret af udmattelseskriterier. Der lægges i projektet et stort fokus på valget af metoderne bag modelleringen og optimeringen af fundamentet.

Finite element metoden anvendes til spændingsanalyse i konstruktionen. Til skadesestimeringen anvendes en rainflow optælling af de beregnede spændingsspektre, der sammenholdes med Wöhler-kurver. Der tages desuden hensyn til indflydelsen af middelspændinger i skadesberegningen vha. et Goodman diagram.

Et klassisk optimeringsproblem opstilles, hvor objektfunktionen udgøres af den samlede vægt af konstruktionen og en estimering af skaden medtages som bibetingelse, mens designvariablene udgøres af diametre og tykkelser i rørprofilerne. Et hovedformål med projektet er at bestemme de nødvendige gradienter af både objektfunktionen og skadesbibetingelserne analytisk. Resultatet verificeres med finite difference approksimationer.

I dets nuværende form er der i enkelte tilfælde problemer med den analytiske bestemmelse af design følsomhederne, hvilket skyldes den implementerede datahåndtering.

Indledningsvis afprøves den udviklede optimeringsprocedure på simple bjælkemodeller inden den anvendes på vindmøllefundamentet. Resultaterne viser en vellykket implementering af metoden. Det har vist sig, at der er et stort potentiale for at anvende gradientbaseret optimeringsmetoder

med udmattelse som bibetingelse på fundamentmodellen. Gennem analysen og designoptimeringen af vindmøllefundamentet er det blevet undersøgt og klarlagt, hvilke metoder, som er mest effektive at anvende. Herunder den analytiske følsomhedsanalyse.

Contents

Resumé	vii
Acronyms	1
Nomenclature	3
I Problem Analysis	7
1 Introduction	9
1.1 Problem Definition	11
2 Jacket Structure	15
2.1 Properties of Jacket Structure	15
2.2 Load Case	17
3 Solution Approach	19
3.1 Structural Analysis Part	20
3.2 Optimization Part	22
3.3 Program Development Model	23
II Structural Analysis	25
4 Finite Element Analysis	27
4.1 The 3D Frame Element	27
4.2 Frame Element Stiffness Matrix	28
4.3 Stresses in Cross Sections	29
4.4 Verification of FE Program	34
4.5 Sub Conclusion	34

5	Fatigue	37
5.1	Stress Life Approach	37
5.2	Counting Stresses	38
5.3	Sorting Rainflow Table	39
5.4	Component S-N Curve	41
5.5	Cumulative Damage Model	43
5.6	Benchmark Example of Damage Estimation	43
5.7	Sub Conclusion	46
6	FE Analysis of Jacket Structure	49
6.1	FE Jacket Model	49
6.2	Influence of Sampling the Load Cases	50
6.3	Influence of the Number of Intervals in the Rainflow Counting	53
6.4	Initial Analysis of Jacket Model	56
6.5	Sub Conclusion	58
III	Optimization	59
7	Introduction	61
7.1	Design Variables	61
7.2	Cost Function	62
7.3	Inequality Constraints	63
7.4	Symmetry Conditions	63
8	Design Sensitivity Analysis	65
8.1	DSA of Cost Function	65
8.2	DSA for Constraint Function	66
8.3	Implementation and Bookkeeping	73
8.4	Verification of DSA Method	75
8.5	Comparison of Methods for DSA	80
8.6	Sub Conclusion	80
9	Optimization Methods	81
9.1	Optimization Algorithm	81
9.2	Treatment of Constraint Functions	82
9.3	DSA of Generalized Mean Method	85
9.4	DSA Verification of Generalized Mean Method	85

<i>CONTENTS</i>	xi
9.5 Sub Conclusion	86
10 Optimization Results	87
10.1 Beam with a Single Force Applied	87
10.2 Optimization of Jacket Structure	95
10.3 Sub Conclusion	100
IV Evaluation	101
11 Conclusion	103
12 Discussion	105
Bibliography	109
V Appendix	113
A Load Case	
B Program	
C Finite Element Analysis	
D Modeling Limitations	
E Fatigue	
F DSA Methods	
G Normal Stress Sensitivity	
H Shear Stress Sensitivity	
I Calculation Time	
J Parametric Study of Stress Constraints	
K Deficiencies in the Current Analytical DSA	
L Optimization of Beam with Six Applied Loads	

M Generalized Mean Methods

N CD

Acronyms

AM	Adjoint Method
ANSYS	ANSYS Mechanical APDL v14
BC	Boundary Condition
COG	Center of Gravity
DDM	Direct Differentiation Method
DOF	Degrees of Freedom
DSA	Design Sensitivity Analysis
FBD	Free Body Diagram
FD	Finite Difference
FE	Finite Element
GMM	Generalized Mean Method
LCOE	Levelized Cost of Energy
MATLAB	MATLAB R2010b
MSL	Mean Sea Level
OFD	Overall Finite Difference
OWT	Offshore Wind Turbine

SLP	Sequential Linear Programming
SPD	Structured Program Development
TLT	Total Life Time
TP	Transition Piece

Nomenclature

λ	Lagrange Multiplier	—
ϵ	Normal strain	$\frac{\text{m}}{\text{m}}$
η	Damage	—
μ	Mean value	—
$\bar{\omega}$	Circular eigenfrequency	$\frac{1}{\text{rad}}$
ρ	Density	$\frac{\text{kg}}{\text{m}^3}$
σ	Normal stress	Pa
σ'_f	Fatigue strength at one reversal	Pa
σ_a	Stress amplitude	Pa
σ_m	Stress mean	Pa
σ_u	Ultimate tensile strength, normal	Pa
σ_y	Yield stress, normal	Pa
σ_{NF}	Fully reversed fatigue strength	Pa
τ	Shear stress	Pa
τ_u	Ultimate tensile strength, shear	Pa
θ_x	Rotation around the X-axis	Rad
θ_y	Rotation around the Y-axis	Rad
θ_z	Rotation around the Z-axis	Rad
A	Cross sectional area	m^2
A_0	Amplitude	—
b	Exponent of the S-N curve	—
d	Diameter	m

E	Young's module	Pa
f	Cost Function	—
G	Shear modulus	Pa
g	Constraint Function	—
I	Area moment of inertia	m^4
i	Table columns index	—
I_p	Polar moment of inertia	m^4
I_y	Area moment of inertia around the Y-axis	m^4
I_z	Area moment of inertia around the Z-axis	m^4
j	Design variable index	—
\mathbf{K}	Global stiffness matrix	—
k	Constraint functions index	—
L	Length	m
L_e	Element length	m
\mathbf{M}	Global mass matrix	—
M	Moment	Nm
n	Number of counted cycles	—
N_f	Number of cycles to fatigue failure	—
N_{Amp}	Number of amplitude intervals	—
N_{CS}	Number of cross sectional sample points	—
N_{DOF}	Number of degrees of freedom	—
N_E	Number of Elements	—
N_g	Number of constraint functions	—
N_i	Number of intervals in the rainflow table	—

N_{Mean}	Number of mean intervals	—
N_x	Number of design variables	—
P	Force	N
Q	First moment of inertia	m ³
R	Centerline radius	m
r	Radius	m
RF	Rainflow function	—
\mathbf{T}	Transformation matrix	—
T	Torsional moment	Nm
t	Thickness	m
t_B	Beginning time	s
\bar{U}	Global displacement vector	m
\bar{U}'	Nodal displacement vector	m
u	Displacement in the X-direction	m
V	Shear force	N
v	Displacement in the Y-direction	m
ν	Poisson ratio	—
w_c	Center line deflection	m
x	Design Variable	—
w	Displacement in the Z-direction	m

Part I

Problem Analysis

Chapter 1

Introduction

Since the earliest successful attempts of applying structural design optimization more and more components and structures in engineering have been designed using various optimization schemes. For many products the design is governed by fatigue considerations. Thus, it is evident that including fatigue considerations in optimization may have many benefits. Several previous attempts of including simple fatigue considerations in structural optimization has been made. However, these attempts have often been quite limited in the sense that for instance only proportional load spectra can be used. Thus, the aim of this project is to develop a method for including fatigue considerations in gradient based optimization for larger non-proportional load spectra.

The design of support structures for Offshore Wind Turbine (OWT)s are highly dependent on fatigue loadings. Thus, a generic support structure for an OWT will be used for this project in order to examine the potential of including fatigue considerations in structural optimization on a relevant application.

In contrast to onshore wind turbines, the offshore location calls for a large support structure on which the wind turbine may be erected. So far the majority of offshore wind turbines have been erected on water depths often no deeper than 30 m with support structures being of the gravity based monopile kind. It can be problematic to erect large wind farms along the coast line due to many issues, i.e. coast protection. Thus, the tendency is to erect larger wind farms in deeper waters. For water depths exceeding 30 m support structures of the monopile type is no longer economical or possible due to the large thicknesses of the plates used for the pile. Thus, the use of jacket type support structures are more desirable in order to minimize the Levelized Cost of Energy (LCOE)

for the wind turbine.

In this project a steel jacket support structure, known from the oil and gas industry, for water depths as high as 50 m is examined, see Figure 1.1.



Figure 1.1: Wind turbine with steel jacket support structure [Dong et al., 2012].

The jacket structures are made of hollow steel tubes welded together onshore and transported by ship to the wind farm site. The offshore jacket structure is affected by both wind and wave loads. The dynamic response of the jacket structures is larger when they are used for support structure for wind turbines, than when used for oil and gas platforms. This is due to the significantly larger influence of the alternating wind loads, which makes fatigue considerations critical in the design process. The estimated service life of wind turbines is commonly 20 years or higher. Naturally, the service life of the support structure cannot be lower than the estimated service life of the wind turbine.

By the use of gradient based optimization methods in collaboration with fatigue considerations, an optimum support structure is sought, optimum

being the lightest structure, and implicitly the cheapest solution, with the lowest LCOE impact. The optimized jacket structure will have a significant impact on lowering the LCOE of the OWT for deeper seas since the cost of the support structure may be as high as 20% of the LCOE dependent on the water depth and the design concept [Frantzis et al., 2013]. A lighter support structure may also allow for an easier transportation and on-site mounting.

1.1 Problem Definition

Due to the large number of challenging tasks and the limited time frame for the project some main focus points have been chosen. These are highlighted in the following.

The project will aim at developing a method for structural design optimization with regards to fatigue considerations. The method will be developed using smaller models before it is applied to the full jacket structure to examine the potential of the method. In order to lower the LCOE of the OWT it is chosen to minimize the weight of the jacket structure with fatigue and manufacturing constraints. The overall aim for the structural optimization is to obtain a design where all the evaluated points in the structure are at the fatigue limit. Hence, the material in the structure has been minimized and distributed in the most efficient way. The manufacturing constraints means, that symmetry conditions are enforced on the jacket structure. A damage estimation of the individual structural elements in the jacket support structure must be performed in order to verify, that the fatigue strength is sufficient.

One objective of the project is to use and implement Finite Element (FE) based methods for the stress analysis of the jacket structure. This will act as the base for the design optimization. The outer diameters and wall thicknesses of the circular hollow tubes, used throughout the report, are the set design variables. Only linear elastic materials and small deformations are allowed for the analysis. Thus, a linear FE model can be created and used for the analysis.

The developed method must be applicable on real life structures with non-proportional load series. To examine this, the method is applied on a generic jacket support structure. A number of requirements are set for the optimized jacket structure in order to evaluate the usability of the developed method on an actual structure.

The jacket structure must be:

- Designed for low weight.
- Designed using gradient based optimization methods.
- Designed using fatigue constraints.
- Symmetric in design.
- Able to withstand the applied loads for a service life of 20 years.
- Analyzed by a developed FE program based on 3D frame elements.

The fulfillment of the above requirements will determine the applicability of the developed method.

The use of gradient based optimization methods in collaboration with fatigue constraints is still under development. The potential of this optimization method may be large, but challenges are to make the optimization functional, efficient, and accurate. During a literature study the topic is examined, see Zhou et al. [2009] or Holmberg [2013], and it is found, that no one has developed and published analytical Design Sensitivity Analysis (DSA) of fatigue constraints with non-proportional load spectra. Thus, the main focus of this project is to develop an efficient analytical DSA for fatigue constraints with a non-proportional load spectra. This project serves as one of the first attempts to develop an efficient analytical DSA.

Thus, it will be the goal of this project to find the most suitable methods for:

- The damage estimation.
- The set up of fatigue constraints.
- The analytical design sensitivity analysis of fatigue constraints.
- The optimization with fatigue constraints.

The list serves as a an overview of the problem definition, which will be evaluated as a part of the conclusion. The purpose of using the different methods is to find an efficient procedure for determining an optimized structure subjected to fatigue constraints. Computational time and solution accuracy will be used to compare the different applied methods and to choose

the best suited method for the overall optimization procedure. The methods must be benchmarked in order to prove that they are functional and accurate.

1.1.1 Delimitations

Environmental effects on the support structure from the harsh sea environment will not be considered in the project. Furthermore, fatigue strength of the welded details in the structure is left unexamined. The effects of temperature, radiation, buckling, impact, creep, relaxation, corrosion, and abrasion are disregarded as well.

Chapter 2

Jacket Structure

A generic steel jacket support structure designed for a 5 MW OWT and a single load case are provided for the project. These are presented in this chapter and described in Vorpahl et al. [2011]. Lastly, an initial treatment of the provided load spectra is clarified. Appendix A supports this chapter.

2.1 Properties of Jacket Structure

The jacket structure is designed for a water depth of 50 m and has a total height of 70.15 m. It rests on four piles of length 45 m rammed into the sea bed. A conical tower of height 68 m, representing a wind turbine tower is mounted on the jacket structure via a concrete Transition Piece (TP).

The parts can be seen on Figure 2.1a. The corresponding properties for the coloured parts on Figure 2.1b can be found in Table 2.1. The jacket structure is assembled from hollow steel tubes with circular cross sections, and x- and k-connections, which are welded together. Numbering and name conventions of the legs, k-joints, and x-joints can be seen on Figure 2.2, where the sides and the braces of the jacket structure are named as well.

Property set	Component	Color	Outer diameter [m]	Thickness [mm]
1	x- and mud braces	gray	0.8	20
2	leg at lowest level	red	1.2	50
3	leg 2 to 4	blue	1.2	35
4	leg crossing TP	orange	1.2	40

Table 2.1: Properties of jacket members.

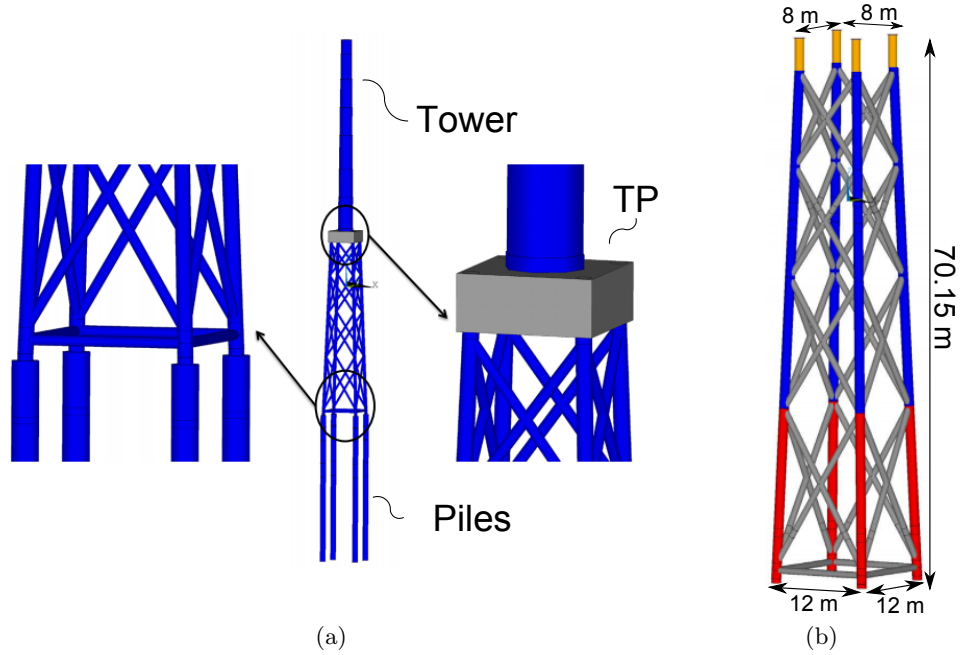


Figure 2.1: (a) Tower, piles, and TP, (b) jacket structure with measurements [Vorpahl et al., 2011].

The properties for the steel jacket structure are given by [Vorpahl et al., 2011] as:

$$\rho = 7850 \text{ kg/m}^3 \quad E = 2.1e11 \text{ Pa} \quad \nu = 0.3 \quad (2.1.1)$$

A global Cartesian coordinate system is introduced on Figure 2.2. It is positioned 20.15 m below the top of the TP according to the Z-coordinate, which is defined in the upward direction. The origin is placed at the Mean Sea Level (MSL) in the centerline of the tower. The X-axis is normal to the sides 'S2' and 'S4' seen in Figure 2.2, and its positive direction is towards side 'S4'. The mudline is located at $Z = -45$ m.

The jacket structure includes a concrete TP, which connects the jacket structure to the wind turbine tower, see Figure 2.1a. The TP is a rigid concrete block with a mass of 666 t and a size of $4 \times 9.6 \times 9.6$ m. It is positioned on the top of the jacket structure, where four additional steel members (coloured orange on Figure 2.1b) are embedded into the concrete. The jacket structure model is a cantilever frame structure, which is anchored at the mudline, providing the Boundary Condition (BC) for the model.

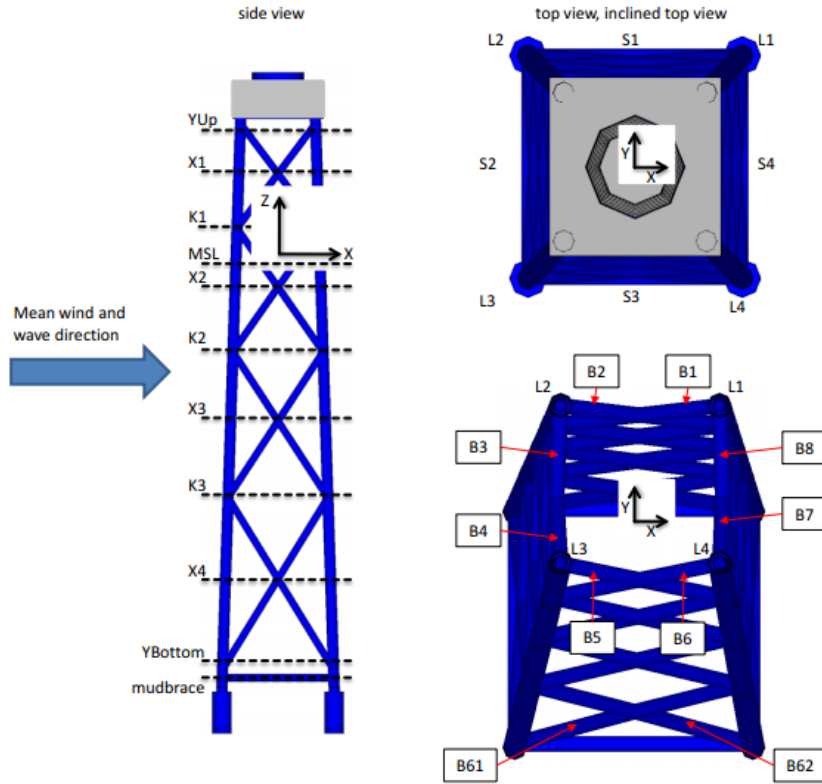


Figure 2.2: Global coordinate system located at MSL and name convention for the sides, [Vorpahl et al., 2011].

2.2 Load Case

The main loads on the jacket support structure are caused by the wind and the waves. These loads are obtained by performing a multi body analysis of the entire OWT assembly using the software HAWC2 from the Risø National Laboratory. The results from this multi body analysis are provided by the DTU Wind Energy Group and contain the forces P_x and P_y , and the moments M_x and M_y as seen in Appendix A. These are applied in the center of the TP.

The loads obtained from the multi body analysis are highly dependent on the geometry of the jacket structure, since this affects the mass, damping, and stiffness of the model and thus the dynamical response. As a result, the loads on the model are design-dependent and will change for each geometry change. This means, that the multi body analysis should be rerun for every design

change made during the optimization iterations yielding an updated load case. The effect of the design changes on the obtained loads is however disregarded in the project, since a full coupling between the fatigue optimization and the multi body analysis is impractical for the project purpose.

The obtained load case is calculated for a finite period of time i.e. 15 minutes. Thus, the full load-history for 20 years must be assembled from several different finite time load cases applied after each other. This will yield a rough estimation of the applied loads during the 20 years time period. Note, the wind turbine is assessed to operate only 80% of the time, [Planning, 2013], which affects the estimation of the Total Life Time (TLT) damage.

2.2.1 Load Case Reduction

Load series reduction can be a helpful tool, but due to the limited time frame it has not been examined in this project. Thus, only a simple reduction of the load spectra will be made by applying a smoothing operation of the load spectra. This is illustrated on Figure 2.3. The smoothing operation can be made, because the estimated damage will remain unchanged, since only the load amplitude and its corresponding mean between two turning points contribute to the damage. Thus, the load spectra used in this project will only consist of turning points as seen from Figure 2.3.

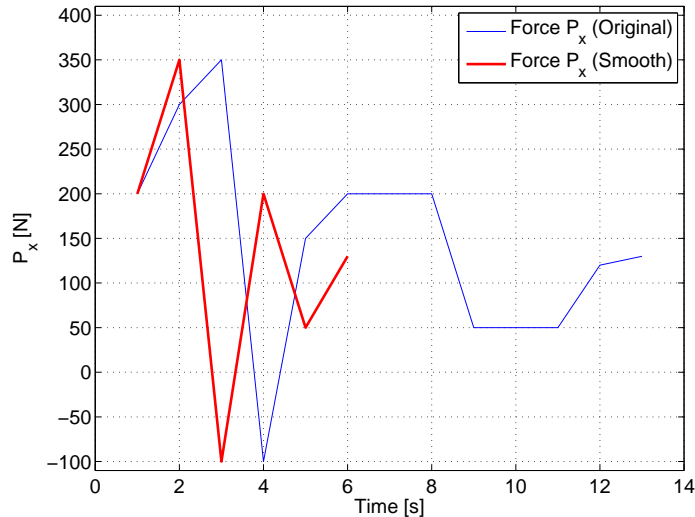


Figure 2.3: Example of a load spectrum and the corresponding smoothed load spectra.

Chapter 3

Solution Approach

The solution strategy of the project is presented in the following, which may be seen as a guide to the content of the report. This chapter is supported by Appendix B.

As mentioned in Chapter 1 the purpose of the project is to determine the most efficient procedures and methods for determining the lightest possible design able to withstand an applied load spectra. The fatigue life of a structure is highly affected by the resulting stress amplitude from the applied dynamic loading. Thus, in order to assess the fatigue life, a stress analysis and an accumulated damage estimation must be performed. The stress analysis and the damage estimation are joined in the part of the report known as the Structural Analysis Part, see Figure 3.1.

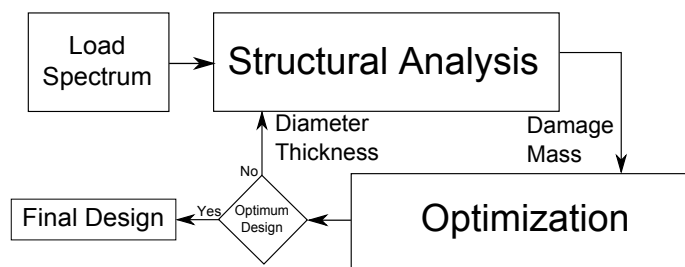


Figure 3.1: Solution strategy for the project.

The Optimization Part has the purpose of clarifying the methods and results for mass minimization, without compromising the desired service life.

However, the main focus in this part is to develop the analytical DSA of the fatigue constraint for a spectra with non-proportional loads.

The FE model is changed in each iteration of the optimization routine, resulting in an altered damage. As mentioned, the aim for the structural optimization is to obtain the lightest possible design, where all the evaluated points in the structure is below the fatigue limit. Such a design will yield the global optimum solution, but may be hard or even impossible to achieve in practice. Instead a local optimum solution will be sought, where some evaluated points will be close to the fatigue limit.

The full optimization procedure, including the FE structural analysis, will be conducted by the use of several MATLAB R2010b (MATLAB) scripts and sub-functions, which can be found on the enclosed CD, Appendix N.

The two major parts of the project, the Structural Analysis Part and the Optimization Part, will be examined individually in more details in the following sections.

3.1 Structural Analysis Part

One of the main tasks of the Structural Analysis Part is to accurately determine the stresses in the used FE model as well as estimating the accumulated fatigue damage from the stress results. A 2D FE beam analysis program has been provided by Erik Lund. The provided 2D beam program is rewritten for the analysis of 3D models. This is done by expanding the 2D beam element formulation with three additional nodal DOFs to the implemented 3D element formulation. The 3D frame element is developed based on Bernoulli-Euler beam theory.

Up to six different load cases are examined in each loop of the structural analysis. These are a unit load applied in the positive X-, positive Y-, and positive Z-direction as well as a positive unit moment around the X-, Y-, and Z-axis. Each load case is examined individually and the global stiffness matrix is reused in the six load cases. The result is six sets of global displacements for each DOF in the model. Each displacement set, obtained by a unit load, is scaled according to the applied load spectra. By superimposing the scaled displacements, the actual displacement field for a given load sample point is determined. The model stresses may be found based on this obtained set of global displacements. Note, this approach requires linearity of the FE model.

Each load spectrum is sampled in a finite number of load sample points. Thus, one set of global displacements is obtained for each load sample point. This results in a stress spectrum for each cross sectional sample point of the FE model. These are counted by the rainflow method to give a number of mean and amplitude stresses, and placed into a sorted rainflow table to make the approach efficient w.r.t damage estimation and DSA. The accumulated damage in each cross sectional sample point may be determined by the use of Palmgren-Miner's damage rule. The Structural Analysis Part is illustrated in Figure 3.2.

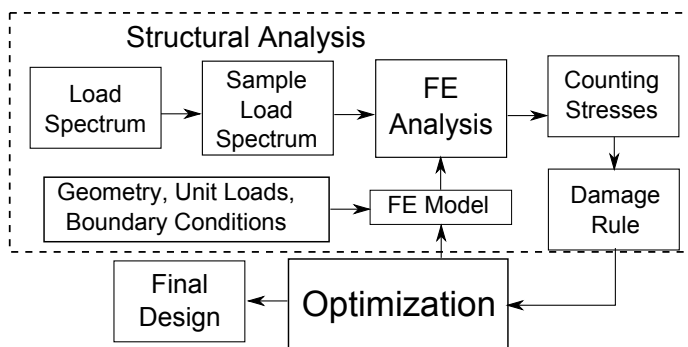


Figure 3.2: Solution strategy for the Structural Analysis Part.

In this project, simple beam models and the generic jacket structure, both made from circular hollow profiles, will be used. Thus, the geometric inputs to the structural analysis is the outer diameter and the wall thickness of each frame element in the FE model. The output is a predicted damage value in a predetermined number of sample points in the cross sections of the beams as well as the mass of each beam. This means a FE analysis of the structure, a sampling of the applied load spectrum, a counting of the resulting stress spectrum, and an accumulated damage estimation, are required, as illustrated in the dotted-line box on Figure 3.2. Different methods for the damage estimation will be applied in order to determine the most suited method. The Structural Analysis Part will however consist of the same basic subparts illustrated in Figure 3.2 regardless of the applied method in the individual subparts.

reduce the number of constraints.

Initially, small simple benchmark examples will be used to verify the method for the optimization using fatigue inequality constraints. After this the method is applied on the jacket structure to examine the potential of the developed method on a real life structure. The use of smaller benchmark examples will ease the validation, since the optimum solution may be known prior to the optimization, due to the use of parametric studies.

An optimized design should always be analyzed thoroughly in a final validation before put into production. However, a final validation of the optimized models will not be attempted in this project, since the focus is on the developed method.

3.3 Program Development Model

The MATLAB FE program is developed based on the method known as Structured Program Development (SPD), which is presented in Soerensen et al. [1988]. The method is a part of the product development model, which can be seen on Figure 3.4.

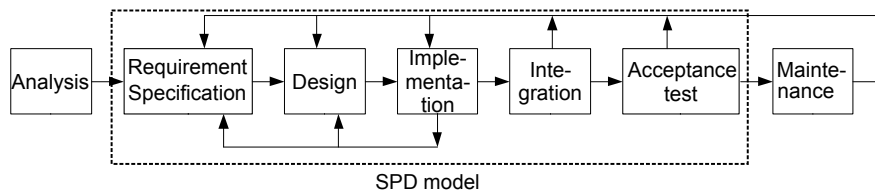


Figure 3.4: Illustration of the parts contained in the SPD model.

The Requirements are determined in the problem definition, section 1.1. The term 'Design' covers the realization of the requirements and partitioned into sub processes. Every process is split into sub-modules, with specific requirements. Implementation covers the module design, module development, and module testing. The integration contains the coupling of modules, where processes are linked one by one and tested in connection with other processes. The acceptance tests serves as a verification of the requirements.

The method can be used during the development of all the parts of the MATLAB FE program, but the method is only exemplified for the damage estimation including the FE model on Figure 3.5.

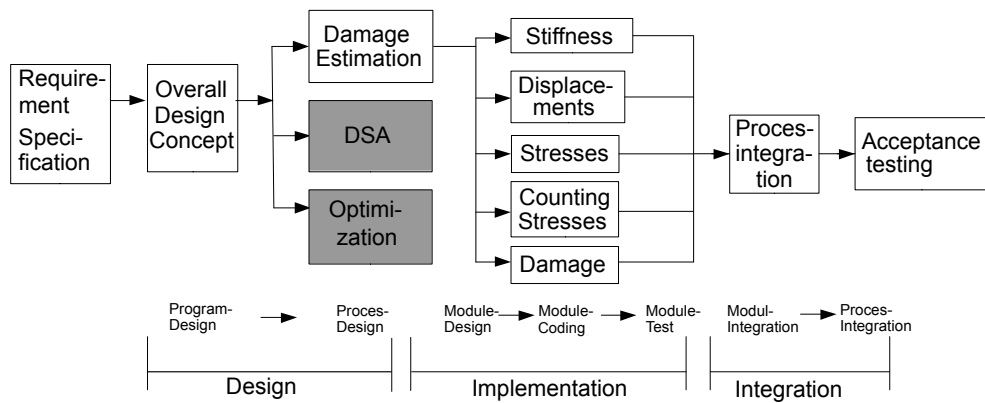


Figure 3.5: SPD model for the damage estimation in the project.

The modules stiffness, displacements, stresses, counting stresses, and damage are tested and verified individually before they are combined and the full program is tested. Thus, the method may ease the debugging on the larger scale since sub-functions may be verified individually. The modules are presented and verified continuously throughout the report. A full list of program functionalities can be found in Appendix B.

Part II

Structural Analysis

Chapter 4

Finite Element Analysis

A FE beam program is developed for 3D stress analysis of the used models. The element formulation, assumptions, governing equations, and the determination of stresses in the cross sections will be described briefly in the following and details may be found in Appendix C. The bookkeeping will not be explained in details. The MATLAB FE program will be validated using benchmark examples analyzed in ANSYS Mechanical APDL v14 (ANSYS) as well as analytical results. Modeling limitations are examined in Appendix D.

4.1 The 3D Frame Element

The developed MATLAB FE program is an expansion of a 2D beam analysis code provided at the project start. In order to be applicable for the analysis of 3D models like the generic jacket structure, the original program is modified by including a 3D frame element in the code.

The element implemented in the MATLAB FE program is a two-node 3D frame element. This element has six DOFs in each node:

$$\bar{U}'_l = [u'_l \ v'_l \ w'_l \ \theta'_{xl} \ \theta'_{yl} \ \theta'_{zl}]^T \quad \text{for } l = 1, 2 \quad (4.1.1)$$

where l is the node number. These are three translations and three rotations as illustrated on Figure 4.1.

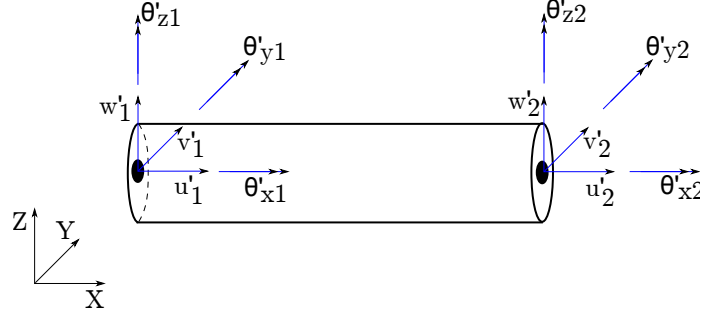


Figure 4.1: Positive directions of the DOFs of the two-node 3D frame element.

The stiffness of the 3D frame element can be seen as a combination of contributions from a bar and a beam element since it contains both axial, torsional, and bending stiffnesses. The local stiffness matrix for the 3D frame element is derived in Appendix C.

4.2 Frame Element Stiffness Matrix

The local stiffness matrix is a 12x12 matrix given by the two nodes with six DOFs each. By setting up the 12 equations linking the nodal displacements to the nodal forces and moments, the 3D frame element stiffness matrix in local coordinate system, \mathbf{K}'_e can be obtained, see Figure 4.2.

$$\begin{Bmatrix} P'_{x1} \\ P'_{y1} \\ P'_{z1} \\ M'_{y1} \\ M'_{z1} \\ P'_{x2} \\ P'_{y2} \\ P'_{z2} \\ M'_{y2} \\ M'_{z2} \end{Bmatrix} = \begin{bmatrix} \frac{AE}{L_e} & 0 & 0 & 0 & 0 & 0 & -\frac{AE}{L_e} & 0 & 0 & 0 & 0 & 0 \\ \frac{12EI_x}{L_e^3} & 0 & 0 & 0 & 0 & \frac{6EI_x}{L_e^2} & 0 & -\frac{12EI_x}{L_e^3} & 0 & 0 & 0 & 0 \\ 0 & \frac{12EI_y}{L_e^3} & 0 & -\frac{6EI_y}{L_e^2} & 0 & 0 & 0 & 0 & -\frac{12EI_y}{L_e^3} & 0 & -\frac{6EI_y}{L_e^2} & 0 \\ 0 & 0 & \frac{GJ}{L_e} & 0 & 0 & 0 & 0 & 0 & 0 & -\frac{GJ}{L_e} & 0 & 0 \\ 0 & 0 & 0 & \frac{4EI_y}{L_e} & 0 & 0 & 0 & 0 & \frac{6EI_y}{L_e^2} & 0 & \frac{2EI_y}{L_e} & 0 \\ 0 & 0 & 0 & 0 & \frac{4EI_z}{L_e} & 0 & 0 & -\frac{6EI_z}{L_e^2} & 0 & 0 & 0 & \frac{2EI_z}{L_e} \\ \hline \text{Sym.} & & & & & & \frac{AE}{L_e} & 0 & 0 & 0 & 0 & 0 \\ & & & & & & 0 & \frac{12EI_x}{L_e^3} & 0 & 0 & 0 & -\frac{6EI_x}{L_e^2} \\ & & & & & & 0 & 0 & \frac{12EI_y}{L_e^3} & 0 & \frac{6EI_y}{L_e^2} & 0 \\ & & & & & & 0 & 0 & 0 & \frac{GJ}{L_e} & 0 & 0 \\ & & & & & & 0 & 0 & 0 & 0 & \frac{4EI_y}{L_e} & 0 \\ & & & & & & 0 & 0 & 0 & 0 & 0 & \frac{4EI_z}{L_e} \end{bmatrix} \begin{Bmatrix} u'_1 \\ v'_1 \\ w'_1 \\ \theta'_{x1} \\ \theta'_{y1} \\ u'_2 \\ v'_2 \\ w'_2 \\ \theta'_{x2} \\ \theta'_{y2} \\ \theta'_{z2} \end{Bmatrix}$$

Figure 4.2: The local stiffness matrix of a 3D frame element.

This gives the element equilibrium:

$$\mathbf{K}'_e \cdot \bar{\mathbf{U}}' = \bar{\mathbf{P}}'$$

which is given in the local coordinate system. By the use of the transformation matrix from Appendix C.1, transformations between global and local

coordinate systems can be carried out by:

$$\mathbf{K}_e = \mathbf{T}_{12 \times 12}^T \mathbf{K}'_e \mathbf{T}_{12 \times 12} \quad (4.2.1)$$

The global stiffness matrix may be assembled by several local 12x12 stiffness matrices which have been transformed using equation (4.2.1). Transformed local stiffness terms affecting the same global DOF are added in the global stiffness matrix. Knowing the applied force on the structure and having assembled the global stiffness matrix enables a determination of the global displacements from:

$$\mathbf{K}\bar{\mathbf{U}} = \bar{\mathbf{P}} \quad (4.2.2)$$

This is known as the global equilibrium equation. Stresses in the elements may be determined from the found displacements as seen in the following section.

4.3 Stresses in Cross Sections

The stresses must be examined in various sample points in the cross section in order to use the FE program to estimate the damage in the jacket structure. The normal and shear stresses are examined individually and evaluated in the local element coordinate system in the following.

The shear and normal stresses in the FE program are computed in a number of cross sectional sample points, N_{CS} provided by the user. The sampling in the cross section is conducted along the dashed lines seen in Figure 4.3a. These are defined from the α -angle given by $\alpha = \frac{360^\circ}{N_{CS}}$. $\alpha_{Initial}$ is an angle offset value shown on Figure 4.3a, and it is used to rotate all the cross sectional sample points by an input value provided by the user.

This approach will not guarantee that a sample point is placed in the exact spot of the highest damage on the element cross section. This is illustrated in Figure 4.3b for a cantilevered beam example with six tip loads. As N_{CS} increases the chance of finding the maximum damage on the cross section increases as well. However, the calculation time is increased as the number of cross sectional sample points increases. The suitable number of cross sectional sample points will be problem dependent.

In order to calculate the damage, a suitable number of cross sectional sample points must be chosen. This choice is a compromise of computational time and the needed number of sample points on the cross section. The

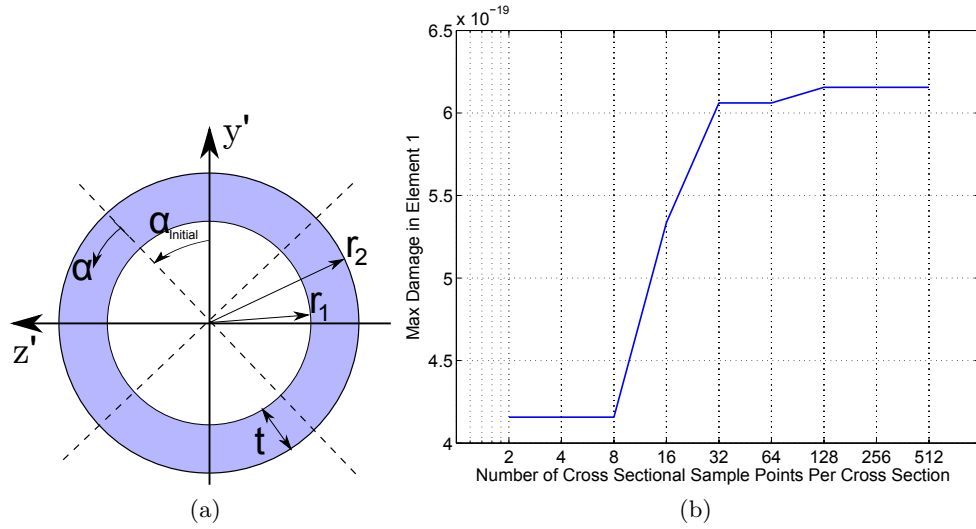


Figure 4.3: (a) The cross section of a frame element with four cross sectional sample points, illustrated by dashed lines, evenly distributed starting from the y' -axis. (b) The influence of the number of cross sectional sample points, N_{CS} on the maximum damage.

bookkeeping for the cross sectional sampling points is shown in Table 4.1 for four sample points in the cross sections.

Element	Element 1								Element 2							
	Node 1				Node 2				Node 1				Node 2			
α_i [deg.]	0	90	180	270	0	90	180	270	0	90	180	270	0	90	180	270
σ_i																
τ_i																

Table 4.1: Sampling stresses in a cross section containing four sample points evenly distributed with $\alpha_{Initial} = 0$.

Having clarified how the cross sectional sample points are determined and how they are handled in the bookkeeping, the stresses in the cross section may be found. The details of the stress calculation can be found in Appendix C. Note, only the final equations for the stress calculations are presented in this section. First, the normal stress in the cross sectional sample points is examined.

4.3.1 Normal Stresses

Both the axial and the bending stress contribute to the normal stress in the cross sectional sample points. The axial stress is determined from the axial force and the bending stresses are determined from an applied bending moment or transverse force. For details see Appendix C.2. The normal stress in each cross sectional sample point may be determined by a superposition of the normal stresses:

$$\sigma(d, t) = \sigma_{axial}(d, t) - \frac{M_y \cdot d}{2 \cdot I_y(d, t)} - \frac{M_z \cdot d}{2 \cdot I_z(d, t)} \quad (4.3.1)$$

Next, the determination of the shear stresses is examined.

4.3.2 Shear Stresses

Three loads contribute to the shear stress in each cross sectional sample point. These are the y' - and z' -shear forces as well as the torsional moment. The procedure for determining the shear stresses in a circular hollow cross section can be read in detail in Appendix C.3. The total shear stress in each cross sectional sample point may be determined by a superposition of the y' - and z' -shear stress:

$$\begin{aligned} \tau_y(d, t, \alpha, \alpha_{Initial}) &= \frac{V_y \cdot Q_y(d, t, \beta)}{I_z(d, t) \cdot 2t} + \tau_{Ty}(\alpha + \alpha_{Initial}) \\ \tau_z(d, t, \alpha, \alpha_{Initial}) &= \frac{V_z \cdot Q_z(d, t, 90^\circ - \beta)}{I_y(d, t) \cdot 2t} + \tau_{Tz}(\alpha + \alpha_{Initial}) \\ \tau_{tot}(d, t, \alpha, \alpha_{Initial}) &= \tau_y(d, t, \alpha, \alpha_{Initial}) + \tau_z(d, t, \alpha, \alpha_{Initial}) \end{aligned} \quad (4.3.2)$$

where β is used to determine the first area moment of inertia and defined in the interval $0 \leq \beta \leq \frac{\pi}{2}$, see Figure C.4a.

The sign on the shear force will determine whether the shear stresses from the two shear forces are added or not, since the shear force is the only parameter in equation (C.3.3) which may be negative.

In order to examine the shear stress distribution over the cross section, four cases are set up. Unit shear loads with changing signs are used. This is exemplified by using the properties from row number one in Table 2.1. The results can be seen on Figure 4.4.

For the case where V_y and V_z are in the same direction, the maximum shear stress are in $45^\circ + i \cdot 90^\circ$, where i is zero or a positive integer. For the case where V_y and V_z are in the opposite direction, the shear stress increases/decreases

almost linearly, and it is fluctuating between the maximum and minimum value of one of the shear components (τ_y or τ_z). Thus, it can be concluded that the worst case occurs when the sign on the shear forces are equal.

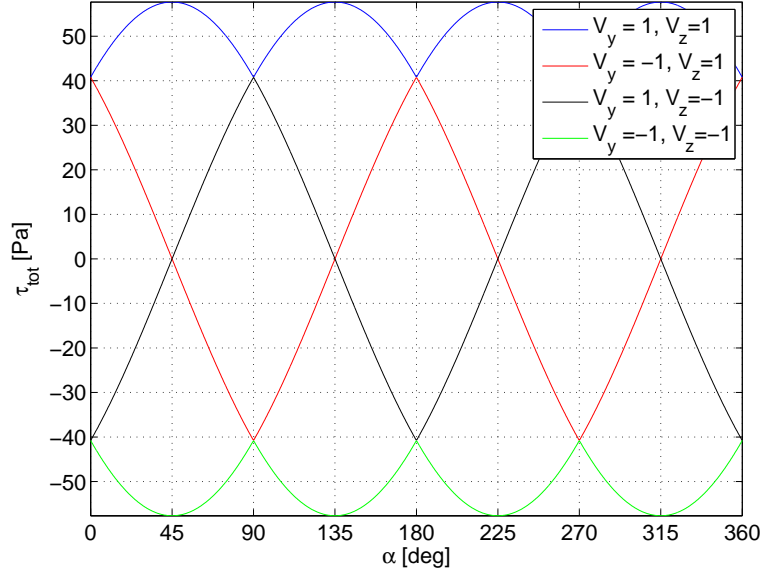


Figure 4.4: Shear stresses in a hollow circular cross section as a function of the angle α with $\alpha_{Initial} = 0$.

Having found the stresses in the cross sectional sample points, the FE code is verified in the following section.

4.3.3 Scope of Application for the FE Model

In the following it is examined for which design variables the FE-model is valid. The beam element used for the FE-analysis is based on Bernoulli-Euler beam theory. Thus, errors in the obtained results must be expected for short stubby beams. The diameter to length ratio, below which errors will be introduced in the results, is examined in Appendix D. For convenience the main graph of Appendix D is reprinted on Figure 4.5a. A cantilever prismatic beam containing the frame elements is used for the investigation, and the tip deflection is determined by Bernoulli-Euler and Timoshenko beam theory in order to identify the limitations of the Bernoulli-Euler theory. The diameter and length are varied for a fixed thickness of 0.02 m. It is concluded, that a

relationship of 1/10 should be kept between the diameter and the length of each frame element in order not to violate the Bernoulli-Euler assumptions, see Figure 4.5a. From Figure D.2b it can be concluded, that the thickness has only a minor influence with regards to maintaining the Bernoulli-Euler assumptions.

A limitation is introduced for the thicknesses as well. However, this limitation is not caused by the Bernoulli-Euler beam theory, but is a result of the formula used to approximate the first area moment of inertia, Q seen in equation (C.3.6) in Appendix C.3. The formula approximating Q is only valid for small tube thicknesses relative to the diameter. In order to examine when the approximate formula will start to yield unreliable results a test example is set up. An exact analytical solution is available for a full half circle. Thus, the deviation between the case of a full half circle by the approximate and exact analytical solution for Q can be obtained. The relative deviation of the approximate and exact analytical solution for Q is shown on Figure 4.5b. Based on Figure 4.5b the limit of the thickness to diameter ratio is set to 1/10, which will introduce an error on less than one percent in the calculated results.

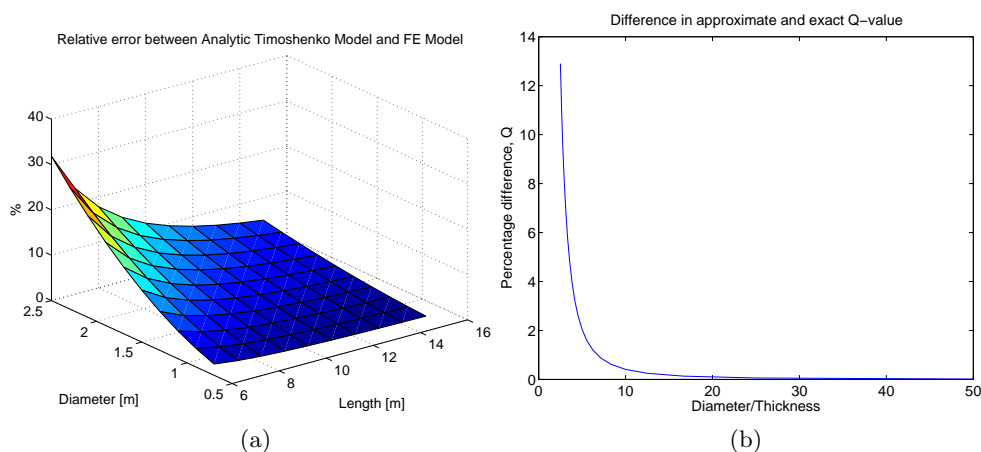


Figure 4.5: (a) Relative deviation of tip displacements between the analytic Timoshenko Model and the FE model for a study of diameter and length. (b) The deviation between the approximate and exact solution for Q .

4.4 Verification of FE Program

The MATLAB FE program is verified by a benchmark example in Appendix C. The verification is made by comparing displacement, stress, and eigenfrequency results to results obtained using ANSYS or analytical results. The comparison of the normal stresses are repeated in Table 4.2 and the comparison of shear stresses are repeated in Table 4.3. It can be concluded, that the FE program works properly and that results are reliable, since the deviation in the normal- and shear stresses are relatively low between MATLAB and ANSYS. The approach for calculating shear stresses is verified by the use of a simple cantilevered beam, since a direct comparison between ANSYS and MATLAB results is difficult for even slightly complicated models.

Element	Element 4							
Node	Node 2							
α [deg.]	0	45	90	135	180	225	270	315
MATLAB result [MPa]	0.867	-252.1	-356.2	-250.4	3.3	256.2	360.3	254.5
ANSYS result [MPa]	0.875	-252.4	-356.7	-250.7	3.3	256.6	360.8	254.9
Difference, %	0.9	0.1	0.1	0.1	0.2	0.2	0.1	0.2

Table 4.2: Normal stresses in eight cross sectional sampling points with $\alpha_{initial} = 0$. Note, percentage difference is calculated from non-rounded values.

Shear stress component	τ_{xy}	τ_{xz}
ANSYS result [Pa]	-1532.4	0
MATLAB result [Pa]	-1529.1	0
Difference, percentage	0.2%	-

Table 4.3: Comparison between shear stresses obtained from an ANSYS and a MATLAB analysis of a simple prismatic cantilever beam.

4.5 Sub Conclusion

Through the chapter the element technology, on which the 3D frame elements are based, has been examined. An implementation of the elements into the MATLAB FE program was made and the results were verified by a comparison to ANSYS. The eigenfrequencies, displacements, and stresses have been verified through a benchmark example of a frame structure in Appendix C. The MATLAB FE program will be used for the stress analysis of the used FE models. Accumulated damage in each frame element of the model will be assessed from the obtained stress values. The model limitations were

investigated by a benchmark example, and a relationship of ten between length and diameter was found. Furthermore, it was found that the approximate formula for determination of the first area moment of inertia yields unreliable results for thickness to diameter ratios below ten.

Chapter 5

Fatigue

In the following chapter the procedure used for calculating the accumulated damage will be presented. This includes an introduction to the chosen cycle counting method and the chosen damage rule. A benchmark example with known cycle counting results and a known damage value is used for the verification of the procedure. The procedure is implemented as a part of the MATLAB FE program. Appendix E supports the present chapter.

5.1 Stress Life Approach

The service life of the jacket structure used in this project should be 20 years. During this time the load spectrum in Appendix A contains more than $1 \cdot 10^8$ cycles. Thus, the stress-life approach for modeling fatigue is chosen. The approach is based on empirically determined data. This means, that the accumulated damage is estimated from constant-life diagrams, where no sequence- or interaction effects are taken into account. It is however possible to include stress concentrations, joints, surface conditions, mean stress effects, and others in the S-N curve. The S-N curves are also known as Wöhler curves. The only effect considered in this project is the influence from the mean stress, since no information is available for the remaining contributors. The method for obtaining the damage in a structure can be seen on Figure 5.1. Each part of the figure is explained in the following sections.

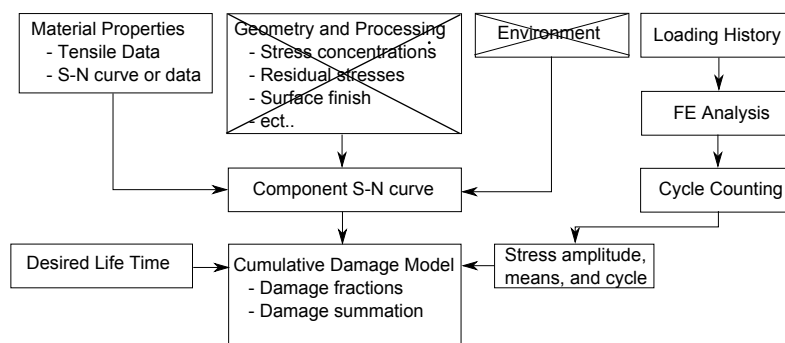


Figure 5.1: Sequential steps in predicting fatigue damage based on the S-N approach. Modified from Stephens et al. [2001].

5.2 Counting Stresses

Cycle counting methods are needed in order to compare the effect of variable amplitude loading history to fatigue data obtained with constant amplitude loading. Both the mean and the amplitudes of the spectrum are needed in order to take the mean stress effect into account when estimating the damage. The largest amplitudes are known to be the highest contributors to the accumulated damage. Thus, a suited counting method capable of counting all the highest amplitudes must be chosen in order to obtain a reliable damage estimation.

The cycles must be counted such that the load ranges are maximized. Several different methods for cycle counting are available. This includes the rainflow method, range-pair method, racetrack method, level-crossing method, and peak counting method.

Stephens et al. [2001] presents the rainflow method as the best and most popular counting method. Furthermore, the rainflow method will be able to count the largest amplitude ranges in the spectrum. Thus, the rainflow method is chosen to count the various spectra in this project. See Stephens et al. [2001] for an in-depth discussion of the rainflow method.

In this project the rainflow counting is carried out by a MATLAB algorithm found in the script *Rainflow.m*. The raw output from the rainflow count is a finite number of columns containing: stress amplitudes, σ_a , stress means, σ_m , number of cycles, n , and the beginning time, t_B of each stress cycle. The cycles are either counted as a reversal or a cycle. The used rainflow script is available from Nieslony [2003] and has been widely used since 2003. The

rainflow counting method is verified by a benchmark example in section E.1 of Appendix E.

5.3 Sorting Rainflow Table

In order to calculate the accumulated damage and the design sensitivities efficiently after the rainflow count, a sorting routine is used to divide the resulting cycle count into a suited number of predefined intervals. This will help reduce the total number of terms in the damage calculation and thus the calculation time. In the following, the sorting routine used on the raw output from the rainflow count is described. The benefits of using a sorting algorithm for the DSA is discussed in section 8.3.

The first step in the sorting routine is to set up two intervals, an amplitude interval and a mean interval. The number of desired amplitude and mean intervals, N_{Amp} and N_{Mean} , may be chosen by the user or by the study in section 5.6.1. The amplitude interval step, $A_{0,interval}$, is determined by finding the maximum amplitude, $A_{0,max}$, from the raw rainflow count and dividing this by the number of desired amplitude intervals, N_{Amp} :

$$A_{0,interval} = \frac{A_{0,max}}{N_{Amp}} \quad (5.3.1)$$

By multiplying $A_{0,interval}$ with 1 to N_{Amp} the upper limit in each interval may be determined. Take for example $A_{0,max} = 100$ and $N_{Amp} = 4$ which will give the maximum values in the intervals: [25 50 75 100]. Thus, the four amplitude intervals: $0 < A_0 \leq 25$, $25 < A_0 \leq 50$, $50 < A_0 \leq 75$, and $75 < A_0 \leq 100$ are set up.

The set up of the mean intervals is done in a much similar manner. However, resulting mean values may be both positive and negative. Thus, the maximum values of the mean interval are determined by:

$$\mu_{interval} = \mu_{min} + \frac{(\mu_{max} - \mu_{min})}{N_{Mean}} \quad (5.3.2)$$

where μ_{max} and μ_{min} are the maximum and minimum mean values determined from the raw rainflow count. Again the fraction in equation (5.3.2) is multiplied with 1 to N_{Mean} . As an example take $\mu_{max} = 50$, $\mu_{min} = -50$, and $N_{Mean} = 4$, which will give the maximum values of the intervals: [-25 0 25 50]. Thus, the four mean intervals: $-50 < \mu \leq -25$, $-25 < \mu \leq 0$, $0 < \mu \leq 25$, and $25 < \mu \leq 50$ are defined.

The raw rainflow count is sorted according to the intervals determined above. Thus, counted stress cycles of almost equal amplitude and mean value will be stored in the same interval when a sufficient number of intervals are used. The amplitudes will however not be exactly the same, why a method for choosing a suited amplitude value in a given interval must be examined. Three possible approaches are examined for this.

5.3.1 Maximum Amplitude Approach

The first approach is to use the upper interval limits for the amplitude. The result of this will most likely be an overestimation of the damage based on the output matrix, since all cycles in each column will get the maximum interval amplitude value. This approach is denoted the maximum approach.

It should be noted, that the mean value in each interval will always be set using this approach.

5.3.2 Average Amplitude Approach

The second approach is simply to average the amplitude values in a given interval. This means the amplitude value for the first interval $0 < A_0 \leq 25$ will be 12.5. Whether this method will result in an over- or an under estimation of the accumulated damage is highly dependent on the spectrum on which the rainflow count is carried out. This approach will be referred to as the average approach.

5.3.3 Equivalent Amplitude Approach

The last approach is based on the determination of an equivalent amplitude stress which can be determined from:

$$\sigma_{a,eq} = \left(\frac{\sum_{i=1}^p n_i (\sigma_{a,i})^m}{\sum_{i=1}^p n_i} \right)^{\frac{1}{m}} \quad (5.3.3)$$

where p is the number of contributors in the given interval, $\sigma_{a,eq}$ is the equivalent amplitude stress, n_i is the cycle count for entry i , and $m = 3$ for normal stress or $m = 5$ for shear stresses, [Standard, 1999]. Equation (5.3.3) is derived by setting the damage of the raw rainflow output equal to the damage found by the use of the equivalent stress amplitude. This means, that the approach should predict the most accurate damage estimation of the three. This approach will be referred to as the equivalent approach.

Each of the three approaches will be applied to the jacket structure, and the most efficient approach chosen based on the performance of this real life model.

5.3.4 Example of Sorting Routine

An example of an output matrix from the sorting routine can be seen in Table 5.1. Here, the amplitude values used in Table 5.1 are determined by the use of the maximum approach.

i	1	2	3	4	5	6	7	8	9	10	11	12	13	14	15	16
σ_{ai}	25	25	25	25	50	50	50	50	75	75	75	75	100	100	100	100
σ_{mi}	-25	0	25	50	-25	0	25	50	-25	0	25	50	-25	0	25	50
n_i																

Table 5.1: The output matrix from the sorting routine based on the maximum approach used on the counted rainflow results. Illustrated for normal stresses.

The total number of intervals is denoted N_i . Having set up the output matrix, the remaining part is to add up the counted cycles in the correct amplitude and mean intervals. Note, the amplitude and mean values after which the various cycles are sorted are always determined from equations (5.3.1) and (5.3.2) regardless of the procedure used to determine the actual amplitude value of the output of the sorted rainflow table. Note, an output matrix illustrated by Table 5.1 will be present for both normal- and shear stresses for each cross sectional sample point in the analyzed model.

When using the sorted results for the damage calculation, the number of terms in the Palmgren-Miner expression are reduced significantly. However, the exact mean and amplitude stress values are no longer available. Hence, the damage estimated from the sorted rainflow table will be approximate. The sorting algorithm is verified using a benchmark example in section E.1.

5.4 Component S-N Curve

The amplitude value must be modified to account for mean stresses. This can be done by using the modified Goodman equation:

$$\frac{\sigma_a}{\sigma_{NF}} + \frac{\sigma_m}{\sigma_u} = 1 \quad \Rightarrow \quad \sigma_{NF} = -\frac{\sigma_a \cdot \sigma_u}{\sigma_m - \sigma_u} \quad (5.4.1)$$

In equation (5.4.1), σ_a is the stress amplitude, σ_u is the ultimate tensile strength, and σ_m is the mean stress. By the use of equation (5.4.1), σ_{NF}

which is the fully reversed fatigue stress at $2N_f$ reversals, may be determined.

From the S-N curve, the number of reversals to fatigue failure for a given stress amplitude can be found by:

$$\sigma_{NF} = \sigma'_f (2N_f)^b \quad \Rightarrow \quad N_f = \frac{1}{2} \exp \left(\frac{\ln(\sigma_{NF}/\sigma'_f)}{b} \right) \quad (5.4.2)$$

N_f is the cycles to failure, σ'_f is the fatigue strength for one reversal, while b is a material constant corresponding to the slope of the S-N curve in a log-log diagram. Note, that this approach is similar for shear stresses although the S-N curve must be altered. Thus, different fatigue data for normal and shear stresses must be used. The used S-N curve denotes the mean fatigue life for the material. This means as much as 50% of the material can have suffered fatigue failure before the fatigue limit is reached.

5.4.1 Fatigue Properties

Material parameters of steel type RQC-100 from [Stephens et al., 2001, Table A.2] is chosen for this project. This allows for the use of an example in [Stephens et al., 2001, section 9.6] for the verification of the damage estimation. Thus, the Wöhler exponents for the S-N curve are set to $b = -0.114$. The ultimate tensile stress is $\sigma_u = 931$ MPa and the yield stress is $\sigma_y = 883$ MPa, while $\sigma'_f = 1240$ MPa. The cut-off value on the S-N curve is disregarded in order to keep the approach simple and conservative as seen on Figure 5.2b. The Goodman diagram used is shown on Figure 5.2a. This is also the simplest version of the Goodman diagram since the modified Goodman line is simply mirrored around the amplitude-axis and no effects of beneficial negative mean stresses are included.

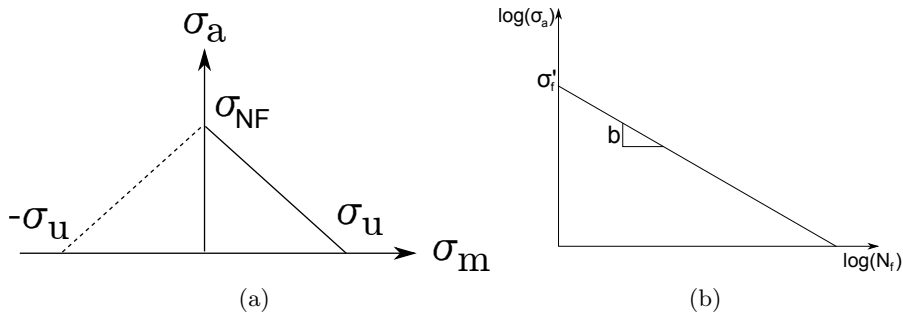


Figure 5.2: (a) Goodman diagram. (b) Wöhler curve.

5.5 Cumulative Damage Model

The damage is defined by [Stephens et al., 2001, P. 274] as: ”*The damage caused by one cycle is defined as $\eta = 1/N_f$, where N_f is the number of repetitions of this same cycle that equals the median life to failure*”.

The damage can be obtained by a number of different models. The Palmgren-Miner linear damage rule is usually the preferred method, since it is difficult to determine whether the use of a more complicated non-linear damage model will actually result in a more accurate damage estimation. Since neither the linear or non-linear damage models will give a precise damage estimation for all experimental data, the simple linear model is often chosen, [Stephens et al., 2001, P. 276]. Note, Palmgren-Miners damage rule does not take the load sequence into account. The Palmgren-Miner damage rule, for one block of a load spectrum, may be written as:

$$\eta_{block} = \sum_{i=1}^p \frac{n_i}{N_{fi}} \quad (5.5.1)$$

n_i being the number of cycles for a given stress amplitude. N_{fi} is the number of cycles for which the stress amplitude will fail according to the S-N curve. Equation (5.5.1) states that failure occurs when the sum of all ratios of cycles against fatigue cycles equals one.

The load case in Appendix A shows only a single 10 minutes block. In order to estimate the TLT damage for the generic jacket structure, it is necessary to scale the damage of one block so it corresponds to a service life of 20 years, as mentioned in section 2.2. Thus, the damage found in one block is multiplied by the number of these blocks occurring in a service life of 20 years. It should be noted, that an operational time of 80% is assumed and that the availability of the OWT is 100%. Usually more than 1000 different load series are used to design a wind turbine. Since only one load series is available, the damage in the generic jacket structure will be estimated by expanding the single load series to the entire service life as shown by equation (5.5.2).

$$\eta_{TLT} = \eta_{block} \cdot \left(\frac{20 \cdot 365 \cdot 24 \cdot 60 \cdot 60}{600} \right) \cdot 0.8 \quad (5.5.2)$$

5.6 Benchmark Example of Damage Estimation

A benchmark example of the damage estimation, presented in Appendix E.1, is used to verify the algorithm for estimation of the damage. In the example the

rainflow count, the sorting algorithm, and the calculation of the accumulated damage are all tested. The benchmark example is taken from [Stephens et al., 2001, P. 293], and the stress history of the example can be seen in Figure 5.3.

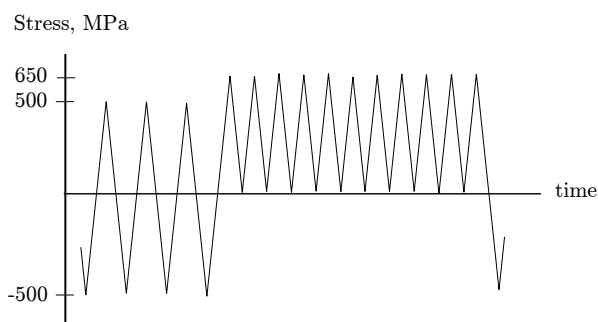


Figure 5.3: The stress history of the benchmark example used for the verification of the fatigue procedure, [Stephens et al., 2001, Figure 9.16].

5.6.1 Damage Estimation and Effect of Interval Subdivision

The main observation made in the verification example is that the number of intervals for the sorting of the rainflow counting has a high influence on the estimated damage. It was seen in the validation of the sorting algorithm how the subdivision of amplitude and mean intervals may lead to large over- or underestimations of the calculated accumulated damage. A representation of this is seen in Figures 5.4a, 5.4b, and 5.5 for the three different approaches for determining the stress amplitude value in the sorted rainflow table.

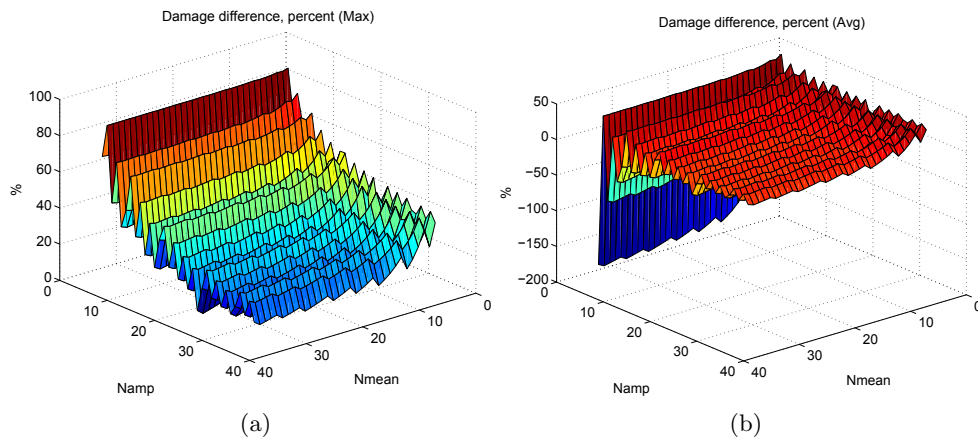


Figure 5.4: The percentage deviation between the true damage (0.0139) and the estimated damage using the (a) maximum amplitude approach and (b) the average amplitude approach as a function of interval subdivisions.

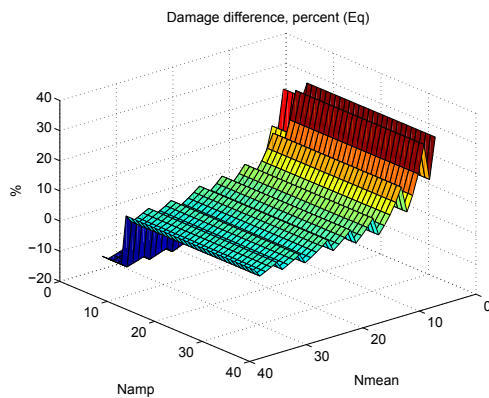


Figure 5.5: The percentage deviation between the true damage (0.0139) and the estimated damage using the equivalent stress amplitude approach as a function of interval subdivisions.

In Figures 5.4a, 5.4b, and 5.5 the number of amplitude and mean intervals range from 3 to 35. Generally the accuracy of the damage calculation increases as the number of intervals are increased, as expected. This follows directly from the more precise amplitude and mean stress values in the output table from the sorting algorithm obtained by the higher number of intervals. For the max and average amplitude approach, Figures 5.4a and 5.4b, the number of amplitude intervals seems to have a higher influence on the percentage

difference in damage than the number of mean intervals. For the equivalent amplitude approach, Figure 5.5, the number of amplitude intervals has no effect above eight, since this number of intervals is capable of representing the true spectra. The remaining difference is caused by the use of the maximum mean values. Thus, the number of mean intervals has the highest effect for this approach for the given example. However, it should be noted that the scaling of the axis makes the mean effect look more significant in Figure 5.5 than the other two cases.

A rough assessment of the accuracy of each approach can be determined from the percentage damage difference obtained for the highest number of amplitude and mean intervals. For the maximum approach the overestimation of the damage is 10%, whereas the overestimation of the equivalent amplitude approach is 4%. The average approach underestimates the true damage by approximately 6%. However, it should be noted that neither of the three approaches seems to be fully converged at the examined point.

The distinct 'stair' shape of all three surfaces is a result of the fairly low number of load sample points used in this analysis. This means, each individual stress amplitude will have a higher effect on the calculated damage. Thus, the damage is highly affected whenever a single cycle or reversal switches from one stress amplitude to another in the sorted rainflow table as a result of an increased number of intervals. For an infinite number of load sample points the surface of for instance Figure 5.4a should be smooth.

It is not possible from the stress spectrum in Figure 5.3 to determine which of the three approaches will be the most appropriate for a real life model. Thus, the number of interval subdivisions is investigated further for the jacket model in section 6.3.

5.7 Sub Conclusion

Through the chapter, a method for obtaining the damage in each cross sectional sample point of the model was established and verified. It was seen how the number of intervals in the sorted rainflow table and the approach used for determining the amplitude value had a significant effect on the estimated damage. The three approaches and the number of intervals must be examined on the full jacket structure in order to determine the most efficient approach for a real life application as shown in section 6.3. The obtained damage quantity

may be used as a part of the input to the optimization. Furthermore, the method for damage estimation is used for an initial analysis of the jacket structure presented in the next chapter.

Chapter 6

FE Analysis of Jacket Structure

This chapter has the purpose of presenting the FE jacket model and an initial analysis by using the developed MATLAB FE program. The purpose of the analysis is to determine the initial damage in the cross sectional sample points of the model to clarify the usability of the structural analysis on a real life structure. Furthermore, the number of intervals in the sorted rainflow table is investigated in depth. The effect of sampling the load spectrum is examined in order to determine how the number of load sample points influence the damage estimation and computational time.

6.1 FE Jacket Model

The initial cross sectional properties of the frame elements were introduced in Chapter 2. A cross of frame elements have been introduced in the top of the FE jacket model, in order to apply the loads in the top center of the TP. These artificial frame elements have been provided with a stiffness of 100 times the stiffness of the other frame elements in the model. The elements are numbered from 105 to 108 and the damage in these elements will not be examined since their only purpose is to create a point for applying the four load series described in Appendix A. The loads are applied in the center of the cross as shown on Figure 6.7, and the legs of the model are clamped. The properties of the model are summarized in Table 6.1. The original mass will be used to evaluate the optimized structure.

Mass [kg]	Density [kg/m ³]	Elements	Nodes
562,660	7850	108	57

Table 6.1: Properties of the FE jacket model

6.1.1 Local Member Coordinate System

A local member coordinate system is defined for each element. The local x' -axis is defined pointing from the lowest node number to the highest, with the origin located in the lowest node number. On the sides S2 and S4, see Figure 6.1a, the local y' -axis points in the same direction as the global X-axis. For the sides S1 and S3 the local y' -axis points in the same direction as the global Y-axis. A special case is the local member coordinate system of the cross in the top representing the TP. The x' - y' plane for these elements are chosen to be normal to the global Z-axis.

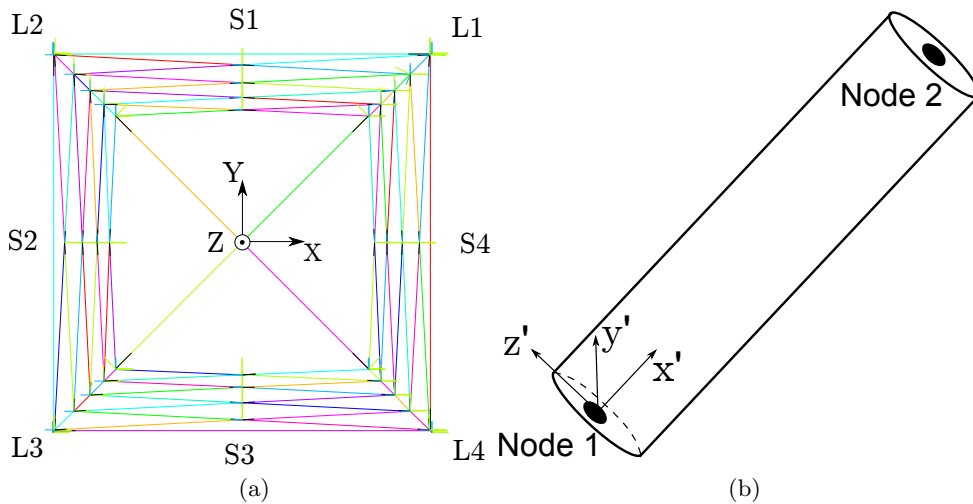


Figure 6.1: (a) The global coordinate system and numbering of legs and sides in the jacket model and (b) The local coordinate system for a 3D frame element.

6.2 Influence of Sampling the Load Cases

The chosen sampling of the load spectrum will have a significant influence on the damage estimation. Thus, a study of this influence is needed in order to choose a suitable number of sample points of the load spectrum. The load

spectrum in Appendix A contains 60,000 data points given for 600 seconds, which reveals a sampling frequency of 100 Hz. It is sampled by picking the first entry in the load vector and using a constant sampling frequency until the end is reached. Several studies from other authors have been made on the subject of reducing a load spectra to a lower number of sample points without compromising the accuracy of the damage estimation. The subject of reducing load spectra is however out of the scope of this project.

The influence of the number of load sample points is examined by the use of the jacket model loaded with P_x , P_y , M_x , and M_y with non-proportional load spectra. The influence of the load sampling may be illustrated by viewing the first 100 seconds of the spectra for example used for the force P_x , see Figure 6.2. The load spectra for P_y , M_x , and M_y contains similar fluctuations and show the same sampling tendencies as the load spectrum for force P_x . However, figures for these applied loads are not shown in the report.

The first 100 seconds contains 10,000 data points in the full spectrum. The full spectrum is sampled with 750, 1,500, 3,000, and 6,000 sample points, which gives sampling frequencies of 1.25 Hz, 2.5 Hz, 5 Hz, and 10 Hz. It is seen how a low number of sample points have a significant effect on the resulting spectrum, since a lot of load peaks are disregarded, cf. Figure 6.2a. These peaks are of major importance when estimating the accumulated damage, since this is dominated by the amplitude values.

As expected, the higher number of sampling points represents the original spectrum more accurate. For shorter time series it is recommended to use the full spectrum for the damage estimation. However, it is difficult to assess, from the figures alone, the value of the error introduced by sampling the load spectrum instead of using the full spectrum. Thus, a small comparison of the damage in a chosen point in the FE jacket model is made for the four different sample frequencies. The chosen point is one of the points with the highest damage. The result may be seen in Table 6.2.

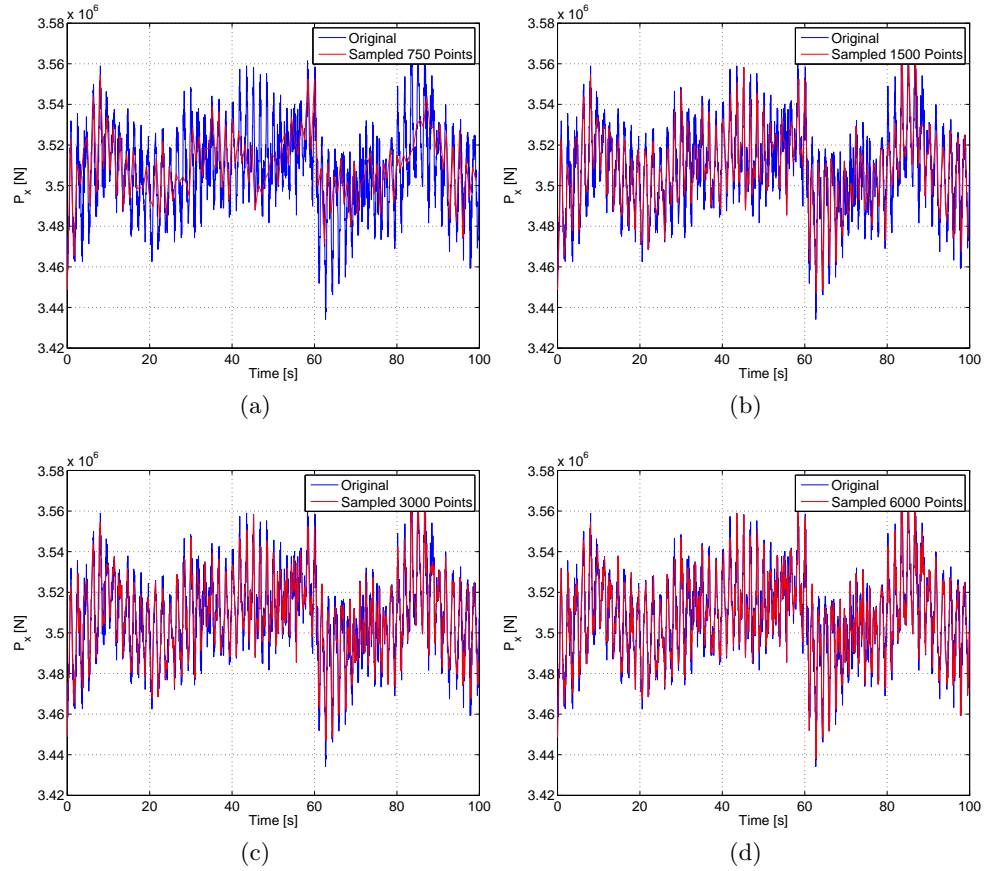


Figure 6.2: Effect of sampling the load spectrum for force P_x with: (a) 750 sample points, (b) 1,500 sample points, (c) 3,000 sample points, and (d) 6,000 sample points.

Load sample points	Damage in point 161	Calculation time	Difference
$Damage_{750}$	$2.1 \cdot 10^{-17}$	55 s	54%
$Damage_{1500}$	$2.5 \cdot 10^{-17}$	1 min 34 s	45%
$Damage_{3000}$	$3.1 \cdot 10^{-17}$	2 min 59 s	32%
$Damage_{6000}$	$4.0 \cdot 10^{-17}$	5 min 37 s	12%
$Damage_{60000}$	$4.6 \cdot 10^{-17}$	51 min 10 s	-

Table 6.2: The influence of the chosen number of load sample points on the total accumulated damage in the structural point numbered 161. The difference in damage is calculated according to a damage of $4.6 \cdot 10^{-17}$, which is determined when the full load spectrum is used.

As expected, the accumulated damage is increased for an increasing number of sample points, since more load peaks are included in the

analysis. Furthermore, a higher number of sample points results in a better approximation of the damage obtained when using the full spectra, which must be expected as well.

The computation time for one iteration of the structural analysis using all 60,000 sample points is approximately 51 minutes. As seen in Table 6.2 this may be reduced to approximately 55 s when using 750 load sample points. However, the underestimation of the damage is increased each time the number of load sample points are reduced.

6.3 Influence of the Number of Intervals in the Rainflow Counting

It was shown in section 5.6.1 how the number of intervals, in which the result from the rainflow counting is sorted, had a significant influence on the calculated damage. The number of amplitude intervals required depends on the load spectrum, hence the number of intervals must be determined based on the load spectrum for the FE jacket model. For the FE jacket model, the exact accumulated damage quantity is not known prior to the analysis since this will require that the damage is determined for 60,000 sample points without using the sorted rainflow table. Thus, the choice of a suited number of intervals cannot be based on the relative error between the true damage and the calculated damage as was the case in section 5.6.1. Instead, the number of amplitude and mean intervals are varied and a convergence point of the damage quantity is sought. The damage is evaluated at an arbitrary chosen cross sectional sample point in the jacket structure. The number of load sample points used is 6,000.

The three approaches for determining the amplitude value, the maximum, average, and equivalent approaches will all be applied in order to determine the most efficient method w.r.t. calculation time and accuracy.

In Figures 6.3a, 6.3b, and 6.4 the accumulated damage for sample point 4 in node 2 of element number 14 is seen. The number of amplitude and mean intervals, N_{Amp} and N_{Mean} respectively, are varied from 3 to 35.

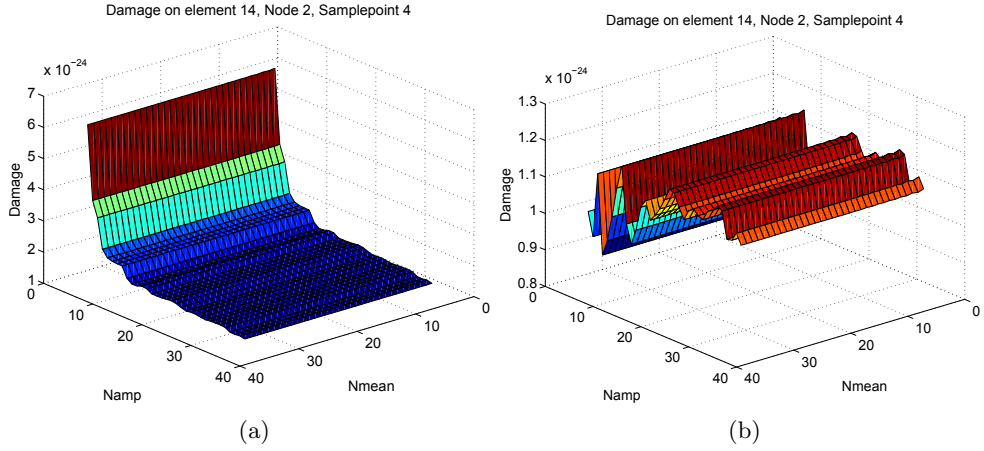


Figure 6.3: The damage in cross sectional sample point 4 of node 2 in element 14 using the (a) max amplitude approach and (b) the average amplitude approach.

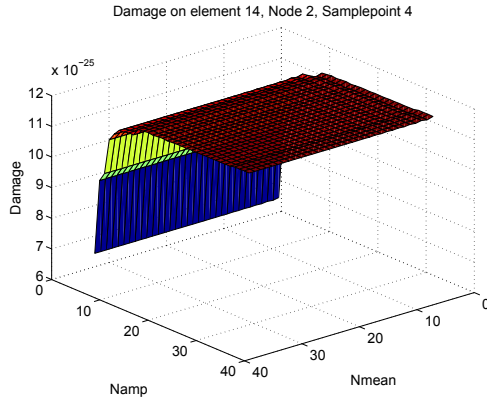


Figure 6.4: The damage in cross sectional sample point 4 of node 2 in element 14 using the equivalent stress amplitude approach.

As seen in Figures 6.3a, 6.3b, and 6.4 the number of mean intervals seems to have a little, if any, effect above 6 subdivisions for all three approaches. Thus, the number of mean intervals is chosen to $N_{Mean} = 6$. Next, the needed number of amplitude intervals, N_{Amp} for each of the three approaches is determined based on Figure 6.5.

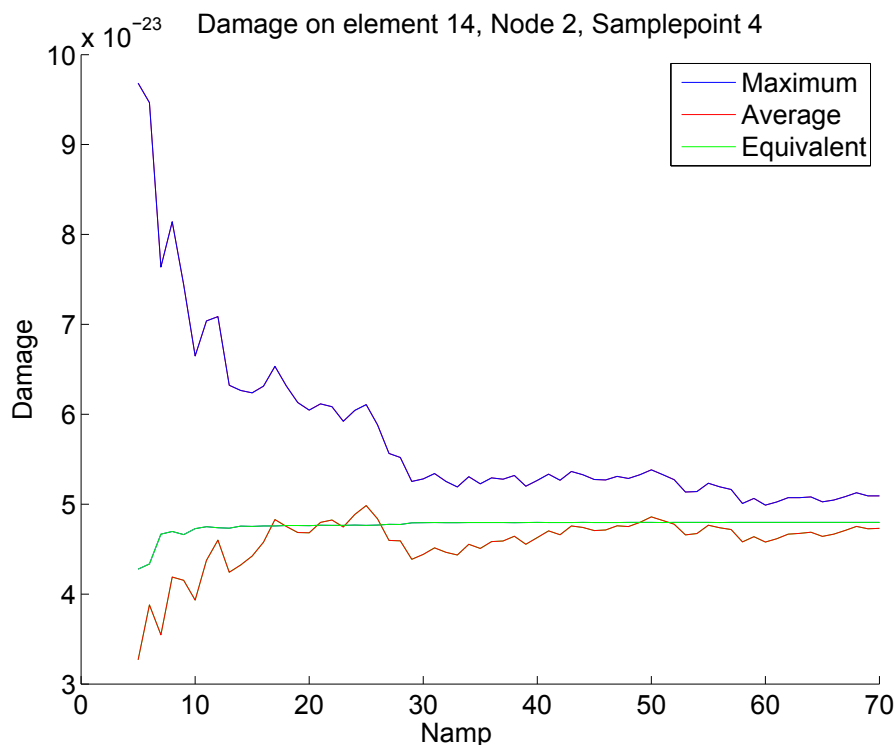


Figure 6.5: The damage in cross sectional sample point 4 of node 2 in element 14 using the maximum amplitude approach, the average amplitude approach, and the equivalent amplitude approach as a function of amplitude intervals and $N_{Mean} = 6$

In the following discussion the damage is assumed to be converged at $N_{Amp} = 70$.

The maximum approach overestimates the damage quite much for a low number of amplitude intervals as expected. For the average and equivalent approaches the damage is underestimated for a low number of amplitude intervals. However, for both the equivalent and the maximum approach a clear convergence tendency is seen as the number of amplitude intervals increases. A slightly less smooth convergence tendency may be observed for the average approach as well. For each extra subdivision of the amplitude interval the calculation time is increased linearly. Thus, the lowest number of amplitude intervals, capable of representing the damage, within an acceptable deviation, must be chosen. For the maximum approach the convergence curve seems to level out at around $N_{Amp} = 30$. The same number of intervals are chosen for the average method despite its more wavy convergence curve.

Since the damage is assumed to be fully converged at $N_{Amp} = 70$, a rough estimation of the damage accuracy at $N_{Amp} = 30$ may be assessed. For the maximum approach the damage is overestimated by approximately 6%, and the underestimation for the average approach is approximately 6% as well. The calculation time for the maximum approach using $N_{Amp} = 30$ is determined to 6 minutes and 15 seconds whereas the calculation time for the average approach is approximately equal to 6 minutes and 24 seconds. The convergence curve of the equivalent method is seen to be quite smooth and to level out around $N_{Amp} = 17$. The underestimation of the damage at this number of amplitude intervals is less than 1%. Due to the lower number of amplitude intervals the calculation time was brought down to approximately 4 minutes and 30 seconds. It can be concluded, that all three methods converge towards approximately $5 \cdot 10^{-23}$ as the number of amplitude intervals approaches infinity. The study has been made for several elements in the FE model and they all show the same tendencies. As a result of the higher accuracy at the lower number of amplitude intervals the equivalent method using $N_{Amp} = 17$ and $N_{Mean} = 6$ is chosen for the further work.

6.4 Initial Analysis of Jacket Model

A structural FE analysis of the jacket model is conducted using the developed MATLAB FE program to ensure, that the method is applicable on a real life structure. The moments and forces from the provided load case are used. The settings in the structural FE analysis are chosen based on the preceding analysis. Thus, it is chosen to use 17 amplitude intervals, 6 mean intervals, and the equivalent approach for determining the stress amplitude in the sorted rainflow table. Furthermore, 750 load sample points are used and 4 cross sectional sample points in each end of the frame elements are set. The damage determined in each cross sectional sample point can be seen on Figure 6.6. The numbering of the cross sectional sample points used in Figure 6.6 follows the bookkeeping system presented in Table 4.1. It can be seen that a few sample points in the cross sections have a significantly higher damage than the rest. The low damage values and the large span in damage between different cross sectional sample points suggest that the generic jacket structure will benefit from a structural optimization.

It should be noted, that the damage in elements 101 to 108, which are the

elements embedded in the TP, are not plotted on Figure 6.6.

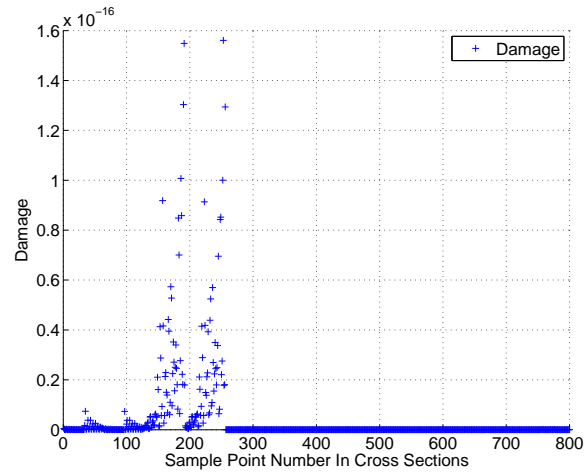


Figure 6.6: The damage determined in each cross sectional sample point in the FE jacket model for 750 load sample points.

The deformed shape of the FE model, for a unit load in the X-direction and a unit moment around the Y-axis, can be seen on Figure 6.7. It is verified from Figure 6.7 that the clamped BC has been imposed properly. Note, the deformed shape, seen on Figure 6.7, has been scaled to emphasize the deformation. The deformed shape for at unit force in the Y-direction, and a unit moment around X-axis are not shown here.

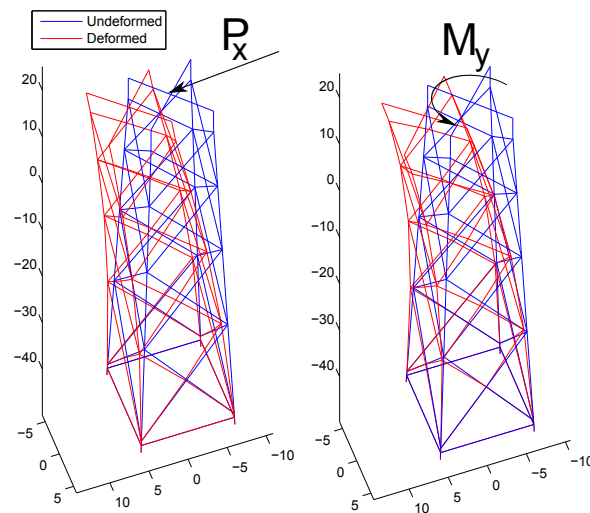


Figure 6.7: The scaled deformed shape of the jacket model for a unit force applied in the X-direction and a unit moment around the Y-axis.

One of the highest loaded points in the jacket model is sample point 161, which is located in element 21, node 1, cross sectional sample point 1, (see Table 4.1 for the bookkeeping system). Recall, this point was used in the analysis in section 6.2.

6.5 Sub Conclusion

The FE jacket model was set up and used for an initial analysis. The damage was determined in a number of cross sectional sample points in the ends of each element. It was seen how the number of load sample points had a significant influence on the accumulated damage. The number of intervals in the rainflow counting was investigated as well. The amplitude had a larger influence than the mean for all examined approaches. The number of intervals for the amplitude was set to 17, while the number of intervals for the mean was set to 6 and the equivalent approach was chosen. The initial analysis of the jacket structure showed, that no cross sectional sample points in the model is close to the fatigue limit. Thus, it may benefit from a structural optimization.

Part III

Optimization

Chapter 7

Introduction

The main task of the project is to investigate methods for performing a size optimization with the purpose of lowering the total mass of the jacket structure as explained in Chapter 3. In order to use optimization techniques it is necessary to identify and define the design variables, the cost function and the constraint function. A DSA is necessary since gradient based optimization is used.

Based on the problem definition, the design optimization problem can be set up as:

$$\begin{aligned} \text{Minimize:} & \quad f(\bar{x}) \\ \text{Subject to:} & \quad g_k(\bar{x}) \leq 0, \quad k = 1, \dots, N_g \end{aligned}$$

where \bar{x} is a vector containing the design variables. f is the cost function given as the total mass of the model, and g_k is a number of inequality constraints, given as the damage in each cross sectional sample points in the FE jacket model. N_g is the total number of constraints and k is the constraint number.

7.1 Design Variables

The design variables are identified as the thickness and diameter of each frame element in the FE jacket model as explained in Chapter 3. The FE jacket model contains 108 elements, which yields 216 design variables in total.

The cross sectional area and the second moment of inertia are explicit functions of the outer diameter and the wall thickness. As seen on Figures 7.1a and 7.1b the relationships are nonlinear. Furthermore, a change in either

area or second moment of inertia will have a direct influence on the global stiffness matrix, since it is an explicit function of the two. From the figures it can be seen that the diameter has a larger influence than the thickness for most of the designs. Note, that as the diameter increases the influence from the thickness increases as well.

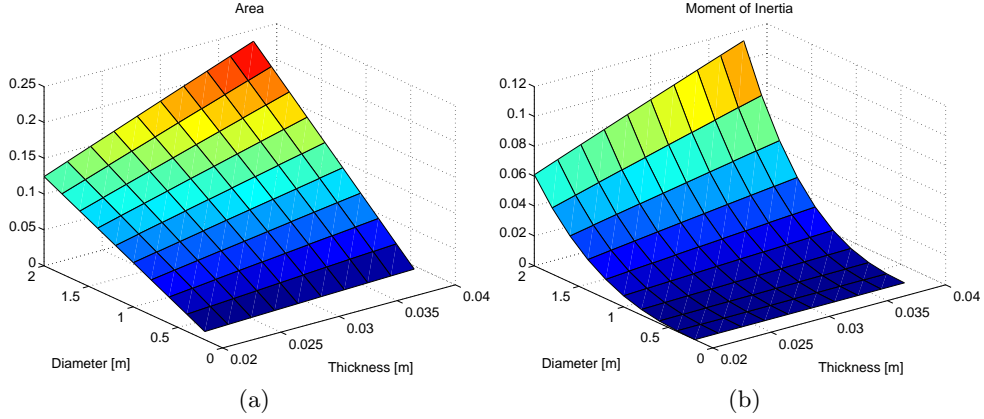


Figure 7.1: Parametric study of the design variables outer diameter, d and thickness, t for: (a) Area, and (b) The second moment of inertia.

The design variables will be considered as continuous during the optimization.

7.2 Cost Function

Since the objective is to decrease the total mass of the FE jacket model, the criterion function is defined as the sum of the mass of all elements as shown in equation (7.2.1).

$$f(\bar{x}) = m_{total} = \sum_{i=1}^{N_E} \rho A_i(\bar{x}) L_i \quad (7.2.1)$$

where ρ is the density, defined in Chapter 2.

In order to enhance the performance of the optimizer and the convergence, the cost function will be normalized according to its initial value. Thus, large numerical differences in the cost function are avoided since the cost function will have values limited to: $0 < f(\bar{x}) \leq 1$.

7.3 Inequality Constraints

The inequality constraint functions are identified as the damage in each cross sectional sample point in the FE model. Recall, that the used Palmgren-Miner damage rule use the S-N curve and takes mean stress effects into account by using the modified Goodman equation. Thus, the inequality fatigue constraint function can be stated:

$$g_k = \sum_{i=1}^{N_i} \frac{n_i}{\frac{1}{2} \exp\left(\frac{\ln\left(-\frac{\sigma_{a_i} \cdot \sigma_u}{\sigma_{m_i} - \sigma_u} / \sigma_f'\right)}{b}\right)} - 1 \leq 0 \quad (7.3.1)$$

This is an implicit function of the design variables. Thus, special techniques are required to perform the DSA for the inequality constraint functions.

7.4 Symmetry Conditions

In order to ease the manufacturing of the jacket structure, it is chosen to introduce a number of symmetry conditions in the FE jacket model. Besides the manufacturing point of view, the symmetry conditions ensure that the jacket structure has the sufficient strength for wind and wave directions different from the direction in which they are applied in the FE jacket model. By enforcing symmetry conditions on the jacket structure the number of design variables for the optimizer may be reduced as well, thus reducing the overall calculation time. An overview of the applied symmetry is given in Figure 7.2.

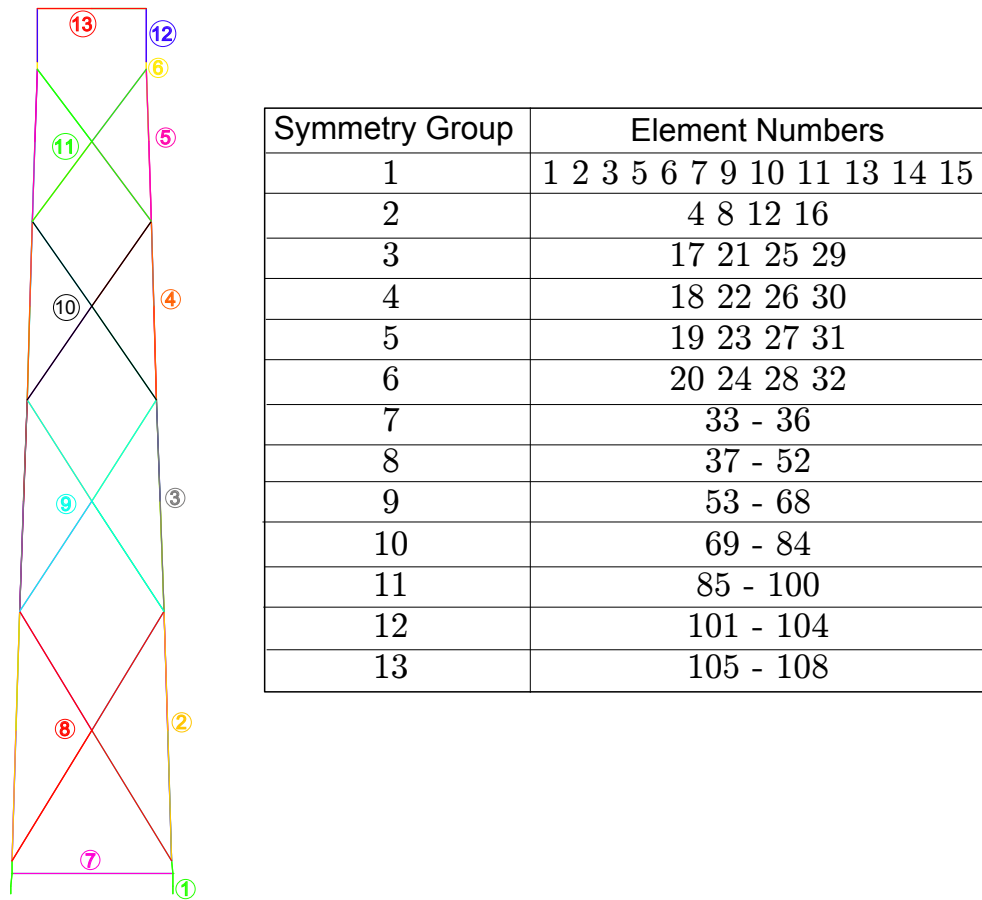


Figure 7.2: Symmetry conditions imposed on the FE jacket model.

As seen on Figure 7.2 the jacket structure is divided into 13 symmetry groups. This reduces the number of design variables from $2 \cdot 108$ to $2 \cdot 13$. It should be noted that it is not necessary to perform a normalization of the fatigue constraint since it is already defined as the number of cycles divided by the number of cycles to failure.

Chapter 8

Design Sensitivity Analysis

In order to use gradient based optimization methods the sensitivities of the cost and constraint functions are needed. In this chapter different methods for determining the sensitivity of the cost and constraint functions will be described, derived, and discussed. The most suitable methods will be determined with the purpose of being applied on the FE jacket model. The methods treated in the chapter are the Overall Finite Difference (OFD) Method, as well as an analytical and a semi-analytical Direct Differentiation Method (DDM) and Adjoint Method (AM). The methods for the DSA are explained in details in Appendix F, while the methods developed for the FE jacket model are explained through this chapter. Appendices G and H contain various equations supporting this chapter as well.

8.1 DSA of Cost Function

The DSA of the cost function introduced in equation (7.2.1) can be made analytically since the area is given explicitly as a function of the design variables, d and t . This is shown in equation (8.1.1).

$$\frac{\partial A_i(\bar{x})}{\partial d} = \pi t \qquad \frac{\partial A_i(\bar{x})}{\partial t} = \pi(d - 2t) \qquad (8.1.1)$$

$$\frac{\partial f(\bar{x})}{\partial x_j} = \sum_{i=1}^{N_E} \rho \frac{\partial A_i(\bar{x})}{\partial x_j} L_i \qquad (8.1.2)$$

By use of equation (8.1.2) the sensitivity of the cost function w.r.t. the design variables may be found.

8.2 DSA for Constraint Function

The methods used for the DSA of the constraint function include the DDM, AM, and OFD. These are explained in details in Appendix F and illustrated on Figure 8.1 together with the functions needed. The dashed lines illustrate, that several functions are needed in order to determine the desired quantity. Thus, all the functions in the dashed lines are needed to determine the displacement derivative, $\frac{d\bar{U}}{dx_j}$ and the Lagrange multiplier, $\bar{\lambda}$. The terms needed for the partial derivative of the constraint function $\frac{\partial g_k}{\partial x_j}$ and $\frac{\partial g_k}{\partial U}$ can be found either numerically or analytically. Thus, the goal is to determine $\frac{dg_k}{dx_j}$ by determining the described components shown on Figure 8.1.

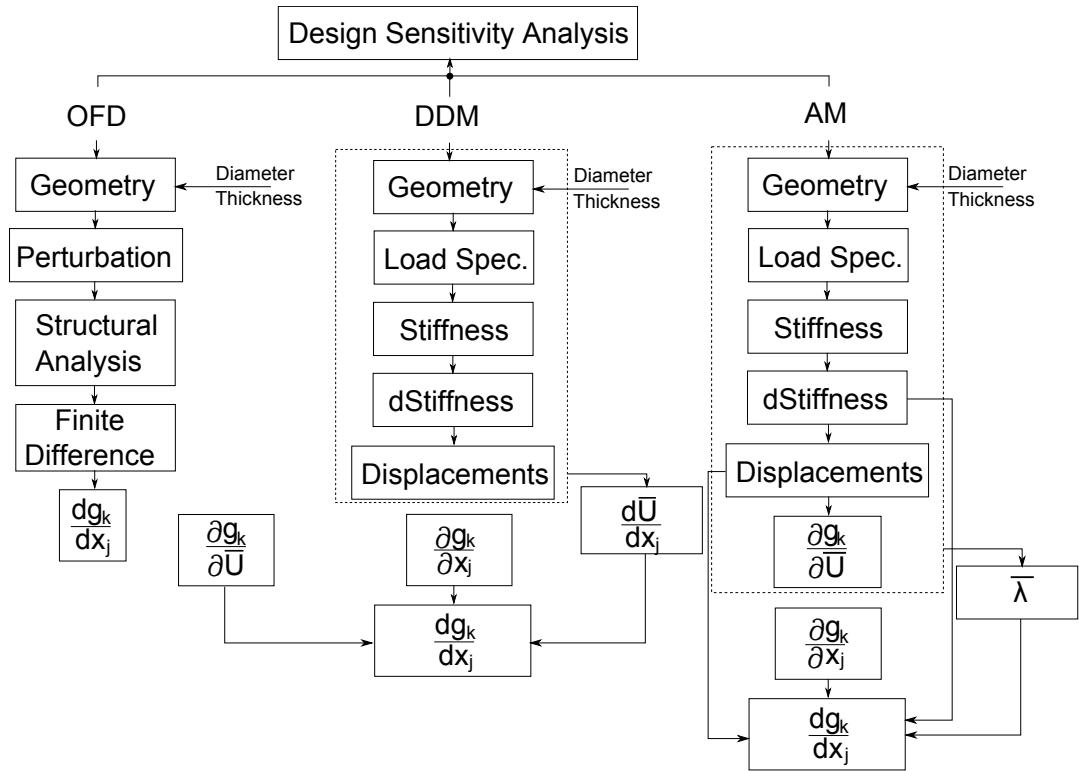


Figure 8.1: Methods and procedures for DSA for the constraint function.

8.2.1 Fatigue Constraint

The starting point for the analytical DSA of the constraint function is equation (7.3.1), which is repeated below:

$$g_k = \sum_{i=1}^{N_i} \frac{n_i}{\frac{1}{2} \exp\left(\frac{\ln\left(-\frac{\sigma_{ai} \cdot \sigma_u}{\sigma_{mi} - \sigma_u} / \sigma'_f\right)}{b}\right)} - 1 \leq 0 \quad (8.2.1)$$

where the terms σ_u , b , and σ'_f are all material constants. The variables σ_{ai} and σ_{mi} are the stress amplitude and stress mean values in each interval of the sorted rainflow table from the rainflow count. These are a function of the displacements and the design variables as seen in equation (8.2.2). Furthermore, the amplitude and mean stress are a function of the rainflow count of the resulting stress spectra. The last variable is the cycle counter, n_i which is a function of the rainflow count and the amplitude and mean stress variables. Note, the damage from a resulting shear stress is calculated using an equivalent procedure. The variables and their dependencies are listed below:

$$\begin{aligned} \sigma_{ai} & (RF(\bar{U}(\bar{x}), \bar{x})) \\ \sigma_{mi} & (RF(\bar{U}(\bar{x}), \bar{x})) \\ n_i & (RF(\sigma_{ai}, \sigma_{mi})) \end{aligned} \quad (8.2.2)$$

According to these implicit dependencies among the variables, special techniques for the DSA are required. Note, that in order to eliminate the dependency on the rainflow counting, the sorted rainflow table from the rainflow routine is kept fixed during the DSA in the OFD approach. Instead of redoing the rainflow count for each DSA, resulting in an unwanted rainflow dependency, the stress values in the original table are simply updated according to the changes in stress results when a design variable is perturbed. Thus, equations (8.2.2) can be rewritten as:

$$\begin{aligned} \sigma_{ai} & (\bar{U}(\bar{x}), \bar{x}) \\ \sigma_{mi} & (\bar{U}(\bar{x}), \bar{x}) \\ n_i & : \text{constant} \end{aligned} \quad (8.2.3)$$

Equation (8.2.3) is the basis in the analytical DSA since the implicit dependency of the rainflow count is eliminated.

8.2.2 Sensitivity Analysis

Three different methods are examined for the DSA. These are the DDM, the AM, and the OFD methods. The DDM and the AM can either be analytical or semi-analytical. The contributions from the mean and amplitude displacements are used in the analytical methods since the damage is caused by a contribution from these two terms. The damage caused by the mean displacements are accounted for by the modified Goodman line, while the damage caused by the amplitude is taken directly from the Wöhler curve. Thus, the full derivative must be assembled from a contribution of the mean and amplitude displacements.

Analytical and Semi-analytical Methods

The DDM is derived in Appendix F.2. For the DSA of the fatigue constraint function the DDM is modified in order to match the displacement field to the stresses at a given time. Thus, the DDM used for the DSA of the fatigue constraint is given as:

$$\begin{aligned} \frac{dg_k}{dx_j} = & \sum_{i=1}^{N_i} \left(\frac{\partial g_{k-amp}}{\partial x_j} \right)_i + \left(\frac{\partial g_{k-amp}}{\partial \bar{U}} \right)_i^T \frac{d\bar{U}_{amp}}{dx_j} + \\ & \left(\frac{\partial g_{k-mean}}{\partial x_j} \right)_i + \left(\frac{\partial g_{k-mean}}{\partial \bar{U}} \right)_i^T \frac{d\bar{U}_{mean}}{dx_j} \end{aligned} \quad (8.2.4)$$

where i is the interval number in the sorted rainflow table introduced in section 5.3, k is the cross sectional sample point number, and j is the design variable number. The terms $\frac{\partial g_k}{\partial x_j}$ and $\frac{\partial g_k}{\partial \bar{U}}$ for both the amplitude and mean are determined either by finite difference approximations or by analytical methods. $\frac{d\bar{U}}{dx_j}$ is determined analytically. The analytical determination of $\frac{\partial g_k}{\partial x_j}$ and $\frac{\partial g_k}{\partial \bar{U}}$ can be found in equations (8.2.8) and (8.2.10). The difference between $\frac{\partial g_{k-amp}}{\partial x_j}$ and $\frac{\partial g_{k-mean}}{\partial x_j}$ is highlighted in equation (8.2.8). The displacement sensitivities, $\frac{d\bar{U}}{dx_j}$ for both amplitude and mean contributions are determined from the derived equilibrium equation as:

$$\mathbf{K} \frac{d\bar{U}_{amp}}{dx_j} = \left(-\frac{d\mathbf{K}}{dx_j} \cdot \bar{U}_{i-amp} \right) \quad ; \quad \mathbf{K} \frac{d\bar{U}_{mean}}{dx_j} = \left(-\frac{d\mathbf{K}}{dx_j} \cdot \bar{U}_{i-mean} \right) \quad (8.2.5)$$

Again, a clear distinction is made between the contributions from an amplitude or a mean displacement. The purpose of this distinction is to match the displacements to the counted stresses, which are split into an amplitude and a

mean. Note, the applied forces are independent of the design variables. Thus, they are not included in equation (8.2.5). Again, index i denotes the given column in the sorted rainflow table, emphasizing the need for determining a matching displacement field for each non-zero column of the sorted rainflow table. Besides the DDM, the AM can be applied to determine the design sensitivities. The AM is derived in Appendix F.3. As for the DDM the AM is modified with the purpose of using the matching displacement amplitudes or means with the stress entries in the sorted rainflow stress table. Thus, the AM for the DSA of the fatigue constraint is given as:

$$\frac{dg_k}{dx_j} = \sum_{i=1}^{N_i} \left(\frac{\partial g_{k-amp}}{\partial x_j} \right)_i - \bar{\lambda}_{i-amp} \cdot \frac{\partial \mathbf{K}}{\partial x_j} \cdot \bar{U}_{i-amp} + \left(\frac{\partial g_{k-mean}}{\partial x_j} \right)_i - \bar{\lambda}_{i-mean} \cdot \frac{\partial \mathbf{K}}{\partial x_j} \cdot \bar{U}_{i-mean} \quad (8.2.6)$$

$$\mathbf{K}^T \bar{\lambda}_{i-amp} = \left(\frac{\partial g_{k-amp}}{\partial \bar{U}} \right)_i \quad ; \quad \mathbf{K}^T \bar{\lambda}_{i-mean} = \left(\frac{\partial g_{k-mean}}{\partial \bar{U}} \right)_i \quad (8.2.7)$$

where $\bar{\lambda}_i$, for both amplitudes and means, is a vector containing the Lagrange multipliers, which is chosen to eliminate the displacement sensitivities $\frac{d\bar{U}}{dx_j}$ from equation (8.2.6). Note, a vector containing the Lagrange multipliers must be obtained for each individual column, i of the sorted rainflow table. As for equation (8.2.5), a matching displacement field containing both amplitude and mean values must be determined for each non-zero column of the sorted rainflow table. This is illustrated by \bar{U}_{i-amp} and \bar{U}_{i-mean} . As for the DDM the derived stiffness matrix is determined analytically and the terms $\frac{\partial g_k}{\partial x_j}$ and $\frac{\partial g_k}{\partial \bar{U}}$, using both amplitude and mean displacements, are found using either analytical or FD methods. As a result, both the DDM and the AM can be analytical or semi-analytical. The analytical determination of $\frac{\partial g_k}{\partial x_j}$ will be explained next.

Damage Derivative of Design Variables

For the damage constraint presented in equation (7.3.1), the partial derivatives w.r.t. the design variables are given as:

$$\begin{aligned} \frac{\partial g_{k-amp}}{\partial x_j} &= \frac{\partial g_k}{\partial \sigma_{ai}} \frac{\partial \sigma_{ai}(\bar{U}_{i-amp})}{\partial x_j} + \frac{\partial g_k}{\partial \tau_{ai}} \frac{\partial \tau_{ai}(\bar{U}_{i-amp})}{\partial x_j} \\ \frac{\partial g_{k-mean}}{\partial x_j} &= \frac{\partial g_k}{\partial \sigma_{mi}} \frac{\partial \sigma_{mi}(\bar{U}_{i-mean})}{\partial x_j} + \frac{\partial g_k}{\partial \tau_{mi}} \frac{\partial \tau_{mi}(\bar{U}_{i-mean})}{\partial x_j} \end{aligned} \quad (8.2.8)$$

The parenthesis indicates that the displacement fields are an input to the respective terms. The partial derivative of the fatigue constraint w.r.t. the design variables is split into a contribution from either the amplitude or the mean stress. This allows for the use of either a matching amplitude or a mean displacement in equations (8.2.5) or (8.2.6). Note, that the partial derivative w.r.t. the mean stress cannot be determined when the mean stress equals zero due to the used Goodman diagram, see Figure 5.2a.

The damage constraint was introduced in equation (7.3.1). Inserting this into equation (8.2.8) yields:

$$\begin{aligned} \frac{\partial g_{k-amp}}{\partial x_j} &= \frac{-2n_i}{\exp\left(\frac{\ln\left(\frac{-\sigma_{ai}\sigma_u}{(\sigma_{mi}-\sigma_u)\sigma_f'}\right)}{b}\right)} \frac{\partial\sigma_{ai}(\bar{U}_{i-amp})}{\partial x_j} + \\ &\quad \frac{-2n_i}{\exp\left(\frac{\ln\left(\frac{-\tau_{ai}\tau_u}{(\tau_{mi}-\tau_u)\sigma_f'}\right)}{b}\right)} \frac{\partial\tau_{ai}(\bar{U}_{i-amp})}{\partial x_j} \\ \frac{\partial g_{k-mean}}{\partial x_j} &= \frac{2n_i}{\exp\left(\frac{\ln\left(\frac{-\sigma_{ai}\sigma_u}{(\sigma_{mi}-\sigma_u)\sigma_f'}\right)}{b}\right)} \frac{\partial\sigma_{mi}(\bar{U}_{i-mean})}{\partial x_j} + \\ &\quad \frac{2n_i}{\exp\left(\frac{\ln\left(\frac{-\tau_{ai}\tau_u}{(\tau_{mi}-\tau_u)\sigma_f'}\right)}{b}\right)} \frac{\partial\tau_{mi}(\bar{U}_{i-mean})}{\partial x_j} \end{aligned} \quad (8.2.9)$$

The terms: $\frac{\partial\sigma_{ai}(\bar{U}_{i-amp})}{\partial x_j}$, $\frac{\partial\sigma_{mi}(\bar{U}_{i-mean})}{\partial x_j}$, $\frac{\partial\tau_{ai}(\bar{U}_{i-amp})}{\partial x_j}$, $\frac{\partial\tau_{mi}(\bar{U}_{i-mean})}{\partial x_j}$ are determined in Appendix G and H for the normal stresses and shear stresses, respectively. The sign of the first part of each term in (8.2.9) depends on the shape of the Goodman diagram seen on Figure 5.2a. A rainflow count of the displacement spectrum is necessary in order to determine the displacement means and amplitudes needed for the determination of $\frac{\partial\sigma_{ai}(\bar{U}_{i-amp})}{\partial x_j}$, $\frac{\partial\sigma_{mi}(\bar{U}_{i-mean})}{\partial x_j}$, $\frac{\partial\tau_{ai}(\bar{U}_{i-amp})}{\partial x_j}$, and $\frac{\partial\tau_{mi}(\bar{U}_{i-mean})}{\partial x_j}$. Note, these terms are dependent on the displacement field, since moments and shear forces are determined from the displacements, for instance see equation (G.0.6). Thus, each $\frac{\partial g_k}{\partial\sigma_{ai}}$ must have a matching $\frac{\partial\sigma_{ai}(\bar{U}_{i-amp})}{\partial x_j}$, which means a matching displacement field should be found for each interval in the sorted rainflow table from the rainflow count.

The moments and shear forces will be determined based on a displacement amplitude in order to determine $\frac{\partial \sigma_{ai}(\bar{U}_{i-amp})}{\partial x_j}$ and $\frac{\partial \tau_{ai}(\bar{U}_{i-amp})}{\partial x_j}$. In a similar procedure the terms $\frac{\partial \sigma_{mi}(\bar{U}_{i-mean})}{\partial x_j}$ and $\frac{\partial \tau_{mi}(\bar{U}_{i-mean})}{\partial x_j}$ will be determined using a mean displacement value. This is explained further in section 8.3.

At this point, the partial derivative of the damage constraint w.r.t. the design variables can be determined. A partial derivative term must be found for each non-zero column in the sorted rainflow table.

The result of this sensitivity analysis will be the sensitivity of each constraint function w.r.t. each design variable of the model. Thus, the dimension of the output matrix will be $N_g \times N_x$.

Damage Derivative of Displacements

In a similar manner as equation (8.2.8), the partial derivatives of the damage constraint w.r.t. the global displacements may be obtained:

$$\begin{aligned} \frac{\partial g_{k-amp}}{\partial \bar{U}} &= \frac{\partial g_k}{\partial \sigma_{ai}} \frac{\partial \sigma_{ai}(\bar{U})}{\partial \bar{U}} + \frac{\partial g_k}{\partial \tau_{ai}} \frac{\partial \tau_{ai}(\bar{U})}{\partial \bar{U}} \\ \frac{\partial g_{k-mean}}{\partial \bar{U}} &= \frac{\partial g_k}{\partial \sigma_{mi}} \frac{\partial \sigma_{mi}(\bar{U})}{\partial \bar{U}} + \frac{\partial g_k}{\partial \tau_{mi}} \frac{\partial \tau_{mi}(\bar{U})}{\partial \bar{U}} \end{aligned} \quad (8.2.10)$$

Again i is the interval number in the sorted rainflow table obtained by the sorting of the rainflow count results, and k is the cross sectional sample point number. The fatigue constraint function is inserted into equation (8.2.10), which yields:

$$\begin{aligned} \frac{\partial g_{k-amp}}{\partial \bar{U}} &= \frac{-2n_i}{\exp\left(\frac{\ln\left(\frac{-\sigma_{ai}\sigma_u}{(\sigma_{mi}-\sigma_u)\sigma_f'}\right)}{b}\right)} \frac{\partial \sigma_{ai}(\bar{U})}{\partial \bar{U}} + \\ &\frac{-2n_i}{\exp\left(\frac{\ln\left(\frac{-\tau_{ai}\tau_u}{(\tau_{mi}-\tau_u)\sigma_f'}\right)}{b}\right)} \frac{\partial \tau_{ai}(\bar{U})}{\partial \bar{U}} \end{aligned}$$

$$\begin{aligned} \frac{\partial g_{k-mean}}{\partial \bar{U}} = & \frac{2n_i}{\exp\left(\frac{\ln\left(\frac{-\sigma_{ai}\sigma_u}{(\sigma_{mi}-\sigma_u)\sigma'_f}\right)}{b}\right)} (\sigma_{mi} - \sigma_u) b \frac{\partial \sigma_{mi}(\bar{U})}{\partial \bar{U}} + \\ & \frac{2n_i}{\exp\left(\frac{\ln\left(\frac{-\tau_{ai}\tau_u}{(\tau_{mi}-\tau_u)\sigma'_f}\right)}{b}\right)} (\tau_{mi} - \tau_u) b \frac{\partial \tau_{mi}(\bar{U})}{\partial \bar{U}} \end{aligned} \quad (8.2.11)$$

The terms: $\frac{\partial \sigma_{ai}(\bar{U})}{\partial \bar{U}}$, $\frac{\partial \sigma_{mi}(\bar{U})}{\partial \bar{U}}$, $\frac{\partial \tau_{ai}(\bar{U})}{\partial \bar{U}}$, $\frac{\partial \tau_{mi}(\bar{U})}{\partial \bar{U}}$ are determined analytically in Appendix G and H for the normal stresses and shear stresses, respectively. It should be noted, that these terms are only dependent of the linear elastic displacement field, and independent of the displacement history of the structure. Thus, the rainflow count of the displacements is only used when determining $\frac{\partial g_k}{\partial x_j}$. The distinction between damage contributions from a stress amplitude or a stress mean must however still be made due to the need for different displacement fields, see equations (8.2.4) and (8.2.6).

The obtained results are verified using a FD approximation. The FD approximation can be used in the semi-analytical approach as well. The FD scheme for the determination of $\frac{\partial g_k}{\partial \bar{U}}$ keeps the design variables fixed and makes changes to the global displacements. A displacement spectra is available for each DOF in the model. The perturbation is chosen to be the same for all points in the spectra, and it is chosen to be a fraction of the largest displacement in the spectra. When the displacement spectra have been perturbed, the stresses are determined and the damage is estimated by the use of equation (7.3.1). Finally, the FD approximation is found based on a forward- or a central FD. The central FD finite difference scheme is given as:

$$\begin{aligned} \frac{\partial g_k}{\partial \bar{U}} = & \frac{g(\bar{U} + \Delta \bar{U}, \bar{x}) - g(\bar{U} - \Delta \bar{U}, \bar{x})}{2\Delta \bar{U}} + o^2(\Delta \bar{U}) \\ & \text{for } 1, \dots, N_{DOF} \quad k = 1, \dots, N_g \end{aligned} \quad (8.2.12)$$

As seen in equation (8.2.10) both the stress amplitude and mean must be perturbed in the FD scheme. Thus, two different methods for the displacement perturbation must be applied. This is illustrated in Figure 8.2 for a forward perturbation.

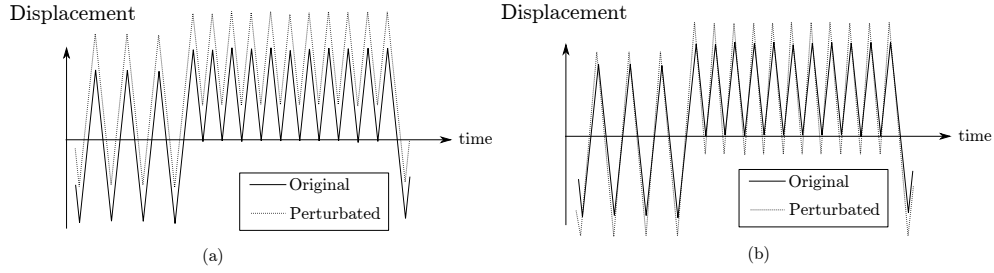


Figure 8.2: (a) Displacement forward perturbation to change mean and (b) displacement forward perturbation to change amplitude.

The displacement perturbation seen in Figure 8.2(a) will change the mean displacement, and thus the mean stresses of the seen spectra. Note, that the amplitude values are unchanged for this displacement perturbation. For the change of the stress amplitude the forward displacement perturbation seen in Figure 8.2(b) is used. Note, the mean is unchanged for this displacement perturbation. Thus, two FD schemes using the two different displacement perturbation must be made and superposed in order to approximate the analytically obtained results.

It should be noted, that the FD approximation of $\frac{\partial g_{k-amp}}{\partial \bar{U}}$ and $\frac{\partial g_{k-mean}}{\partial \bar{U}}$ are the only numerical term used for the the semi-analytical DSA since $\frac{\partial g}{\partial x_j}$ cannot be separated into a mean and an amplitude part. Thus, it is only possible to use FD schemes for the mean and amplitude contributions in the numerical determination of $\frac{\partial g_{k-amp}}{\partial \bar{U}}$ and $\frac{\partial g_{k-mean}}{\partial \bar{U}}$ to obtain the full derivative by the semi-analytical DDM or AM.

8.3 Implementation and Bookkeeping

A bookkeeping scheme is presented in Table 8.1, and it is based on the sorting algorithm presented in section 5.3. A table similar to Table 8.1 is available for each cross sectional sample point. The number of columns in the bookkeeping scheme has dimensions: $N_i = N_{Amp} \times N_{Mean}$. The influence of the number of chosen intervals on the damage estimation was examined in section 6.3. N_i should be set as low as possible since this is beneficial according to reducing the computational time. Table 8.1 is made for illustration purposes only since it contains three different tables in one. This is illustrated by the bold horizontal lines. Every $\left(\frac{\partial g_k}{\partial x_j}\right)_i$ has dimensions $N_g \times N_x$, and $\left(\frac{\partial g_k}{\partial \bar{U}}\right)_i$ has dimensions of $N_g \times N_{DOF}$, and one will be available for each non-zero column of the

sorted rainflow table. The Lagrange multiplier used in the AM, $\bar{\lambda}_i$ is a vector calculated for each non-zero column of the sorted rainflow table. Several stress reversals are grouped in each interval, but only the first beginning time, t_B for each stress reversal is stored in order to match the displacement field to the given stress interval in the sorted rainflow table. Note, all displacement fields are stored without a sorting to ensure a displacement field can always be found from a beginning time. The displacement field is used in the determination of $\left(\frac{\partial g_k}{\partial x_j}\right)_i$ and for the determination of the sensitivity from either equation (8.2.4) or (8.2.6). It is necessary to find the matching displacement field in order to maintain the equilibrium state for which the system of equations is solved.

Several stress reversals of similar amplitude and mean may be stored in the same interval in the sorted rainflow table. They will however occur at different times. Only the beginning time of the first stress reversal stored in an interval is stored, and used to determine a matching displacement field. Thus, it is assumed that all stresses in an interval can be matched with the same displacement field, without introducing a significant inaccuracy in the results. This assumption is treated further in the discussion in Chapter 12.

i	1	2	3	4	5	6	7	8	...	N_i
t_B										
σ_{ai}										
σ_{mi}										
$n_{\sigma i}$										
τ_{ai}										
τ_{mi}										
$n_{\tau i}$										
$\left(\frac{\partial g_k}{\partial x_j}\right)_i$										
$\left(\frac{\partial g_k}{\partial U}\right)_i$										
$\bar{\lambda}_i$										

Table 8.1: Bookkeeping system used in the analytical DDM and AM. A similar table is available for all cross sectional sample points denoted with index k .

8.4 Verification of DSA Method

This section has the purpose of verifying the analytical DSA implementation in MATLAB. A benchmark example of a cantilevered prismatic beam is used for the verification since it is a simple transparent example. Deficiencies are still present in the analytical DSA method, which are discussed and illustrated in Appendix K.

8.4.1 Defining the Benchmark Example

A FE model of a cantilever prismatic beam with fixed/free BCs and a circular hollow cross section is set up. The length of the beam is set to 1.0 m, the diameter of each element is 0.1 m, and the thickness of each element is 0.02 m. The tip of the beam is loaded with three fluctuating forces and three fluctuating moments. The model contains five elements and thus ten design variables. The model includes four cross sectional sample points in each end of the individual frame elements. Thus, the model contains a total number of 40 cross sectional sample points, which are numbered on Figure 8.3.

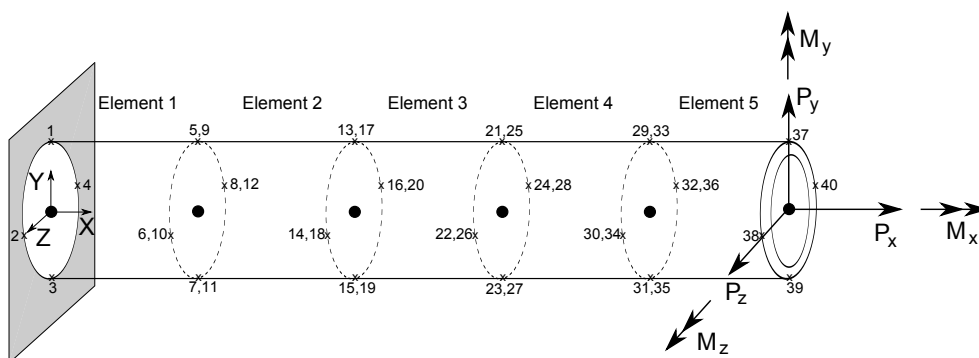


Figure 8.3: Beam model for verification of the DSA numbered with $k = 1, \dots, 40$.

A total number of six nodes are included in the model. Since the first node is locked in all DOFs, 30 free DOFs exist in the model. The number of intervals for the rainflow table is set to 17 for the amplitude and 6 for the means, which gives a total number of 102 intervals in the rainflow table.

The applied non-proportional load spectra of Figure 8.4 contains 29 load sample points. For this verification the same spectrum will be used for all applied loads, but it will be scaled differently for each load, see Figure 8.4.

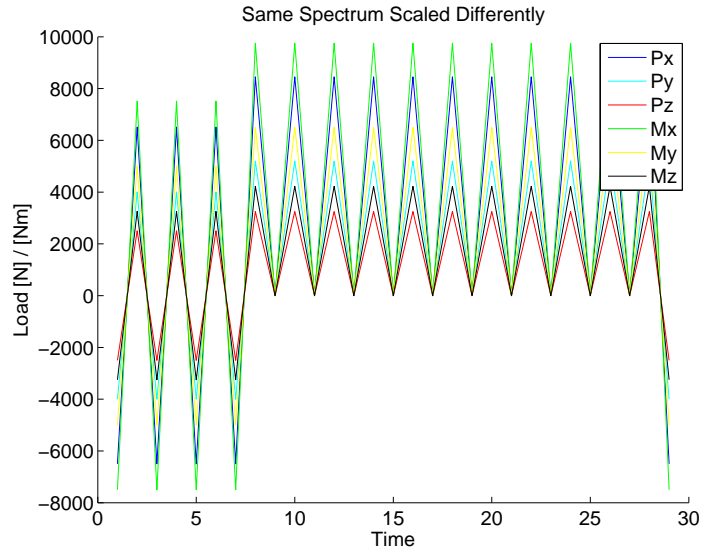


Figure 8.4: The load series used for the six applied loads obtained by scaling the same spectra by six different factors.

8.4.2 Verification and Results

In the following the sensitivity results for $\frac{dg_k}{dx_j}$ obtained by the use of the forward FD, the DDM, and the AM will be compared to a central difference approximation. The DDM was introduced in equation (8.2.4) and the AM was introduced in equation (8.2.6). Only results for the first two elements will be used for the comparison.

No semi-analytical results will be shown since it is only possible to obtain a FD approximation of $\frac{\partial g_{k-amp}}{\partial U}$ for a mean and an amplitude contribution. The result of the forward FD approximation can be seen in Table 8.2. The result of the DDM can be seen in Table 8.3 and the result of the AM is shown in Table 8.4.

		Diameter				Thickness			
Element 1	Node 1	0.4%				0.1%			
		0.4%				0.1%			
		0.4%				0.1%			
		0.4%				0.1%			
	Node 2	0.4%				0.1%			
		0.4%				0.1%			
		0.4%				0.1%			
Element 2	Node 1		0.4%				0.1%		
			0.4%				0.1%		
			0.4%				0.1%		
			0.4%				0.1%		
	Node 2		0.4%				0.1%		
			0.4%				0.1%		
			0.4%				0.1%		

Table 8.2: The percentage deviations between sensitivities obtained using the forward FD and the central FD scheme.

		Diameter				Thickness			
Element 1	Node 1	0.2%				0.2%			
		0.1%				0.1%			
		0.7%				0.7%			
		0.4%				0.4%			
	Node 2	0.2%				0.2%			
		0.2%				0.2%			
		0.7%				0.7%			
Element 2	Node 1		0.2%				0.2%		
			0.2%				0.2%		
			0.7%				0.7%		
			0.4%				0.4%		
	Node 2		0.2%				0.2%		
			0.2%				0.3%		
			0.6%				0.6%		
	0.3%				0.3%				

Table 8.3: The percentage deviations between sensitivities obtained using the DDM and the central FD scheme.

		Diameter				Thickness			
Element 1	Node 1	0.2%				0.2%			
		0.1%				0.1%			
		0.7%				0.7%			
		0.4%				0.4%			
	Node 2	0.2%				0.2%			
		0.2%				0.2%			
		0.7%				0.7%			
		0.4%				0.4%			
Element 2	Node 1		0.2%				0.2%		
			0.2%				0.2%		
			0.7%				0.7%		
			0.4%				0.4%		
	Node 2		0.2%				0.2%		
			0.2%				0.3%		
			0.6%				0.6%		
			0.3%				0.3%		

Table 8.4: The percentage deviations between sensitivities obtained using the AM and the central FD scheme.

As seen from the very low percentage deviations in Tables 8.3 and 8.4 the use of analytical methods for the DSA for the given example yields reliable results. Thus, it is established, that the analytical results are valid for this type of load case with a non-proportional load spectra applied. Next, the calculation times of the various methods are examined.

8.4.3 Calculation Time of DSA Methods

From Tables 8.3 and 8.4 it is seen that the DDM and the AM yields equal results as expected. It can be concluded, that both methods are capable of determining the design sensitivities of the given example. The calculation time for the methods are seen in Figure 8.5.

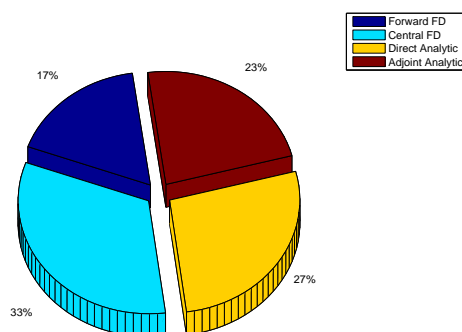


Figure 8.5: Comparison of calculation times for the forward FD, central FD, DDM, and AM.

The comparison of the calculation time is made by computing the DSA using all four methods for the same example. The combined calculation time of all four methods denotes 100%.

From Figure 8.5 it is seen that the forward FD approximations of the gradients is the fastest of the compared methods. The central FD scheme is approximately twice as slow as the forward, which is expected since twice as many function evaluations must be used. No extraordinary attempts of speeding up the analytical DSA, i.e. by using vectorization or parallel computing, is made. Thus, the analytical methods are slower in their current state than the forward FD scheme.

At first glance, it might seem unexpected that the DDM is slower than the AM for the given example, when the number of design variables, 10 is compared to the number of cross sectional sample points, 40. The time difference is however caused by an additional 'for-loop' in the DDM used to determine the full displacement sensitivities before determining the gradient. Thus, an additional calculation time should be expected. Some of the drawbacks in the analytical approach is the large amount of data storage. The number of function calls are significant even for relatively simple examples. A more in-depth study of the calculation time in the DSA are presented in Appendix I.

8.5 Comparison of Methods for DSA

The choice of method for DSA is highly dependent on the computational time of each method and the properties of the design model. The number of design variables and the number of cross sectional sample points have a significant impact on the choice of method. The DDM requires solution of $\frac{d\bar{U}}{dx_j}$ for each design variable in equation (8.2.4), while the AM requires the solution of equation (8.2.6) for each cross sectional sample point.

8.6 Sub Conclusion

Throughout this chapter it has been shown how to obtain the full derivatives of the damage constraint w.r.t. the design variables. This was made by an OFD and the analytical DDM and AM. One of the main considerations is the setup of the full derivative by the contributions from an amplitude part and a mean part. Furthermore several implications in the methods was clarified. It should be noted, that the damage constraint was not differentiable in the case of a zero mean stress according to the shape of Goodman diagram. This was a limitation of the DSA together with the limitations presented in Appendix K. It can be concluded, that if a semi-analytical approach was used, it would only be possible with a numerical determination of $\frac{\partial g_{k-amp}}{\partial \bar{U}}$ and $\frac{\partial g_{k-mean}}{\partial \bar{U}}$, while all other terms would be computed analytically. Finally, the analytical DSA approach has been verified by a benchmark example. Here it was shown, that the analytical methods yield results within an acceptable accuracy. It can be concluded, that it is more efficient to compute the sensitivities analytically if calculation time and precision is compared between the numerical and analytical approach.

Chapter 9

Optimization Methods

This chapter has the purpose of introducing the considerations regarding the available methods for use in the optimization as well as a selection of the most suited methods. Considerations regarding a move limit strategy are made. A robust optimization algorithm must be chosen, and its advantages and disadvantages will be clarified. Aggregated functions are introduced for the post processing of the fatigue constraints. Appendix I supports this chapter.

9.1 Optimization Algorithm

The SLP algorithm is chosen for the optimization due to its simplicity and transparency. Furthermore, the SLP method is known to be able to handle many design variables without problems, [Arora, 2012, Sec. 12.5]. A non-linear optimization problem may be solved using the SLP algorithm by linearizing the response and constraint functions around a given design point. The linearized subproblem can be solved using the Simplex method or similar solving procedures.

In this project a standard SLP algorithm for solving of non-linear optimization problems is provided by Professor Erik Lund. The provided script has been modified in order to suit the optimization problems handled in the following chapter. It should be noted, that the used SLP algorithm will always be initialized from a feasible starting point in this project, since no globalization schemes are used. Further information regarding the SLP algorithm may be found in Lund [2013b] and Arora [2012].

The success of a SLP algorithm is highly dependent on the chosen move limits, which will be examined next.

9.1.1 Move limits

Move limits are used in the SLP algorithm to restrict the change in design variables during each iteration in the optimization algorithm, to ensure the linear approximations of the subproblem are valid. The choice of suitable move limits for the design variables may determine whether the SLP algorithm is successful or not. The choice of the move limits is however highly problem dependent, which means that the optimization problem at hand must be well understood before suitable move limits can be set, [Arora, 2012, Sec. 12.5]. Since a linear algorithm is used to solve a non-linear optimization problem, the move limits should be set low, such that the change in design variables between each iteration is quite limited.

In this project an adaptive move limit strategy is developed with the purpose of lowering the number of iterations, and thus the calculation time, before the optimization algorithm is stopped. A move limit is initialized for each design variable. The move limits are adjusted according to the change in the given fatigue constraint. Thus, if the change in the fatigue constraint value from one iteration to the next is larger than for instance 5% the move limit will be reduced. However, if this change is below for instance 1% the move limit will be increased by a small amount. The percentage values for which to decrease or increase the move limits may vary between different optimization problems. By allowing an increase in the move limits for small changes in the fatigue constraints, the number of iterations needed to approach the bound set by the inequality fatigue constraints can be lowered. No special conditions is applied if the algorithm reach an infeasible point since the optimization will always approach the fatigue bound from a feasible design using small move limits.

9.2 Treatment of Constraint Functions

The max value approach is a simple method to choose the maximum damage value in an element or symmetry group and use this as the value in the optimization. Thus, only one gradient needs to be determined, and the calculation time for each iteration is significantly reduced. Besides this, it seems logical to use the fatigue value in the highest loaded damage point in an element or symmetry group, since this will be the weakest point. It should be noted, that this method may give fluctuations in fatigue constraint values since the point with the largest fatigue constraint quantity may change

between iterations.

Aggregated functions can be regarded as strong tools for post processing of constraints in order to reduce the number of constraints and to avoid fluctuations. In this project the main purpose of using aggregated functions is to assemble several constraints into a single constraint. For instance, a single fatigue constraint value in each element may be calculated based on the constraint values in all cross sectional sample points of the given element. Furthermore, the aggregated functions may be employed whenever several fatigue constraint values are combined to a single constraint value for each symmetry group. This method is in this report referred to as a local approach. The term global approach refers to assembling all constraint function values of the model to a single fatigue constraint value. Only the global approach will be examined in this project.

9.2.1 Aggregated Constraint Functions

A huge number of aggregated functions are available and the choice of the most proper method is highly dependent on the problem treated. Three of the most popular methods of aggregated functions are:

- Kreisselmeier-Steinhauser method.
- Weighted sum method.
- Generalized mean methods.

A study of the different aggregated functions has been performed in order to choose the most suitable method [Lund, 2013a].

The Kreisselmeier-Steinhauser method can take several forms, but only the following form is treated:

$$g(\bar{x}) = g^{max} + \frac{1}{p_{ks}} \ln \left(\sum_{k=1}^{N_g} e^{p_{ks}(g_k - g^{max})} \right) \quad (9.2.1)$$

where p_{ks} is a positive integer and g^{max} denotes the maximum value.

The Kreisselmeier-Steinhauser method will always yield values above the maximum value of the constraints. The Weighted sum method takes the form:

$$g(\bar{x}) = \sum_{k=1}^{N_g} p_{kw} g_k \quad (9.2.2)$$

where N_g is the number of constraints and p_{kw} is the weight factor. The Weighted sum method might give results above the maximum value for some weight factors as well. However, it is quite hard to predict which weight factors will yield a damage value above the maximum. The Kreisselmeier-Steinhauser method gives overly conservative results. The result from the weighted sum method are highly dependent on the chosen weight factors. As a result, these methods will not be discussed further. The Generalized Mean Method (GMM) seem to be a suited tool for post processing of damage constraints and it is the method proposed by Holmberg [2013]. The GMM is preferred for the post processing of the fatigue constraint values, and it will be presented in details next.

9.2.2 Generalized Mean Methods

A number of different GMMs have been considered, some of which are presented in [Holmberg, 2013, Sec 4.1.1]. Based on the area of application in this project the following GMM has been chosen:

$$g^{GMM} = \left(\frac{1}{N_g} \sum_{k=1}^{N_g} (g_k^p) \right)^{1/p} \quad (9.2.3)$$

where N_g is the number of constraints and p is a positive integer. Equation (9.2.3) represents a global approach for the generalized mean method, but it can easily be converted to a local approach based on clustering of element or symmetry group constraint values. The GMM yields a value between the average and maximum value of g_k dependent on the chosen value of p . Thus, it will always give a value equal to or below the maximum value of g_k . If $p = 1$ the GMM will yield an average value of the values in g_k . The other extreme case is when $p \Rightarrow \inf$ where the GMM will give the maximum value of the g_k values. Thus, the choice of p must be determined carefully dependent on the problem treated and the results desired. Holmberg [2013] recommends $p = 8$ or $p = 12$. By using the GMM fluctuations in the fatigue constraint values might be reduced which may be useful or even necessary in order to ensure convergence. The influence of p will be examined further in Appendix M. For the maximum value approach it might be beneficial only to calculate the gradients in the highest loaded cross sectional sample points. This may reduce the calculation time significantly.

9.3 DSA of Generalized Mean Method

Analytical methods are needed in order to calculate the sensitivity of the GMM function. The analytical sensitivity of the GMM can be obtained directly as:

$$\frac{dg^{GMM}}{dx_j} = \left(\frac{1}{N_g} \sum_{k=1}^{N_g} (g_k^p)^{(1/p-1)} \right) \left(\frac{1}{N_g} \sum_{k=1}^{N_g} \left(g_k^{(p-1)} \frac{dg_k}{dx_j} \right) \right) \quad (9.3.1)$$

This equation shows a global approach for the GMM, but it can easily be converted to an local approach based on the damage in each element. The derivative of the constraint function w.r.t. the design variables, $\frac{dg_k}{dx_j}$ is determined from equations (8.2.4) or (8.2.6).

9.4 DSA Verification of Generalized Mean Method

A verification of the implementation of the GMM in the DSA based on a local element approach is shown by the results in Table 9.1. The analytical sensitivities from the DDM are compared to sensitivities obtained by a central FD approach using the cantilevered beam example with a diameter of 0.13 m and a thickness of 0.004 m. The used load series is similar to the stress series seen in Figure 5.3. The damage values in the cross sectional sample points in each element are clustered using the GMM. A maximum deviation of 0.51% is observed, which is regarded as an acceptable deviation. Thus, it can be concluded that the sensitivity analysis of the GMM yields reliable results, and the implementation has been made properly.

Design Variable	Ele. 1	Ele. 2	Ele. 3	Ele. 4	Ele. 5
d_1	0.5%	0	0	0	0
d_2	0	0.4%	0	0	0
d_3	0	0	0.3%	0	0
d_4	0	0	0	0.2%	0
d_5	0	0	0	0	0.1%
t_1	0.5%	0	0	0	0
t_2	0	0.4%	0	0	0
t_3	0	0	0.3%	0	0
t_4	0	0	0	0.2%	0
t_5	0	0	0	0	0.1%

Table 9.1: Percentage deviation between the Central FD approximation and the analytical approach to obtain the sensitivities of the GMM constraint function.

9.5 Sub Conclusion

The SLP algorithm was chosen for the optimization of the jacket structure. The concept of move limits was introduced and an adaptive move limit strategy was developed. Aggregated functions were considered for the post processing of the fatigue constraint values. The GMM was chosen since the Kreisselmeier-Steinhauser method was too conservative and the weight factors for the weighted sum method were difficult to establish. An analytical sensitivity analysis of the GMM was performed in order to obtain the gradient for use in the optimization process. The analytical sensitivities were verified, and it was concluded that the analytical sensitivities yield reliable results. Thus, the methods and tools presented in this chapter will be utilized for the optimization.

Chapter 10

Optimization Results

In the following the results of the optimization will be examined. For the initial optimization, simple benchmark examples using the prismatic cantilevered beam model introduced in Figure 8.3 will be used to verify the chosen analytical approach. A non-proportional load spectrum will be applied, and the SLP algorithm with adaptive move limits, introduced in section 9.1, will be applied. The diameter and thickness design variables will initially be treated individually since this allows for a prediction of the optimum result, which is used as the benchmark result, before they are combined in an optimization. Finally, the optimization approach will be applied to the jacket structure. This chapter is supported by appendices J, K, L, and M.

10.1 Beam with a Single Force Applied

For the first example a single P_y tip load is applied. A diameter and a thickness optimization are performed separately. The GMM will be used for the thickness optimization and the combined diameter and thickness optimization. The choice of p-values in this section is based on a study of the GMM in section 10.1.3. The same cantilevered beam model will be used for all benchmark examples and the sensitivities are determined analytically by the DDM. A second benchmark example utilizing a cantilevered beam with six applied tip loadings can be found in Appendix L.

10.1.1 Diameter Optimization

In the following the outer profile diameters will be used as design variables and the thicknesses will be locked. Due to the simplicity of the beam the highest constraint function value will always occur in the same cross sectional sample point, see Figure 8.3. Thus, the maximum value approach is used to determine the constraint function value in each element since fluctuations are not encountered. The load spectra used for the the tip loading is seen on Figure 10.1a.

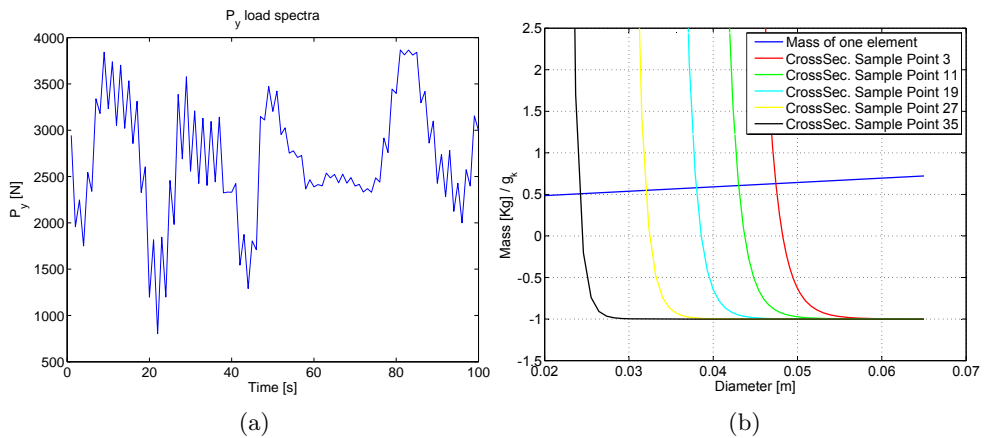


Figure 10.1: (a) The applied load spectra for the P_y tip force. (b) g_k in each of the five elements and the mass of a single element.

The purpose of the optimization is to reduce the mass of the cantilevered beam without violating any fatigue constraints. The initial diameter of the elements is set to 0.07 m and the initial thickness to 0.004 m. A beam length of 0.6 m is chosen for the analysis. This yields an initial mass of 3.9 kg. From Figure 10.1b it is seen that the optimization problem at hand is highly non-linear. This means very small move limits must be set for all design variables. Due to the simplicity of the optimization problem, the optimum solution may in fact be predicted from Figure 10.1b. The optimum diameter for each element must be found when the constraint function value equals zero and is thus right at the bound. This result is used to validate the obtained optimum using the SLP algorithm. Note, this is only possible when the damage in each element is only affected by its own diameter.

The adaptive move limit strategy for this problem is defined as:

- For a change in constraint function value larger than 3%, decrease the move limit by 90%.
- For a change in constraint function value less than 1%, increase the move limit by 8%.

The SLP algorithm converges in 32 iterations to the result shown in Table 10.1.

Element	Diameter, [m]	$g_k(k = 3, 11, 19, 27, 35)$
1	0.050	-0.58
2	0.045	-0.52
3	0.040	-0.44
4	0.033	-0.35
5	0.025	-0.66

Table 10.1: Optimum solution for the cantilevered beam model with P_y tip loading.

A comparison between Table 10.1 and Figure 10.1b reveals that the SLP algorithm converges towards the expected result for all element diameters. However, it should be noted from Table 10.1, that the values of the fatigue constraints are not equal to zero, which means the obtained result is not right at the fatigue bounds. This is a result of the convergence criteria used in the SLP algorithm, which states that the optimization routine is converged when the relative design change between two iterations is below 0.1%. The total reduction in mass for the given example is approximately 47%.

Convergence Criteria

It is examined whether a better design can be obtained using a different convergence criteria. The alternative convergence criteria examined states that the optimization is converged when the fatigue constraint with the lowest value is above -0.1 . Even though a design close to the fatigue bound is found, the number of iterations needed before convergence exceeds 150. Thus, the calculation time is increased by nearly a factor of five. The changes to the design variables are however so low, due to the very low move limits set near the constraint bound, that they are neglectable. Thus, from an engineering point of view, the original convergence criteria w.r.t. the relative change in design

is kept for the optimization.

10.1.2 Optimization and Stresses

The normal and shear stress distribution in the optimized beam is examined in the following. Due to the simplicity of the used beam model, it is expected that the normal stresses in each element in the optimized design will approach the same value. However, it should be noted that some slight differences between the stress values should be expected due to the different constraint function values seen in Table 10.1. An increase in the shear stresses must be expected from the inner to the outer element due to the stair shape of the optimized beam. The normal and shear stress distributions are seen in Figure 10.2. Note, a unit P_y load is applied.

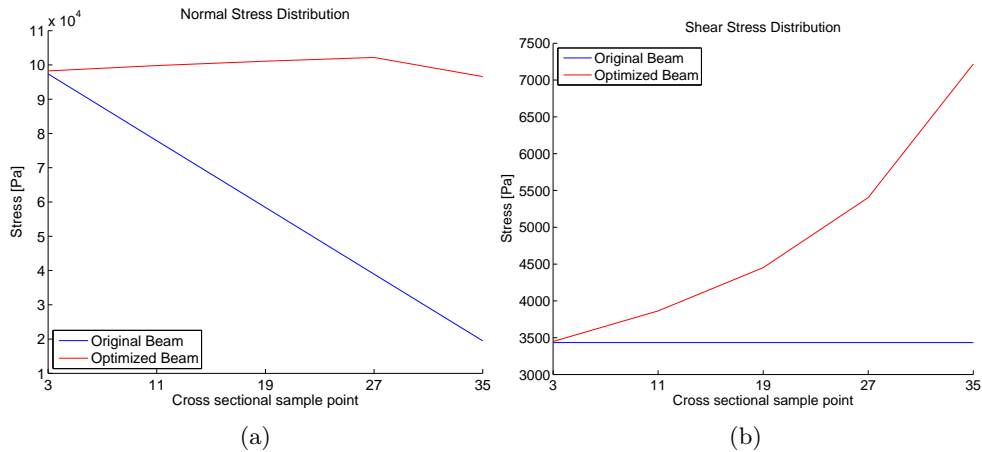


Figure 10.2: (a) The normal stress and (b) the shear stress distribution along the beam model.

From Figure 10.2a it is seen that the normal stress distribution seems to converge toward an equal stress distribution. Figure 10.2b reveals that significant changes are introduced in the shear stresses in the elements near the tip, where shear stresses are more than doubled.

The result illustrated in Figure 10.2a hints, that the optimization of the beam w.r.t. fatigue constraints could be much similar to an optimization using simpler stress constraints. However, it is expected that the differences in optimized design, determined using the two methods, will become more and

more profound as designs become more complicated.

A parametric study using stress constraints is examined in Appendix J.

10.1.3 The Influence of the p-value in the GMM

The GMM on element basis is applied to the cantilevered beam model with a single tip load. The influence of the p-value on the calculated result, the number of iterations for convergence, and the calculation time is examined. P-values: $p = 1, \dots, 15, 30$ are used for the current example. The following move limits and settings have been used for all examined cases:

- For a change in constraint function value larger than 2%, decrease the move limit by 90%.
- For a change in constraint function value less than 1%, increase the move limit by 2%.

It is shown in Appendix M, that the obtained results corresponds well with the results in Table 10.1, where the max value approach is applied for $p \geq 8$. Thus, it is verified that the GMM yields similar results as the maximum value approach if the p-value is set sufficiently large. Tests with p-values above 15 showed that numerical implications may arise. Furthermore, it is recommended to use the GMM with a large p-value rather than the maximum value approach to reduce the risk of fluctuations. In this case only the largest value will remain since all the smaller values will be eliminated by the large p-value. In Appendix M it can be seen, that the p-value has no influence on the number of iterations or the calculation time. Small fluctuations are seen in the number of iterations, but a clear pattern is not recognized. Selected results of Table M.1 can be seen on Figure 10.3. From Figure 10.3b it is seen, that there is a significant difference between the optimized results using the low p-values, while the difference between results above $p = 8$ can be regarded as minor. Thus, the p-value $1 \leq p \leq 8$ will be used in this project.

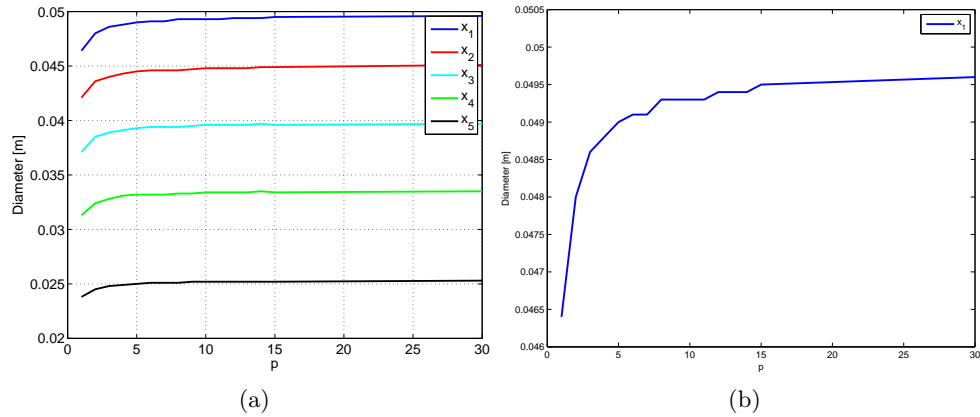


Figure 10.3: (a) Optimization results for the all the diameters with different p-values. (b) Zoom on the optimization results for the diameter x_1 with different p-values.

10.1.4 Thickness Optimization

A thickness optimization is performed with the diameters fixed at 0.04 m in order to investigate the nature of this optimization problem. The profile thicknesses are initialized at 0.009 m. The initial mass of the model is 4.13 kg. The GMM is applied and a p-value of 2 is chosen based on the study presented in section 10.1.3. As for the diameter optimization, a parametric study is used to predict the solution as shown on Figure 10.4.

From Figure 10.4 it can be seen, that the fixed diameter of 0.04 m gives a design where the constraint function value in element one for any examined thickness will be larger than zero. However, the fatigue constraint is not violated why this diameter is kept for the thickness optimization. From Figure 10.4 the nonlinear behavior of the cost function can be seen as reflected by the gradient in equation (8.1.1). Thus, the most severe difference between the diameter optimization and the thickness optimization is the change in cost function from linear to non-linear behavior. This subproblem must be linearized as well in order to apply the SLP algorithm.

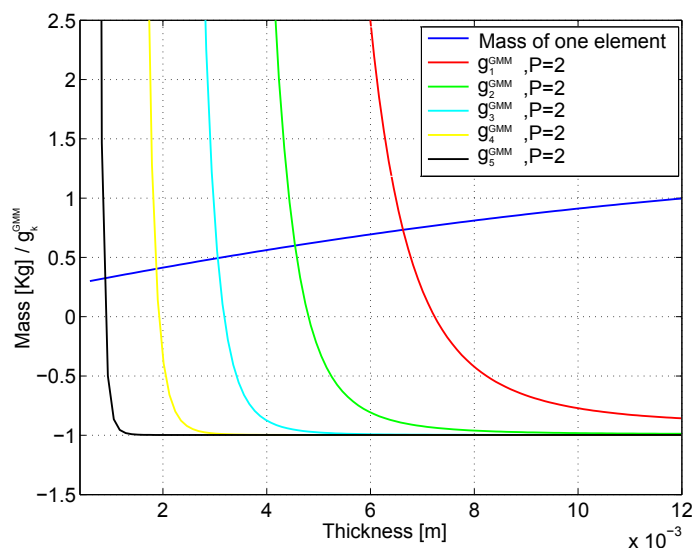


Figure 10.4: Parametric study of the fatigue constraints as a function of the thicknesses with a fixed diameter of 0.04 m.

The adaptive move limit strategy for the optimization problem is defined as:

- For a change in constraint function value larger than 2%, decrease the move limit by 90%.
- For a change in constraint function value less than 5%, increase the move limit by 3%.

These move limits are more restrictive than the move limits used for the diameter optimization since the constraints are found to be steeper in the thickness optimization. The results of the thickness optimization for a diameter 0.04 m can be seen in Table 10.2. These results corresponds well with the parametric study in Figure 10.4.

Element no.	Thickness [m]	g_k^{GMM}
1	0.0081	-0.45
2	0.0056	-0.70
3	0.0038	-0.80
4	0.0023	-0.83
5	0.0011	-0.90

Table 10.2: Optimization results from the thickness optimization with at p-value of 2.

It can be concluded, that only minor differences occur when optimizing the thicknesses compared to the optimization of the diameters. However, the behavior of the cost function is seen to change from linear to non-linear. As for the diameter optimization the optimization algorithm is seen to converge toward the predicted thicknesses. The mass of the optimized model is determined to 2.13 kg, which means a weight reduction of 48% from the initial design is found.

10.1.5 Diameter and Thickness Optimization

In this section a combined optimization of both the thicknesses and diameters are performed. It is not possible to obtain parametric plots of the design space, as made in the preceding sections. Hence, the optimization results are not given beforehand. The p-value is set to 2. The adaptive move limit strategy for both the diameters and thicknesses is defined as:

- For a change in constraint function value larger than 3%, decrease the move limit by 90%.
- For a change in constraint function value less than 1%, increase the move limit by 4%.

The initial and optimized design can be seen in Table 10.3 together with the constraint values. The optimization converges in 71 iterations.

	Start Design		Optimized Design		g_k^{GMM}
	Diameter	Thickness	Diameter	Thickness	
1	0.08	0.004	0.060	0.0031	-0.41
2	0.08	0.004	0.055	0.0029	-0.42
3	0.08	0.004	0.050	0.0028	-0.44
4	0.08	0.004	0.043	0.0025	-0.49
5	0.08	0.004	0.033	0.0023	-0.54

Table 10.3: Results from optimization of both the diameters and thicknesses.

As seen from Table 10.3, both the diameters and thicknesses are decreased during the optimization and the constraints are not violated. Thus, the developed method is seen to be applicable for a combined diameter and thickness optimization.

10.2 Optimization of Jacket Structure

In Appendix K it is seen how the analytical DSA is not capable of providing reliable results whenever different load series are used for the different applied loads as it is the case for the generic jacket structure. Thus, a forward FD approximation is used for the DSA in the following optimization. The optimization of the jacket structure is carried out in order to determine the potential of the mass optimization using the fatigue constraints on a real life structure. Note, only the outer diameters are used as design variables due to high calculation times. The diameters of symmetry groups 12 and 13 are maintained at 1.2 m through the optimization since these are regarded as artificial elements included in the TP. The profile properties of the original jacket structure are defined in Table 2.1. By using an iterative parametric approach a new initial design closer to the optimized solution has been determined. The purpose of determining the new starting point is to reduce the number of optimization iterations needed for convergence and thus the calculation time. The starting point is shown in Table 10.4.

Symmetry group	Outer diameter, [m]	Thickness, [m]
1-2	0.57	0.015
3-6	0.4	0.01
7	0.15	0.005
8	0.17	0.005
9	0.28	0.005
10	0.23	0.005
11	0.2	0.005
12-13	1.2	0.04

Table 10.4: Starting point for the optimization of the jacket model.

The move limits are initialized to 0.4%, while the adaptive move limit strategy for this problem is defined as:

- For a change in constraint function value larger than 5%, decrease the move limit by 90%.
- For a change in constraint function value less than 1%, increase the move limit by 3%.

The convergence tolerance is set to 0.1%, and no upper and lower bounds are set on the design variables. The GMM with a p-value of 5 is applied on each element in order to ensure that no large fluctuations in constraint function

values occur. After the the GMM is used on each element, the maximum constraint function value in each symmetry group is determined and used as the fatigue constraint for the given symmetry group. The gradient of the cost function for each symmetry group is determined from equation (8.1.2), where the contribution from each element in a symmetry group is summed.

Since a forward FD approximation is applied for the DSA the calculation time of each iteration can be assessed from Table 6.2. 13 fatigue constraint gradients must be calculated in each iteration due to the use of 13 symmetry groups containing a total of 13 design variables. Using the forward FD approximation this means the damage in the structure must be determined 14 times. Thus, when 6,000 load sample points is used, the calculation time for the gradient determination alone is in excess of an hour on a standard laptop. As a result, 750 load sample points will be used in the optimization reducing the calculation time of each iteration to approximately 15 minutes. Note, this means an underestimation of the damage of up to 54% must be expected, see Table 6.2.

10.2.1 Results from Optimization of Jacket Model

The results of the optimization can be seen in Table 10.5. The mass of the jacket model is reduced from an initial value of 562,660 kg to 69,554 kg, a reduction of 87.6%. Note, that the original jacket structure has been designed according to offshore standards where high safety factors are used. Furthermore, only a single load case is available and judging from the wind speeds, it does not represent an extreme load case. Adding to this, that a number of design driven topics have been delimited, as seen in section 1.1.1, a large reduction in mass must be expected.

Symmetry Group	Diameter [m]	Thickness [m]	g_k^{GMM}
1	0.54	0.015	-0.54
2	0.28	0.015	-0.99
3	0.29	0.01	-0.28
4	0.22	0.01	-0.61
5	0.19	0.01	-0.99
6	0.30	0.01	-0.64
7	0.002	0.005	-1.0
8	0.095	0.005	-0.07
9	0.10	0.005	-0.33
10	0.12	0.005	-0.99
11	0.11	0.005	-0.01
12	1.2	0.04	-1.0
13	1.2	0.04	-1.0

Table 10.5: Optimization results for the jacket for each symmetry group.

Note, that the profile parameters of Table 10.5 have been determined using just 750 load sample points. As a result, these must be increased when all 60,000 load sample points is used in order for the profiles not to suffer fatigue failure. Studies have shown that even though the damage is underestimated with as much as 54%, the profile properties should only be increased by a few percent in order to have the sufficient fatigue strength. This is a result of the steep constraint functions. From Table 10.5 it is seen that symmetry groups 7, 12, and 13 are not near the fatigue limit for the optimized result. Symmetry groups 12 and 13 were not included in the optimization since they are embedded in the TP. The applied BCs means that the mud braces of symmetry group 7 carry almost no loading. This is recognized from the very small outer diameter of symmetry group 7, which suggest that these elements are redundant. Note, the found profile dimensions for symmetry group seven is not physically possible. However, this has little if any influence, since the mud braces are removed from the optimized design.

The remaining symmetry groups are seen to be close to the fatigue limit. However, a design where all symmetry groups are at the fatigue limit is not obtained due to the used convergence criteria, which is set according to the relative design change. Even though the obtained design is not exactly at the fatigue limit it is accepted as a result of the very steep non-linear behavior of the constraint functions near the fatigue limit. Thus, only neglectable design changes can be found by continuing the optimization.

The percentage reduction in diameter for each symmetry group is illustrated on Figure 10.5.

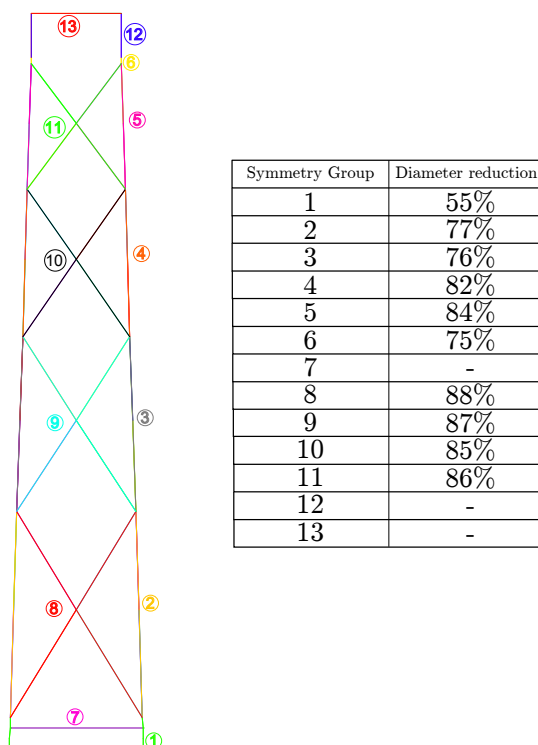


Figure 10.5: The percentage reduction of outer diameters for each symmetry group.

In contrast to the simple beam examples, the design variables in the more complicated structures can influence the damage in several elements. Thus, the direct coupling between an element's design variable and its constraints, as seen for the simple beam examples, will be lost and the gradient matrix will contain off-diagonal terms. Thus, the developed move limit strategy may not be as successful when used on the jacket structure than when used on the simple beam examples.

A study of where the calculation time is spent during the optimization is made in Appendix I. The main conclusion is that 87.5% is spent on computing the gradients, if the gradients are calculated using parallel computing in MATLAB. 12% is spent on computing the damage, while less than a half percent is spent on solving the optimization problem. The calculation time is examined further in Appendix I.

The damage in the cross sectional sample points for the original and optimized design can be seen on Figure 10.6.

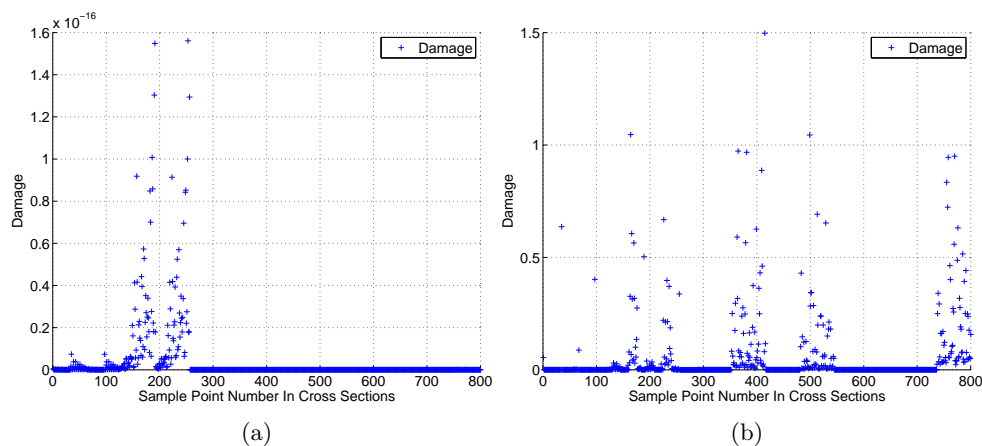


Figure 10.6: The damage determined in each cross sectional sample point of (a) the original design and (b) the optimized design of the jacket model.

From a comparison of Figures 10.6a and 10.6b it is seen that the damage in the cross sectional sample points has been increased for the optimized design as expected. From Figure 10.6b it is seen that the damage in three cross sectional sample points has exceeded the fatigue limit of 1. The three cross sectional sample points belong to symmetry group 3, 8, and 9. However, the violation of the fatigue limits is not seen in the constraint function values for symmetry group 3, 8, and 9, see Table 10.5. Thus, the used p-value of 5 in the GMM must be increased for future optimizations. The damage in symmetry group 1 to 11 may be seen on Figure 10.7 for the original and the optimized design in order to evaluate the optimized design.

From Figure 10.7a it is seen that none of the symmetry groups contain any significant damage in the original design. However, this is changed in the optimized structure as seen on Figure 10.7b. Note, how several of the symmetry groups are now much closer to the fatigue limit of one. The symmetry group closest to the fatigue limit is symmetry group 11. This symmetry group does not contain any damage values above one, which suggests that the overall damage values in the symmetry group are high. The results of Figure 10.7b shows that the diameters of symmetry group 2, 5, and 10 may be lowered even further. However, due to the coupling effects between diameters and damage values in different symmetry groups, the diameters in symmetry groups 8 and 11 might have to be increased in order not to exceed the fatigue limit.

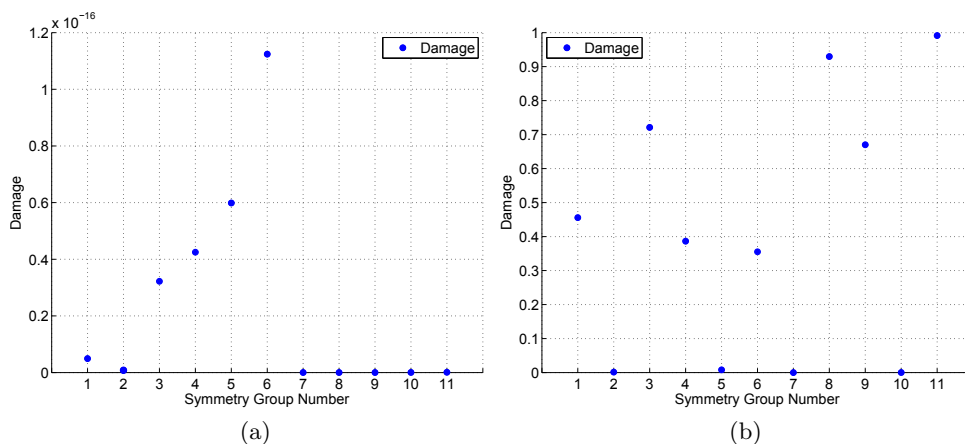


Figure 10.7: The damage value in symmetry groups 1 to 11 for (a) the original jacket design and (b) the optimized jacket design.

It is experienced during the various optimization runs, that different converged designs are found for different chosen starting designs. This hints that the found design of Table 10.5 is a local optimum.

10.3 Sub Conclusion

In order to use a linear optimization algorithm in combination with the steep fatigue constraints a suitable move limit strategy was developed. Optimization performed using the developed move limit strategy in combination with a SLP algorithm proved to yield satisfactory results for both diameter and thickness optimization for the simple beam examples. For the simple benchmark examples the optimized result was seen to converge towards the results predicted by parametric studies.

The GMM was introduced to remove the risk of fluctuations in the fatigue constraint values. From results using the GMM it is recommended to use a p-value between 1 and 8.

An optimization of the jacket structure was carried out using a numerical DSA scheme due to the current deficiencies in the analytical DSA. The developed method was seen to be applicable on a larger real life model, and a local optimum reducing the overall mass with 87% was found. The large mass reduction might be a result of the delimitation made in the project.

Part IV

Evaluation

Chapter 11

Conclusion

The main purpose of the project is to examine the use of gradient based size optimization in correlation with fatigue constraints using non-proportional load spectra, and to determine the most suited methods. One of the main focus areas is to determine the gradients using an analytical approach. The approach, with a numerical DSA, is applied to an OWT support structure in order to examine if the developed method is applicable for a real life product.

A MATLAB FE program is developed in order to perform the structural analysis. A 3D frame element based on Bernoulli-Euler beam theory is implemented. Stresses are determined in a predefined number of cross sectional sample points in the frame elements. The MATLAB FE program is verified by a result comparison to ANSYS and analytical results. It can be concluded, that the MATLAB FE program yields reliable stress results.

The accumulated damage estimation is based on Wöhler curves and a modified Goodman diagram. The rainflow count method is chosen as the cycle count method for the various non-proportional spectra. Three different sorting algorithms are developed to sort the stresses after the rainflow count. A successful sorting of the counted stress results will ease both the damage estimation and the DSA. The equivalent damage approach is preferred over the average damage and maximum damage approaches since fewer intervals can be used. Finally, the Palmgren-Miner damage rule is applied to determine the accumulated damage. It is seen, how the overall calculation time can be reduced by sampling the load spectra with a lower frequency than the original spectra. However, this introduces an underestimation of the damage, which the user should be aware of. It is verified, that the structural analysis has

been implemented properly.

The full derivatives of the damage w.r.t. design variables can be determined by an OFD approximation or analytically by the DDM or the AM.

The analytical DSA must be split into separate damage contributions from an amplitude stress and a mean stress. In its current state the analytical approach is seen to yield unreliable results when using different load series for the applied loads. The current deficiencies are thought to be related to the implemented bookkeeping. However, the analytical methods are seen to be successful for several load cases as well using non-proportional load series. A restriction in the developed method is that it is not applicable for load spectra with a zero mean value due to the shape of the Goodman diagram.

The SLP algorithm is chosen due to its simplicity, transparency, and its ability to handle many design variables. A special adaptive move limit strategy is developed to account for the non-linear fatigue constraints. The GMM is used to cluster several constraint functions in an element or symmetry group. The optimization using the SLP algorithm and the adaptive move limits proved to converge towards the results predicted by the parametric studies for the simple beam examples. An optimization of the generic jacket structure is performed to ensure the developed method is applicable on a real life structure. Symmetry conditions are imposed on the jacket model to reduce the number of design variables. It can be concluded, that the developed method shows great potential when applied on a real life structure.

In excess of 80% of the calculation time during the jacket optimization iterations is spent determining the gradients numerically. The calculation time of the DSA is highly affected by the number of load sample points for both the numerical and analytical approaches.

It should be noted, that the number of sub-function calls and the amount of data which must be stored is significant even for small models and load spectra using the developed method. Some recommendations to the future work are given in the following discussion.

Chapter 12

Discussion

In this project a method of including fatigue constraints in a classical gradient based size optimization problem is sought. The main focus points of this project are chosen to be an analytical DSA as well as the ability to use non-proportional load spectra for the applied loads. As seen in section 8.4 and Appendix K some deficiencies are still present in the analytical DSA, but the ability to handle random amplitude and mean load spectra is achieved for some cases as well. In the following, some suggestions to the further improvement of the developed method is given.

In [Holmberg, 2013, Figure 12(a)] an alternative approach, which might reduce the calculation time of the optimization procedure significantly is suggested. The main difference to the procedure employed in this project is, that the fatigue analysis is moved out of each optimization iteration loop in the alternate approach by determining a stress equivalent and using stress constraints. Thus, the fatigue analysis in this approach is not design dependent. This approach is however only applicable for proportional load series, which does not fulfill the aim in this project.

It is experienced, that the calculation time for each iteration in the optimization of the jacket model is quite high. This is not ideal since a SLP algorithm is applied on the non-linear optimization problem, and a large number of iterations using small design changes must be used as a result. Thus, lowering the calculation time for each iteration would be beneficial. However, no attempts of speeding up the calculations, for instance by applying vectorization or parallel computing, are made.

The overall calculation time may be lowered by a reduction of the applied load spectra. Due to the limited time frame the topic of load series reduction has not been examined.

Fatigue studies have shown that compressive mean stresses in a structure might actually be beneficial for the overall fatigue life of the structure. In this project however, such beneficial effects from a compressive mean stress is disregarded in the Goodman diagram.

In section 8.3 it is explained how the matching of stress- and displacement fields for the analytical DSA is handled. In the bookkeeping it is assumed that a single displacement field may be used for all stress cycles stored in a given interval of the sorted rainflow table, Table 8.1. Due to the simplicity of the beam models this assumption is not violated for the analytical DSA in section 8.4, why reliable results are obtained for this example. However, as different non-proportional load series are applied on larger and more complicated structures the results from the analytical DSA becomes unreliable. This may be a result of the violation of the assumption previously mentioned. Thus, some suggestions to the improvement of the bookkeeping, to ensure a functional analytical DSA for all types of load cases, are given in the following.

Further Work

It is assumed, that the unreliable results from the analytical DSA is caused by the use of a single displacement field for all stress reversals in a given interval. One approach to eliminate this error in the calculations would be to remove the sorted rainflow table and use the beginning time of each stress cycle to find a matching displacement field. However, this approach is not recommended, since the terms $\left(\frac{\partial g_k}{\partial x_j}\right)$ and $\left(\frac{\partial g_k}{\partial U}\right)$ must now be calculated for each stress cycle and not a small finite number of intervals in the sorted rainflow table, which will be computationally heavy. Thus, the method will no longer be applicable on larger load series.

Another approach could be to keep the sorted rainflow table and to determine the displacement field used for each interval by either finding a mean of- or by applying a weighted sum function to all displacement fields matching the stress reversals in the given interval.

As seen from equation (8.2.8) the same displacement field is used as input

to the partial derivative of both the normal- and shear stresses w.r.t. the design variable. Thus, it is assumed that the normal- and shear stress in a given interval occur at the same time. This can however not be guaranteed. As a result, it is recommended to allow for a used of different displacement fields when determining the two partial derivative stress terms.

It can be concluded, that a number of challenges within the field of analytical DSA of fatigue constraints, for use in gradient based optimization, are still present. Hopefully, this first attempt of developing a suitable method for analytical DSA of fatigue constraints may ease the future development of an efficient method, which some day may be applied in the optimization of real life components for all types of load cases.

Bibliography

ANSYS, 2010. ANSYS. *ANSYS Mechanical APDL and Mechanical Applications Theory Reference*. 2010.

Arora, 2012. Jasbir S. Arora. *Introduction to optimum design*. ISBN: 978-0-12-381375-6, 3rd ed. Academic press, 2012.

Cook, Malkus, Plesha, and Witt, 2001. Robert D. Cook, David S. Malkus, Michael E. Plesha, and Robert J. Witt. *Concepts and Applications of Finite Element Analysis*. ISBN: 0-471-35605-0, 4th ed. John Wiley & Sons, 2001.

Dong, Moan, and Gao, 2012. Wenbin Dong, Torgeir Moan, and Zhen Gao. *Fatigue reliability analysis of the jacket support structure for offshore wind turbine considering the effect of corrosion and inspection*. Elsevier press, 2012.

Dym and Shames, 1991. Clive L. Dym and Irving H. Shames. *Energy and Finite Element Methods in Structural Mechanics*. ISBN: 81-224-0749-8, 1st ed. New Age International, 1991.

Frantzis, Battenberg, Bielecki, Bloch, Decker, Hamilton, Karcianas, Madsen, Paidipati, Wickless, and Zhao, 2013. Lisa Frantzis, Lindsay Battenberg, Mark Bielecki, Charlie Bloch, Terese Decker, Bruce Hamilton, Aris Karcianas, Birger Madsen, Jay Paidipati, Andy Wickless, and Feng Zhao. *Offshore Wind Market and Economic Analysis*. Navigant Consulting, Inc, 2013.

Goodno and Gere, 2009. Barry J. Goodno and James M. Gere. *Mechanics of Materials*. ISBN: 0-495-43807-3, 7th ed. Cengage Learning, 2009.

- Haftka and Gürdal, 1992.** Raphael T. Haftka and Zafer Gürdal. *Elements of Structural Optimization*. ISBN: 0-7923-1504-9, 3rd ed. Kluwer Academic Publishers, 1992.
- Holmberg, 2013.** Erik Holmberg. *Stress and fatigue constrained optimization*. Linköping, Sweden, 2013.
- Lund, 2013a.** Erik Lund. *Optimization Course 2013 - Lecture 13: Structural Optimization*. 2013.
- Lund, 2013b.** Erik Lund. *Optimization Course 2013 - Additional note: SLP with Matlab examples*. 2013.
- Michaleris and Tortorelli, 1994.** Panagiotis Michaleris and Daniel A. Tortorelli. *Design Sensitivity Analysis: Overview and Review, from Inverse Problems in Engineering*. 71-103, 1994.
- Nieslony, 2003.** Adam Nieslony.
[http://www.mathworks.com/matlabcentral/fileexchange/3026 – rainflow – counting – algorithm](http://www.mathworks.com/matlabcentral/fileexchange/3026-rainflow-counting-algorithm), 2003.
- Planning, 2013.** *Wind Energy Planning*.
[http://www.windenergyplanning.com/wind – turbine – efficiency/](http://www.windenergyplanning.com/wind-turbine-efficiency/), 2013.
- Rao, 2005.** Singiresu S. Rao. *Mechanical Vibrations, Fourth edition in SI units*. Prentice Hall, 2005.
- Soerensen, Hansen, Klim, and Madsen, 1988.** Stephen Biering Soerensen, Finn Overgaard Hansen, Susanne Klim, and Preben Thalund Madsen. *Struktureret Program Udvikling*. ISBN: 978-87-571-1046-3, 1st ed. Nyt Teknisk Forlag, 1988.
- Standard, 1999.** Dansk Standard. *DS412 - Norm for Stålkonstruktioner*. 1999.
- Stephens, Fatemi, Stephens, and Fuchs, 2001.** Ralph I. Stephens, Ali Fatemi, Robert R. Stephens, and Henry O. Fuchs. *Metal Fatigue in Engineering*. ISBN: 0-471-51059-9, 2nd ed. Wiley-Interscience Publication, 2001.

Vorpahl, Popko, and Kaufer, 2011. Fabian Vorpahl, Wojciech Popko, and Daniel Kaufer. *Description of a basic model of the "UpWind reference jacket" for code comparison in the OC4 project under IEA Wind Annex XXX.* 2011.

Zhou, Xiong, Zhao, Fleury, and Shyy, 2009. Ming Zhou, Cheng-An Xiong, Kang Zhao, Raphael Fleury, and Yaw-Kang Shyy. *Structural Optimization Considering Fatigue Requirements.* Altair Engineering, Irvine, California, USA, 2009.

Part V

Appendix

Appendix A

Load Case

This appendix has the purpose of introducing the load case for the jacket structure. The load spectrum is found by a multi body analysis as explained in section 2.2. The load case consist of two forces and two moments applied in the top center of the TP, P_x, P_y, M_x and M_y , respectively. These together with the wind spectrum are presented on the following figures.

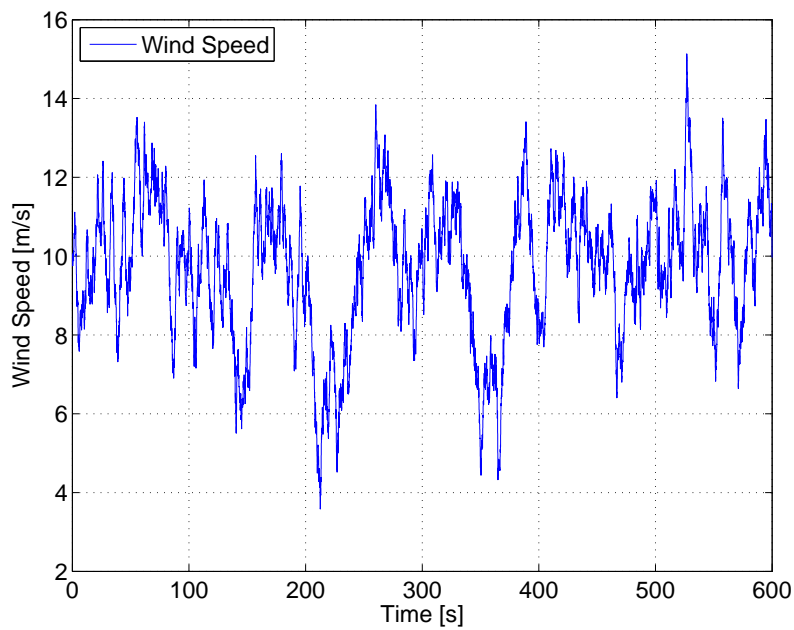


Figure A.1: Wind spectrum.

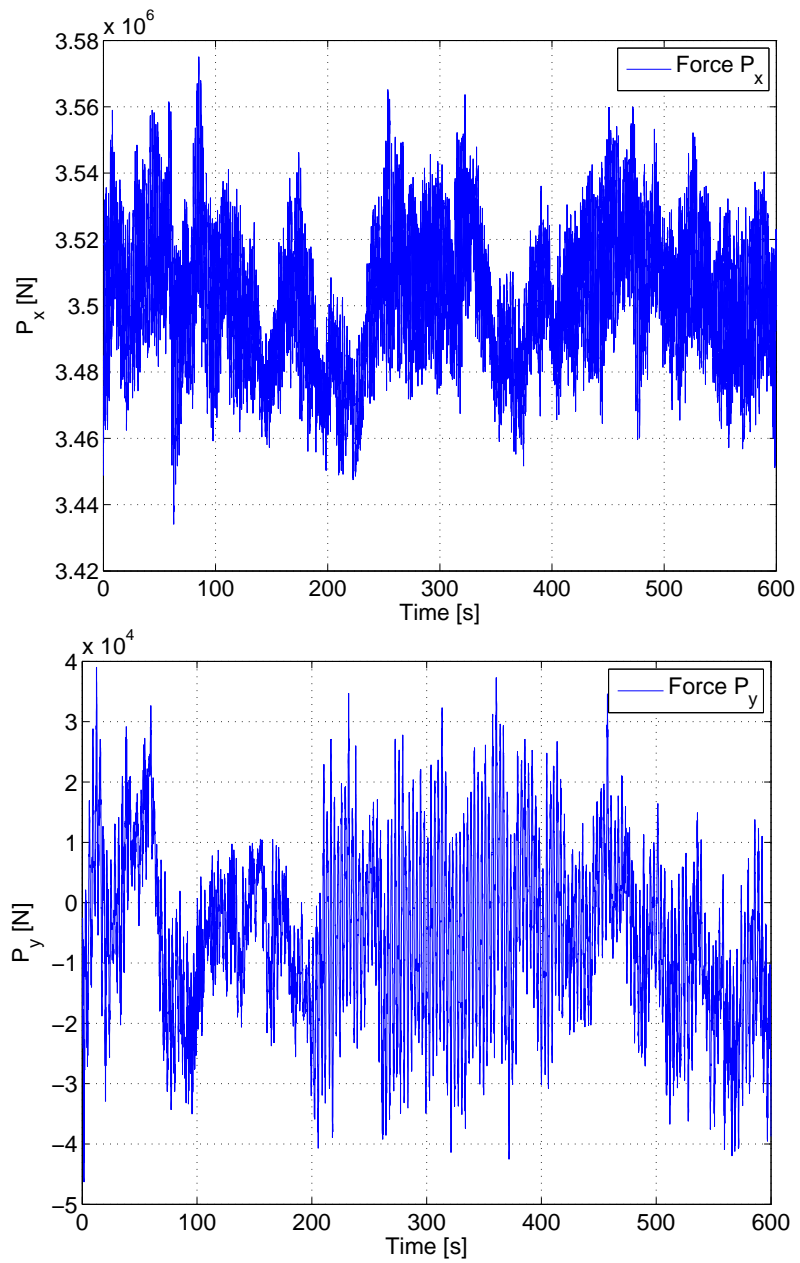


Figure A.2: The measured forces in the X- and Y-direction. The mean force for X-direction is 3,500 kN, while the mean force in the Y-direction is -4.05 kN.

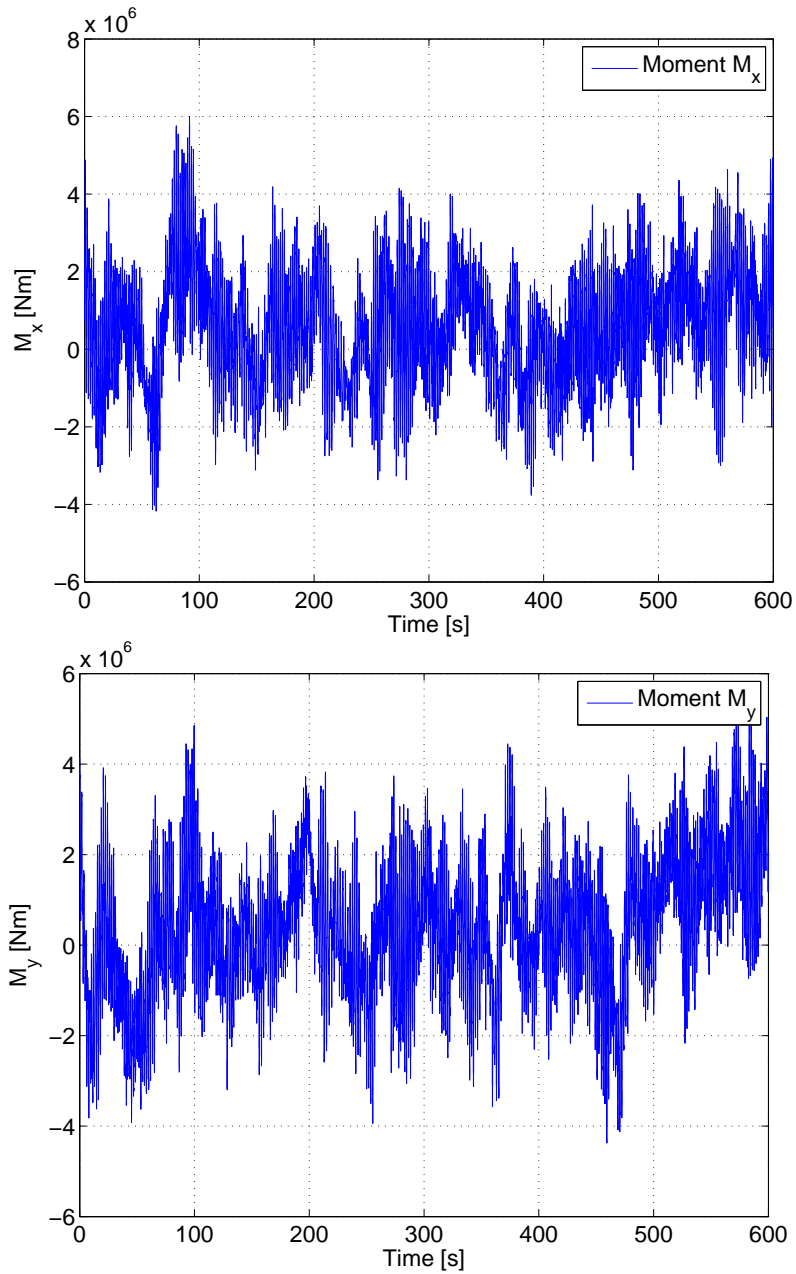


Figure A.3: The measured moment around the X- and the Y-axes. The mean moment for X-direction is 756 kNm, while the mean moment in the Y-direction is 3,408 kNm.

Appendix B

Program

The functionalities of the developed MATLAB FE program is described in the following appendix. Furthermore, the program structure of an example main file and some sub-functions for the DSA are illustrated by the use of flowcharts. An example setup of an analytical DSA may be found on the enclosed CD.

B.1 Program Functionalities

The program functionalities are presented in the following to give the user an overview of the possibilities in the developed program. Various analysis settings may be chosen by the user in the MATLAB FE program. These are listed as:

- Number of cross sectional sample points.
- Number of load sample points.
- Angle offset for cross sectional sample points, $\alpha_{Initial}$.
- Perturbation for the FD approximations.
- The choice of load case: $P_x, P_y, P_z, M_x, M_y, M_z$.

The program is capable of computing the following:

- Displacements.
- Stresses.
- Damage.
- Eigenfrequencies.
- Design sensitivities:
 - Forward FD.
 - Central FD.
 - Analytical AM.
 - Analytical DDM.
- Size optimization.
- Aggregated Function:
 - Generalized mean method.

Furthermore, material model settings may be defined by the user in case the material must be altered. Different material parameters may be used for normal- and shear stresses.

B.2 Program Flow Charts for DSA

This section has the purpose of presenting the program structure, exemplified for a main function and for the OFD and analytical DSAs. The program structure is illustrated by the use of flowcharts where calls of the various sub-functions are highlighted. An example of a main function can be seen in Figure B.1. The functions for the DSA are shown by Figures B.2, B.3, and B.4 for the overall FD approach, the AM, and the DDM, respectively.

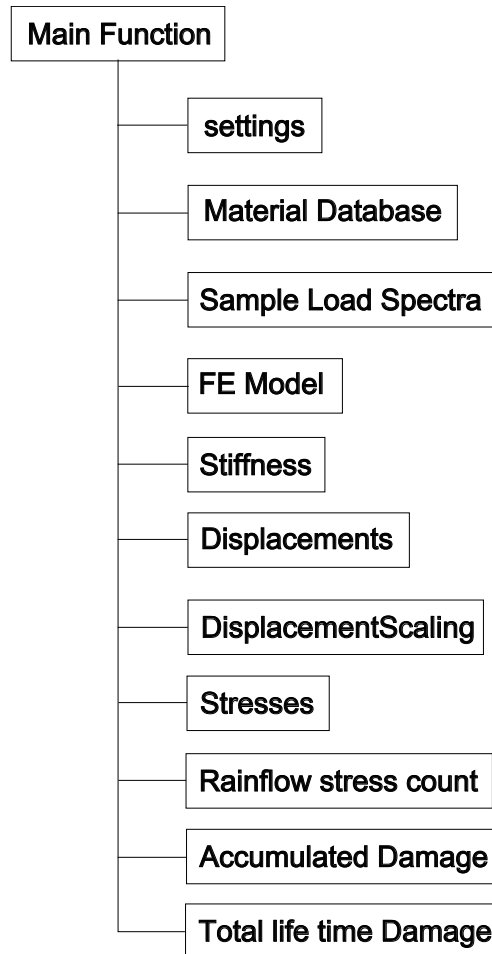


Figure B.1: Flowchart illustrating an example main function of the MATLAB program capable of determining the accumulated damage in a model.

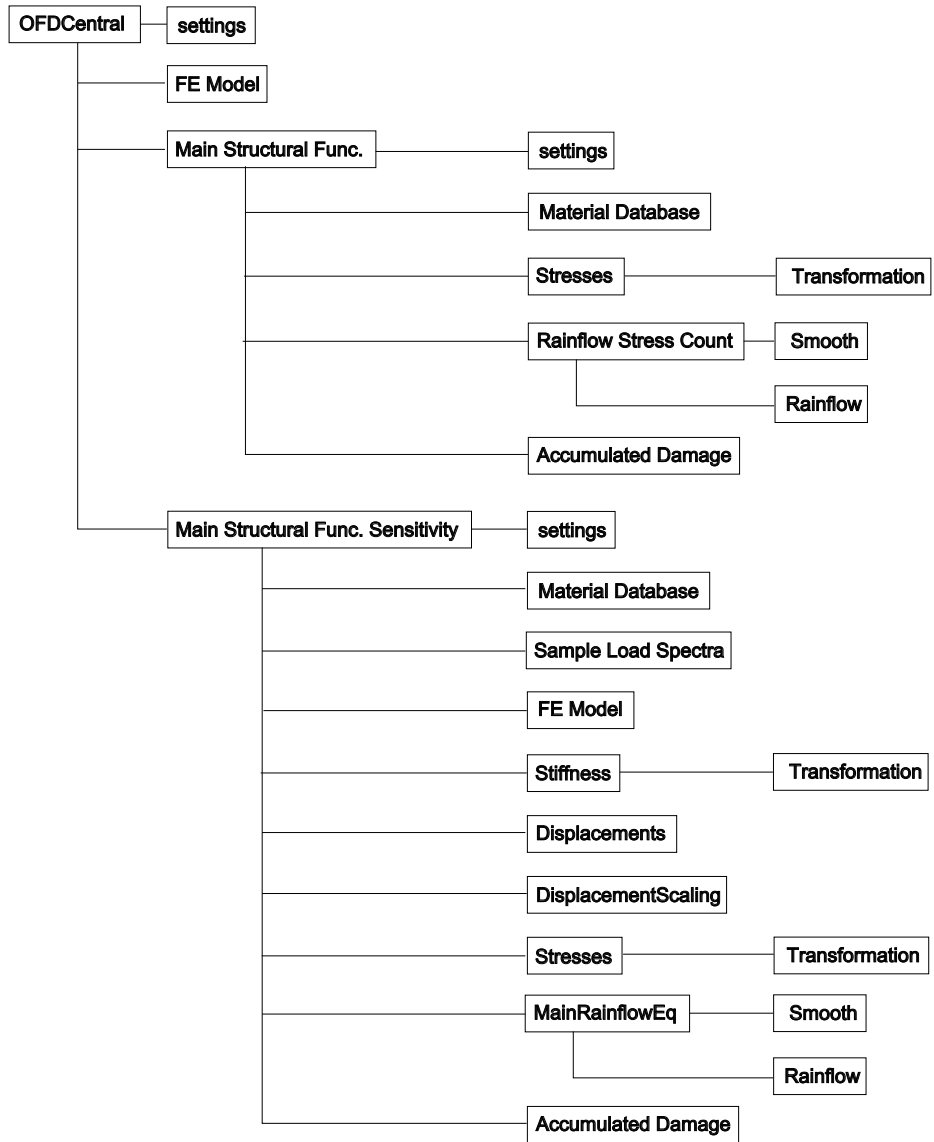


Figure B.2: Flowchart for the OFD function of the MATLAB program.

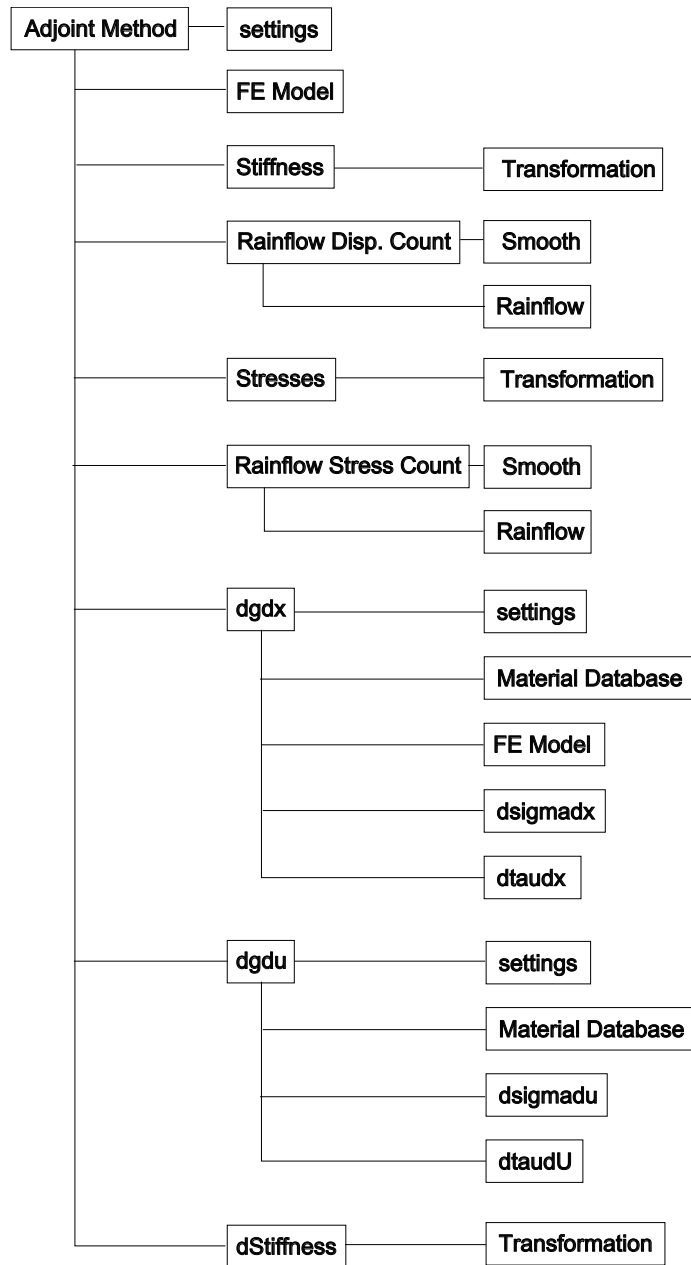


Figure B.3: Flowchart for the AM function of the MATLAB program.

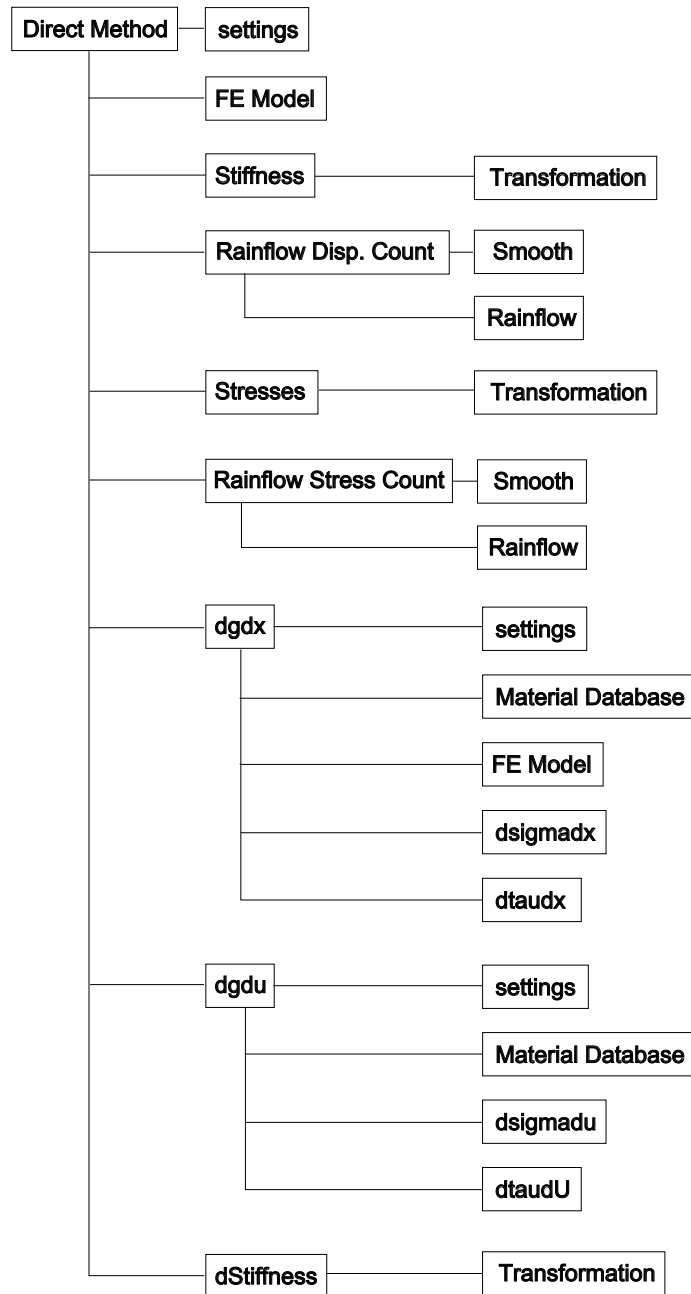


Figure B.4: Flowchart for the DDM function of the MATLAB program.

Appendix C

Finite Element Analysis

The local element stiffness matrix, \mathbf{K}'_e is derived in the following. Furthermore, the transformation from local to global coordinate system using transformation matrices and the procedure for finding normal and shear stresses are described.

Axial stiffness

The axial stiffness of the 3D frame element can be found by considering a two-node bar element with only axial displacements, u'_1 and u'_2 . The bar element is illustrated in Figure C.1.

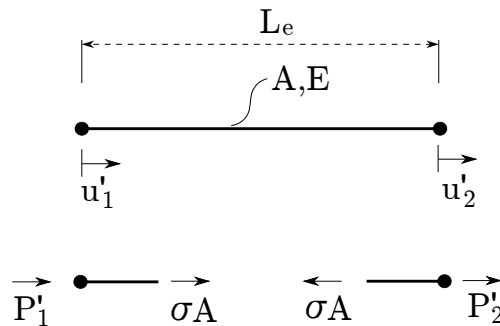


Figure C.1: Two-node bar element and force equilibrium, [Cook et al., 2001, Figure 2.2-1].

From the two nodal displacements u'_1 and u'_2 the strain in the bar element can be determined as:

$$\epsilon = \frac{(u'_2 - u'_1)}{L_e} \quad (\text{C.0.1})$$

from which the axial stress may be found:

$$\sigma_{axial} = E \cdot \epsilon = \frac{E}{L_e} (u'_2 - u'_1) \quad (\text{C.0.2})$$

Two force equilibrium equations can be set up based on Figure C.1.

$$P'_1 + \frac{AE}{L_e} (u'_2 - u'_1) = 0 \quad P'_2 - \frac{AE}{L_e} (u'_2 - u'_1) = 0 \quad (\text{C.0.3})$$

On matrix vector form the two equilibrium equations may be written:

$$\begin{Bmatrix} P'_1 \\ P'_2 \end{Bmatrix} = \frac{AE}{L_e} \begin{bmatrix} 1 & -1 \\ -1 & 1 \end{bmatrix} \cdot \begin{Bmatrix} u'_1 \\ u'_2 \end{Bmatrix} \quad (\text{C.0.4})$$

The axial stiffness of the bar element has thus been determined to $\frac{AE}{L_e}$. Note, that the element should only be used for small deformations due to the use of Cauchy's linear strain definition, equation (C.0.1). Next, the torsional stiffness of the element may be determined.

Torsional stiffness

A twist along the element may occur when the two DOFs: θ'_{x1} and θ'_{x2} are not equal. The torsional stiffness of a two-node element is much similar to the axial stiffness of the element, and will thus not be derived here.

The torsional stiffness linking the twist to a torsional moment, for a circular cross section, may be written as, [Cook et al., 2001, P. 27]:

$$\begin{Bmatrix} M'_{x1} \\ M'_{x2} \end{Bmatrix} = \frac{GI_p}{L_e} \begin{bmatrix} 1 & -1 \\ -1 & 1 \end{bmatrix} \begin{Bmatrix} \theta'_{x1} \\ \theta'_{x2} \end{Bmatrix} \quad (\text{C.0.5})$$

Thus, the torsional stiffness of the two-node element has been determined to $\frac{GI_p}{L_e}$. Note, the use of the polar moment of inertia is only valid for circular cross sections like a solid circular bar or a tube. Next, the bending stiffness is examined.

Bending stiffness

A two-node beam element is used for the determination of the bending stiffness. The beam element is based on Bernoulli-Euler theory, which means transverse shear deformation is neglected. Thus, this element should only be

used for long slender beams. Bending around the z' -axis of the element is considered first. The two-node beam element has the four DOFs:

$$\bar{U}' = [v'_1 \ \theta'_{z1} \ v'_2 \ \theta'_{z2}]^T$$

Two translations in the y' -direction and two rotations around the z' -axis. By applying a unit displacement to each of the four DOFs, one by one, the four displacement curves seen in Figure C.2, can be obtained.

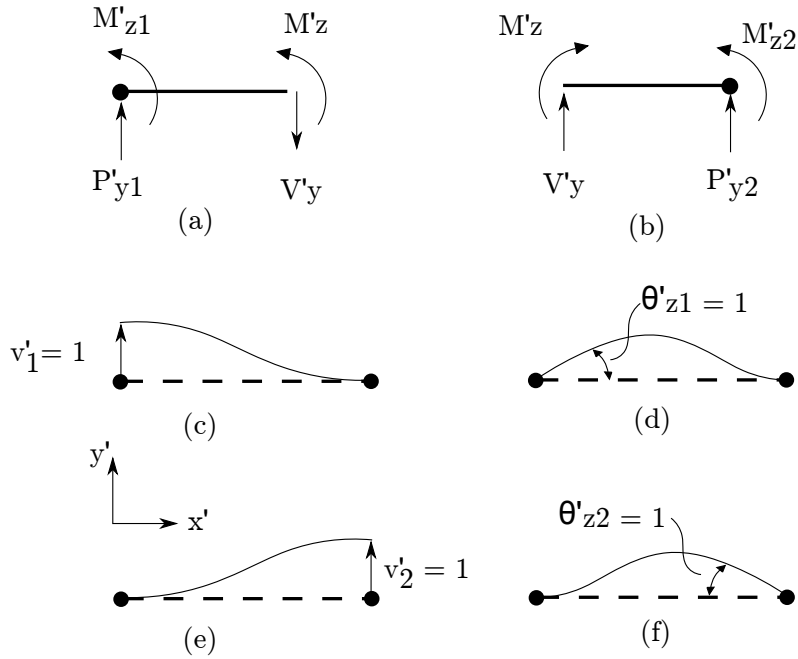


Figure C.2: (a) FBD near node 1, (b) FBD near node 2, (c) Unit displacement on v'_1 , (d) Unit displacement on θ'_{z1} , (e) Unit displacement on v'_2 , (f) and unit displacement on θ'_{z2} , [Cook et al., 2001, Figure 2.3-1]

From elementary beam theory the displacement curves to each of the four unit displacements may be determined to:

$$\begin{aligned} v'_c &= 1 - \frac{3x'^2}{L_e^2} + \frac{2x'^3}{L_e^3} & v'_d &= x' - \frac{2x'^2}{L_e} + \frac{x'^3}{L_e^2} \\ v'_e &= \frac{3x'^2}{L_e^2} - \frac{2x'^3}{L_e^3} & v'_f &= -\frac{x'^2}{L_e} + \frac{x'^3}{L_e^2} \end{aligned} \quad (C.0.6)$$

where the subscripts refer to the given displacement curve in Figure C.2. These four displacement curves are equal to the shape functions of the beam

element, [Cook et al., 2001, P. 90].

The moment and the shear force may be expressed from:

$$M'_z = EI_z \frac{d^2 v'}{dx'^2} \quad V'_y = \frac{dM'_z}{dx'} = EI_z \frac{d^3 v'}{dx'^3} \quad (\text{C.0.7})$$

By using the displacement curves presented in equation (C.0.6), the expressions for the moment around the Z-axis and the shear force may be determined:

$$\begin{aligned} M'_z &= EI_z \left(\left(-\frac{6}{L_e^2} + \frac{12x'}{L_e^3} \right) v'_1 + \left(-\frac{4}{L_e} + \frac{6x'}{L_e^2} \right) \theta'_{z1} + \left(\frac{6}{L_e^2} - \frac{12x'}{L_e^3} \right) v'_2 \right. \\ &\quad \left. + \left(-\frac{2}{L_e} + \frac{6x'}{L_e^2} \right) \theta'_{z2} \right) \\ V'_y &= EI_z \left(\frac{12}{L_e^3} v'_1 + \frac{6}{L_e^2} \theta'_{z1} - \frac{12}{L_e^3} v'_2 + \frac{6}{L_e^2} \theta'_{z2} \right) \end{aligned} \quad (\text{C.0.8})$$

From these two expressions the shear force and moment in nodes 1 and 2, and thus the bending stiffnesses of the 2D beam element, may be determined.

From Figure C.2(a) and C.2(b), the two force equilibriums and the two moment equilibriums seen in equation (C.0.9) can be found.

$$\begin{aligned} P'_{y1} &= V'_y & P'_{y2} &= -V'_y \\ M'_{z1} &= -M'_z|_{x'=0} & M'_{z2} &= M'_z|_{x'=L_e} \end{aligned} \quad (\text{C.0.9})$$

Note, that the expressions for the bending moment must be evaluated at $x' = 0$ for node 1 and $x' = L_e$ for node 2 in order to determine the bending moment at the node location.

An assembly of the equations combining nodal displacements to nodal forces and moments yields the 4x4 stiffness matrix for the 2D beam element:

$$\begin{Bmatrix} P'_{y1} \\ M'_{z1} \\ P'_{y2} \\ M'_{z2} \end{Bmatrix} = EI_z \begin{bmatrix} \frac{12}{L_e^3} & \frac{6}{L_e^2} & -\frac{12}{L_e^3} & \frac{6}{L_e^2} \\ \frac{6}{L_e^2} & \frac{4}{L_e} & -\frac{6}{L_e^2} & \frac{2}{L_e} \\ -\frac{12}{L_e^3} & -\frac{6}{L_e^2} & \frac{12}{L_e^3} & -\frac{6}{L_e^2} \\ \frac{6}{L_e^2} & \frac{2}{L_e} & -\frac{6}{L_e^2} & \frac{4}{L_e} \end{bmatrix} \begin{Bmatrix} v'_1 \\ \theta'_{z1} \\ v'_2 \\ \theta'_{z2} \end{Bmatrix} \quad (\text{C.0.10})$$

For bending around the y'-axis, the moment and shear expressions of equation (C.0.8), may be reused with reversed signs on the rotational terms, and the DOFs: $\bar{U}' = [w'_1 \ \theta'_{y1} \ w'_2 \ \theta'_{y2}]^T$. This leads to the following set of equations:

$$\begin{Bmatrix} P'_{z1} \\ M'_{y1} \\ P'_{z2} \\ M'_{y2} \end{Bmatrix} = EI_y \begin{bmatrix} \frac{12}{L_e^3} & -\frac{6}{L_e^2} & -\frac{12}{L_e^3} & -\frac{6}{L_e^2} \\ -\frac{6}{L_e^2} & \frac{4}{L_e} & \frac{6}{L_e^2} & \frac{2}{L_e} \\ -\frac{12}{L_e^3} & \frac{6}{L_e^2} & \frac{12}{L_e^3} & \frac{6}{L_e^2} \\ -\frac{6}{L_e^2} & \frac{2}{L_e} & \frac{6}{L_e^2} & \frac{4}{L_e} \end{bmatrix} \begin{Bmatrix} w'_1 \\ \theta'_{y1} \\ w'_2 \\ \theta'_{y2} \end{Bmatrix} \quad (\text{C.0.11})$$

The bending stiffness for rotations around the y' - and the z' -axis have thus been determined. Next, the 3D transformation matrix is assembled.

C.1 Transformation Matrix

In the 3D beam program used for the FE analysis of the structure, transformations between different local to global coordinate systems are used multiple times. In the following, a method for finding the 3D transformation matrix will be discussed.

In 2D dimensions, rotation from global to local coordinates may be carried out by the well-known 3x3 matrix seen in equation (C.1.1),

$$\mathbf{T}_z = \begin{bmatrix} \cos(\theta) & \sin(\theta) & 0 \\ -\sin(\theta) & \cos(\theta) & 0 \\ 0 & 0 & 1 \end{bmatrix} \quad (\text{C.1.1})$$

since rotations are always around the z' -axis in 2D, and coordinates are thus always in the same plane. This is however not the case for a 3D analysis. Consider the beam element in Figure C.3 and its local coordinate system.

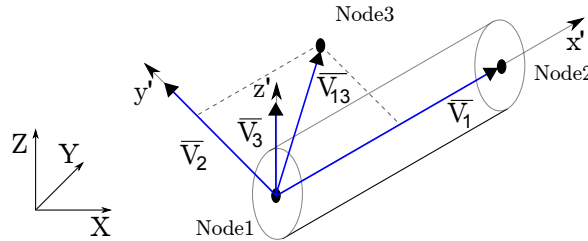


Figure C.3: A 3D frame element and the three nodes defining its local coordinate system according to the global coordinate system, (X, Y, Z) .

For the 3D frame element seen in Figure C.3 the local x' -axis will always be defined as going from Node1 to Node2. The coordinates of Node1 is (x'_1, y'_1, z'_1) and (x'_2, y'_2, z'_2) for Node2. In order to define the y' - and z' -axes a third node,

which define the x'y'-plane, must be included. If this third node is not included the y'- and z'-axes can rotate freely around the x'-axis. Note, that no DOFs and no stiffness are associated with the third node of the element. Its only purpose is to define the local coordinate system of the element.

From the coordinates of the three nodes, two vectors \overline{V}_1 and \overline{V}_{13} , may be found:

$$\overline{V}_1 = \begin{Bmatrix} x'_2 - x'_1 \\ y'_2 - y'_1 \\ z'_2 - z'_1 \end{Bmatrix} \quad \overline{V}_{13} = \begin{Bmatrix} x'_3 - x'_1 \\ y'_3 - y'_1 \\ z'_3 - z'_1 \end{Bmatrix}$$

From the cross product between \overline{V}_1 and \overline{V}_{13} the vector along the local z'-axis, \overline{V}_3 may be determined. The cross product between the newly found \overline{V}_3 vector and the \overline{V}_1 vector will give the vector \overline{V}_2 along the local y'-axis:

$$\overline{V}_3 = \overline{V}_1 \times \overline{V}_2 \quad \overline{V}_2 = \overline{V}_3 \times \overline{V}_1$$

Three vectors defining the local x'y'z'-coordinate system have thus been determined from the three nodes. By dividing with the length of each individual vector, the local coordinate system may be described by the three unit vectors: \overline{e}_1 , \overline{e}_2 , and \overline{e}_3 :

$$\overline{e}_1 = \frac{\overline{V}_1}{|\overline{V}_1|} \quad \overline{e}_2 = \frac{\overline{V}_2}{|\overline{V}_2|} \quad \overline{e}_3 = \frac{\overline{V}_3}{|\overline{V}_3|}$$

where $|\overline{x}|$ denotes the length of the vector \overline{x} . The columns of the 3x3 transformation matrix can now be assembled from the unit vectors as:

$$\mathbf{T}_{3x3} = [\overline{e}_1 \quad \overline{e}_2 \quad \overline{e}_3] \quad (\text{C.1.2})$$

In the MATLAB beam program, the transformation matrix is used to transform entries of the local stiffness matrix to entries of the global stiffness matrix, and later to transform global displacements of two nodes to local displacements. The global displacements of two nodes yields a total of 12 DOFs, and the dimensions of the local stiffness matrix is 12x12, see Figure 4.2. This means that the 3x3 rotations matrix found in equation (C.1.2) must be expanded to a 12x12 matrix. This is done following the procedure shown in equation (C.1.3).

$$\mathbf{T}_{12x12} = \begin{bmatrix} \mathbf{T}_{3x3} & 0 & 0 & 0 \\ 0 & \mathbf{T}_{3x3} & 0 & 0 \\ 0 & 0 & \mathbf{T}_{3x3} & 0 \\ 0 & 0 & 0 & \mathbf{T}_{3x3} \end{bmatrix} \quad (\text{C.1.3})$$

Note, not every zero entry is represented. Next, the normal and shear stresses in the cross sectional sample points are determined.

C.2 Normal Stresses

Two stress components contribute to the normal stress in the cross sectional sample points. These are the axial stress calculated from the normal forces and the bending stresses determined from the bending moments. The axial stress may be found by multiplying the axial strain with Young's modulus. That is not shown in this appendix.

The normal stress from the applied bending moment is determined from the bending formula:

$$\sigma = -\frac{M \cdot h}{I} \quad (\text{C.2.1})$$

where h is the distance from the neutral axis to the sampling point. The second area moment of inertia and the thickness for a hollow circular cross section are given by [Goodno and Gere, 2009, P. 398]:

$$I_y = I_z = \frac{\pi}{4}(r_2^4 - r_1^4) = \frac{\pi}{4} \left((d/2)^4 - (d/2 - t)^4 \right) \quad (\text{C.2.2})$$

$$t = r_2 - r_1 \quad d = 2r_2 = 2(r_1 + t) \quad (\text{C.2.3})$$

where r_1 is the inner radius and r_2 is the outer radius.

The bending moments in each node are determined from:

$$M_y = EI_y \frac{d^2 w}{dx'^2} \quad M_z = EI_z \frac{d^2 v}{dx'^2} \quad (\text{C.2.4})$$

The z' - and y' -coordinates of the cross sectional sample points, used for h in equation (C.2.1) must be determined. The coordinates are calculated from the outer diameter d in order to determine the maximum bending moment in the sample points. The coordinates to the cross sectional sample points may be found from:

$$y' = \frac{d}{2} \cos(\alpha + \alpha_{Initial}) \quad z' = \frac{d}{2} \sin(\alpha + \alpha_{Initial}) \quad (\text{C.2.5})$$

Results from equation (C.2.5) can be compared to Figure 4.3a.

Having determined the sample point coordinates, the normal stress in each cross sectional sample point may be determined by a superposition of the normal stresses:

$$\sigma(x', y') = \sigma_{axial} - \frac{M_y \cdot z'}{I_y} - \frac{M_z \cdot y'}{I_z} \quad (\text{C.2.6})$$

For the sign convention to be correct, the moments must be applied positive according to the right hand rule, and the coordinates calculated positive according to the axes seen in Figure 4.3a. Next, the shear stresses in the cross sectional sampling points are examined.

C.3 Shear Stresses

Three load parameters contribute to the shear stress in the cross sectional sampling points. These are the applied torsional moment T and the shear forces V_y and V_z . Since the cross section of the tubes are circular, the torsional moment can be determined by:

$$T = GI_p \frac{\theta_{x2}' - \theta_{x1}'}{L} \quad (\text{C.3.1})$$

Similarly, the shear forces are determined as:

$$V_z = EI_y \frac{d^3 w}{dx'^3} \quad V_z = EI_z \frac{d^3 v}{dx'^3} \quad (\text{C.3.2})$$

The shear stresses stemming from the shear force may be determined from the shear formula, [Goodno and Gere, 2009, P. 391]:

$$\tau_y = \frac{V_y \cdot Q}{I_z \cdot 2t} \quad (\text{C.3.3})$$

Note, that the shear stress is assumed to be constant through the thickness of the cross section since the thicknesses are small compared to the diameters. For the hollow circular beam cross sections used in this project, the shear force, the wall thickness, and the moment of inertia will be constant over the entire cross section. This means these values may be reused for the different cross sectional sample points. The first area moment, Q however, will vary depending on which cross sectional sample point is used. This may be illustrated from Figure C.4a.

Note, that the angle β and not α is used to define the first area moment. β is defined between zero and $\frac{\pi}{2}$. By using the symmetry of the cross section around the y' - and z' -axis, the first area moment for all cross sectional sample points may be defined from the β -angle. A section of the tube is thought to be cut free at the position of the cross sectional sampling point, illustrated by the dashed line in Figure C.4a. For a variation in applied moments, a shear force must be present on the two cut surfaces in order to obtain equilibrium,

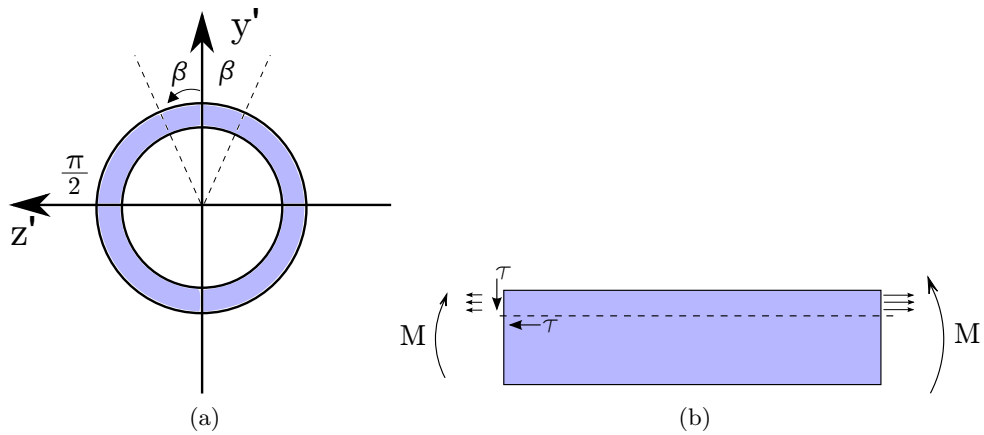


Figure C.4: (a) The hollow circular cross section. (b) The variation in applied moments leading to a shear stress on the cross sectional surface as a results of force equilibrium.

see Figure C.4b. This may also be recognized from $V = \frac{dM}{dx}$. The shear force on the cut surface will lead to a shear stress. Since shear stresses flow around corners, a shear stress must be present on the surface of the cross section as well, illustrated by τ on Figure C.4b.

The shear stress will however not be constant on the cross section surface, since the first area moment, used in equation (C.3.3) will vary depending on where the section cut is made. This is illustrated by Figure C.5.

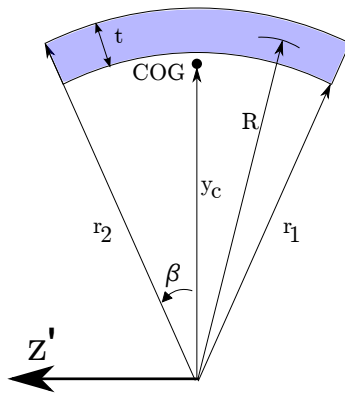


Figure C.5: The area cut free from the remaining cross section used to determine the first area moment, Q .

As the β -angle changes the distance from the z' -axis to the section Center

of Gravity (COG), denoted y_c and the area of the section cut loose will change as well. These two components make up the first area moment:

$$Q = \int y_c dA \quad (\text{C.3.4})$$

The angle-dependent distance from the z' -axis to the section COG and the angle-dependent area are given as, [Goodno and Gere, 2009, P. 945]:

$$A(\beta) = 2\beta Rt \quad y_c(\beta) = \frac{R \cdot \sin \beta}{\beta} \quad (\text{C.3.5})$$

where R is the radius to the centerline of the circular hollow cross section defined as:

$$R = r_2 - \frac{r_2 - r_1}{2}$$

By the use of the two equations in (C.3.5) the angle-dependent first area moment of the cut section may be written:

$$Q(\beta) = \frac{R \cdot \sin(\beta)}{\beta} \cdot 2\beta Rt \quad (\text{C.3.6})$$

The angle-dependency of the distance to the COG and the first area moment may be seen in Figure C.6. Note, Figure C.6 is made for a diameter of 0.8 m and a thickness of 0.02 m.

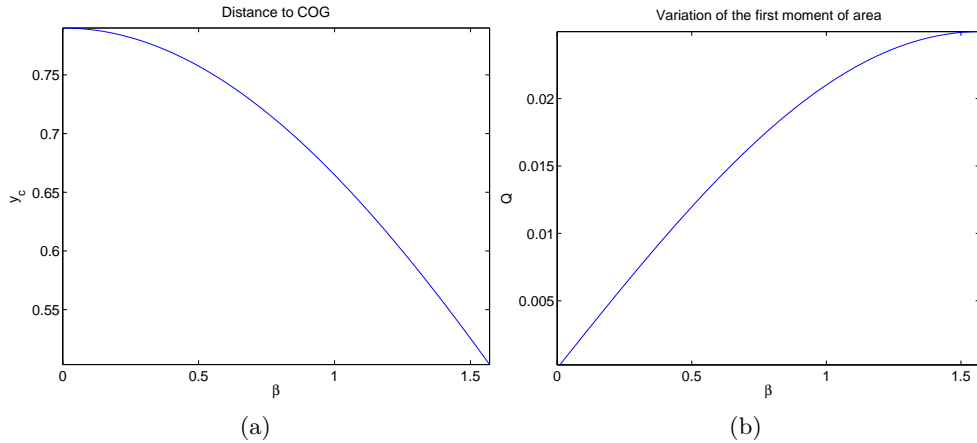


Figure C.6: The angle dependent distribution of: (a) the distance to the COG and (b) the first area moment, Q .

Analytical solutions for the distance to the section COG and the first area moment are present for the case where $\beta = \frac{\pi}{2}$, that is a full half circle. For a

full half circle $y_c(\frac{\pi}{2})$ is determined to 0.503 m, which is represented exact by equation (C.3.5), see Figure C.6a. Naturally, $y_c(0)$ must lie in the centerline between the two radii at 0.79 m, which is seen in Figure C.6a as well. However, this point cannot be determined directly from equation (C.3.5) due to the division by zero.

The first area moment must be zero for $\beta = 0$, leading to a shear stress of zero in this cross sectional location. This is a result of the non-existing area for cross sectional sample point $\beta = 0$. For the full half cycle, the analytical result yields $Q = 0.025 \text{ m}^3$, which is seen to be the same on Figure C.6b. Based on equations (C.3.3) and (C.3.6), the angle-dependent shear stress in the cross sectional sample points may be determined. An identical expression is used for finding the shear stress acting in the z-direction, τ_z . However a phase shift on 90° must be applied.

The exact analytical solution for Q can be obtained for the case of a full half circle as [Goodno and Gere, 2009, p. 398]:

$$Q = \frac{2}{3} (r_2^3 - r_1^3) \quad (\text{C.3.7})$$

Equation (C.3.5) represents the approximate solution, which in contrast can be used for any value of β . The deviation between the case of a full half circle by the approximate and analytical solution for Q can be found for different values of diameters and thicknesses by using (C.3.5) and (C.3.7). By varying the diameter/thickness relationship and determine the deviation, a suitable limit of the relationship for the thicknesses compared to the diameter can be found. It can be seen on Figure C.7, that the deviation is less than 1 percent when the diameter/thickness relationship is 10 or larger. Thus, it can be concluded, that the diameter/thickness relationship should be kept to 10 or larger in order to keep the error sufficiently low.

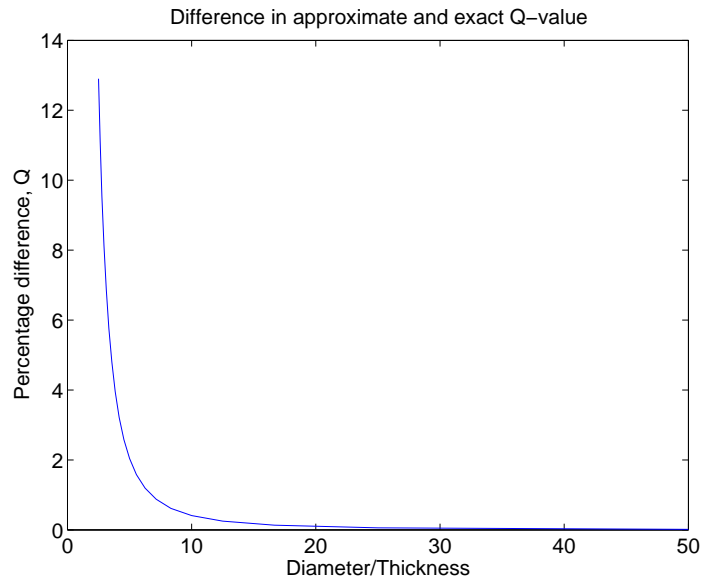


Figure C.7: The deviation between the approximate solution for Q compared to the exact determination of Q for a full half cycle.

The last contributor to the shear stress in the cross sectional sample points is the torsional load, T . The shear stress distribution from an applied torsional moment is illustrated on Figure C.8.

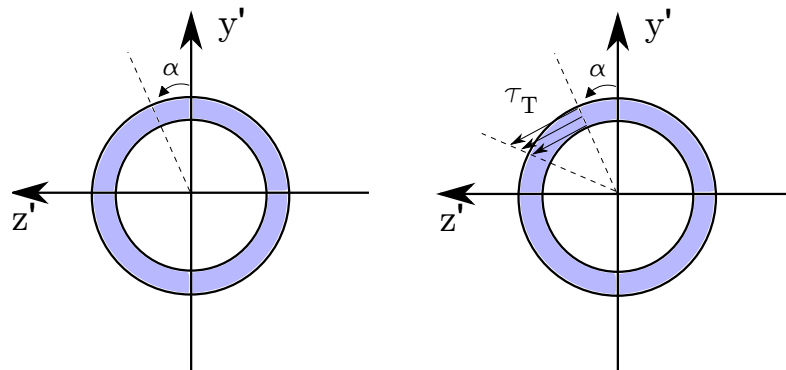


Figure C.8: The sampling locations on the cross section and the torsional shear stress distribution on a circular hollow profile, $\alpha_{Initial} = 0$.

As seen from Figure C.8 the torsional shear stress will always be tangential to the surface of the sample point. The sample point is defined by the angle α in the interval $0 \leq \alpha \leq 2\pi$. The maximum shear stress is determined from:

$$\tau_T = \frac{T \cdot d}{2I_p} \quad (\text{C.3.8})$$

The contribution to the total shear stress in the y' - and z' -direction may be found from:

$$\begin{aligned} \tau_{Ty}(\alpha + \alpha_{Initial}) &= -\tau_T \cdot \sin(\alpha + \alpha_{Initial}) \\ \tau_{Tz}(\alpha + \alpha_{Initial}) &= \tau_T \cdot \cos(\alpha + \alpha_{Initial}) \end{aligned} \quad (\text{C.3.9})$$

This may be verified from Figure C.8.

A superposition of the shear stresses obtained from the two shear forces and the torsional moment will yield the total shear stress in each cross sectional sample point. The total shear stress can be seen in equation (4.3.2). Next, the FE code is verified.

C.4 Verification of FE code

A model of a house with a crane is used for the verification of the 3D FE code, since it contains many details similar to the FE model of the jacket structure. The model is analyzed using both ANSYS and MATLAB. Eigenfrequencies, global displacements, and stresses will be compared in order to verify the FE code. The analysed model is shown on Figure C.9. The analyzed model consists of 16 elements sharing a total of 11 nodes. All elements have the same cross section geometry with an outer diameter of 0.1 m and a thickness of 0.02 m. An arbitrary chosen load on -100 kN is applied in the Y-direction on node 11.

C.4.1 Eigenfrequencies

The eigenfrequencies of a structure may be determined from the global mass and stiffness matrices. Thus, by comparing the eigenfrequencies found using MATLAB to the eigenfrequencies found by ANSYS, the set up of the global stiffness and mass matrix can be verified.

The material properties are set to $\rho = 7800 \frac{\text{kg}}{\text{m}^3}$, $E = 210$ GPa, and $\nu = 0.3$ in both programs. The local 12x12 mass matrix for the frame element can be seen in Figure C.10, [ANSYS, 2010, BEAM4 3-D Elastic Beam]. The assembly of the global mass matrix from the local mass matrix is much like the assembly of the global stiffness matrix from several local stiffness matrices.

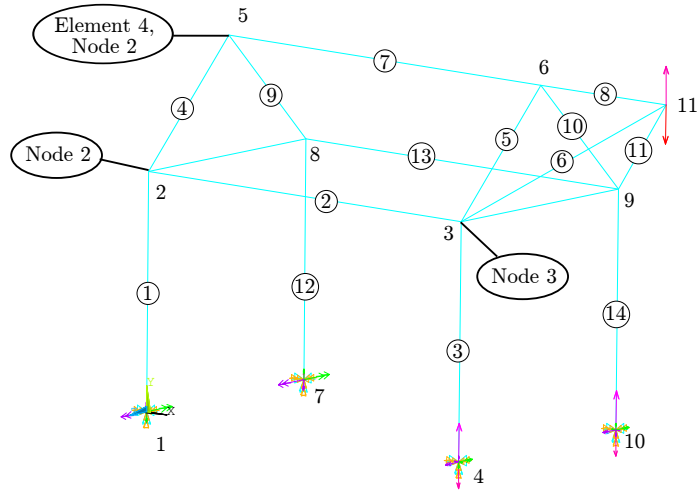


Figure C.9: The 3D model of a house with a crane mounted in one end is used for the validation of results obtained from the MATLAB FE analysis. Node numbers 1-11 are marked by numbers, while the element numbers are marked with encircled numbers.

$$\begin{array}{c}
 \left[\begin{array}{cccccc}
 \frac{1}{3} \cdot M_e & 0 & 0 & 0 & 0 & 0 \\
 0 & \left(\frac{13}{35} + \frac{6}{5} \cdot \frac{r_g}{L_e^2} \right) \cdot M_e & 0 & 0 & 0 & \left(\frac{11L_e}{210} + \frac{L_e}{10} \cdot \frac{r_g}{L_e^2} \right) \cdot M_e \\
 0 & 0 & \left(\frac{13}{35} + \frac{6}{5} \cdot \frac{r_g}{L_e^2} \right) \cdot M_e & 0 & - \left(\frac{11L_e}{210} + \frac{L_e}{10} \cdot \frac{r_g}{L_e^2} \right) \cdot M_e & 0 \\
 0 & 0 & 0 & \frac{I_p}{3 \cdot A} \cdot M_e & 0 & 0 \\
 0 & 0 & 0 & 0 & \left(\frac{L_e^2}{105} + \frac{2 \cdot L_e^2}{15} \cdot \frac{r_g}{L_e^2} \right) \cdot M_e & 0 \\
 0 & 0 & 0 & 0 & 0 & \left(\frac{L_e^2}{105} + \frac{2 \cdot L_e^2}{15} \cdot \frac{r_g}{L_e^2} \right) \cdot M_e
 \end{array} \right] \\
 \hline
 \text{Sym.} \\
 \hline
 \left[\begin{array}{cccccc}
 \frac{1}{6} \cdot M_e & 0 & 0 & 0 & 0 & 0 \\
 0 & \left(\frac{9}{70} - \frac{6}{5} \cdot \frac{r_g}{L_e^2} \right) \cdot M_e & 0 & 0 & 0 & - \left(\frac{13L_e}{420} - \frac{L_e}{10} \cdot \frac{r_g}{L_e^2} \right) \cdot M_e \\
 0 & 0 & \left(\frac{9}{70} - \frac{6}{5} \cdot \frac{r_g}{L_e^2} \right) \cdot M_e & 0 & \left(\frac{13L_e}{420} - \frac{L_e}{10} \cdot \frac{r_g}{L_e^2} \right) \cdot M_e & 0 \\
 0 & 0 & 0 & \frac{I_p}{6 \cdot A} \cdot M_e & 0 & 0 \\
 0 & 0 & - \left(\frac{13L_e}{420} - \frac{L_e}{10} \cdot \frac{r_g}{L_e^2} \right) \cdot M_e & 0 & \left(\frac{L_e^2}{140} + \frac{L_e^2}{30} \cdot \frac{r_g}{L_e^2} \right) \cdot M_e & 0 \\
 0 & \left(\frac{13L_e}{420} - \frac{L_e}{10} \cdot \frac{r_g}{L_e^2} \right) \cdot M_e & 0 & 0 & 0 & \left(\frac{L_e^2}{140} + \frac{L_e^2}{30} \cdot \frac{r_g}{L_e^2} \right) \cdot M_e
 \end{array} \right] \\
 \hline
 \left[\begin{array}{cccccc}
 \frac{1}{3} \cdot M_e & 0 & 0 & 0 & 0 & 0 \\
 0 & \left(\frac{13}{35} + \frac{6}{5} \cdot \frac{r_g}{L_e^2} \right) \cdot M_e & 0 & 0 & 0 & - \left(\frac{11L_e}{210} + \frac{L_e}{10} \cdot \frac{r_g}{L_e^2} \right) \cdot M_e \\
 0 & 0 & \left(\frac{13}{35} + \frac{6}{5} \cdot \frac{r_g}{L_e^2} \right) \cdot M_e & 0 & \left(\frac{11L_e}{210} + \frac{L_e}{10} \cdot \frac{r_g}{L_e^2} \right) \cdot M_e & 0 \\
 0 & 0 & 0 & \frac{I_p}{3 \cdot A} \cdot M_e & 0 & 0 \\
 0 & 0 & 0 & 0 & \left(\frac{L_e^2}{105} + \frac{2 \cdot L_e^2}{15} \cdot \frac{r_g}{L_e^2} \right) \cdot M_e & 0 \\
 0 & 0 & 0 & 0 & 0 & \left(\frac{L_e^2}{105} + \frac{2 \cdot L_e^2}{15} \cdot \frac{r_g}{L_e^2} \right) \cdot M_e
 \end{array} \right]
 \end{array}
 \begin{array}{l}
 \left. \begin{array}{l}
 u_1 \\
 v_1 \\
 w_1 \\
 \theta_{x1} \\
 \theta_{y1} \\
 \theta_{z1}
 \end{array} \right\} \\
 \left. \begin{array}{l}
 u_2 \\
 v_2 \\
 w_2 \\
 \theta_{x2} \\
 \theta_{y2} \\
 \theta_{z2}
 \end{array} \right\}
 \end{array}$$

Figure C.10: The mass matrix for a 3D frame element. Note, M_e is the mass of the element defined as: $M_e = A \cdot L_e \cdot \rho$

The eigenfrequencies are determined from the undamped vibration

eigenvalue problem, [Rao, 2005, P. 478]:

$$\det |\mathbf{K} - \bar{\omega}^2 \cdot \mathbf{M}| = 0 \quad (\text{C.4.1})$$

where $\frac{\bar{\omega}}{2\pi}$ are the positive cyclic eigenfrequencies of the structure in Hz. These are often sorted in an ascending order and $\bar{\omega}$ contains the circular eigenfrequencies, $\frac{1}{\text{rad}}$. The resulting first five eigenfrequencies are compared in Table C.1

Eigenfrequency number	ANSYS result	MATLAB result	Difference, percentage
1	3.5	3.5	1%
2	4.2	4.2	0.5%
3	5.5	5.4	2%
4	11.4	10.3	10%
5	12.7	11.6	8%

Table C.1: A comparison of the first five eigenfrequencies, obtained by ANSYS and MATLAB, used to verify the global stiffness matrix. Note, percentage differences are calculated from non-rounded values.

As seen from Table C.1 the difference in all eigenfrequencies fall within a 10% range. The difference may be a result of a slightly different mass matrix used in the two programs. The ANSYS elements are based on Timoshenko beam theory, while the implemented element in MATLAB is a Bernoulli-Euler element. This has an influence on both the mass and the stiffness matrices since the shear deformation is included for the Timoshenko beam. Naturally, this will have an effect on the calculated eigenfrequencies, see equation (C.4.1). A comparison of the global mass and stiffness matrices between ANSYS and MATLAB reveals that the largest differences occurs in the mass matrix. However, this is not shown in the report. The differences in the mass matrices can be accepted, since they are only used to verify the global stiffness matrix through the eigenfrequency check above. Some smaller differences are present in the stiffness matrix as well. In order to examine if these are significant, the global displacements are compared in the following.

C.4.2 Global displacements

The global displacements are determined by the use of equation (4.2.2). By checking the global displacements both the global stiffness matrix and the transformation matrix may be verified. Furthermore, a check of the global displacements should reveal if the different beam theories, Timoshenko

(ANSYS) and Bernoulli-Euler (MATLAB), will cause a significant change in the nodal displacements of the model.

Again the house model presented in Figure C.9 is used for the verification. Since Nodes 1,4,7, and 10 are all locked the model has 42 DOFs. However, only displacements of Node2 and Node3 are used in the comparison, Table C.2.

DOF	ANSYS result	MATLAB result	Difference, percentage
u_2	$3.45 \cdot 10^{-2}$	$3.44 \cdot 10^{-2}$	0.4%
v_2	$4.91 \cdot 10^{-5}$	$4.91 \cdot 10^{-5}$	0.1%
w_2	$-1.55 \cdot 10^{-5}$	$-1.55 \cdot 10^{-5}$	0%
θ_{x2}	$-6.16 \cdot 10^{-5}$	$-6.06 \cdot 10^{-5}$	1.5%
θ_{y2}	$-1.06 \cdot 10^{-2}$	$-1.06 \cdot 10^{-2}$	0.2%
θ_{z2}	$-1.94 \cdot 10^{-2}$	$-1.93 \cdot 10^{-2}$	0.3%
u_3	$3.44 \cdot 10^{-2}$	$3.43 \cdot 10^{-2}$	0.4%
v_3	$-1.91 \cdot 10^{-4}$	$-1.91 \cdot 10^{-4}$	0.1%
w_3	$7.72 \cdot 10^{-5}$	$7.72 \cdot 10^{-5}$	0%
θ_{x3}	$-1.91 \cdot 10^{-3}$	$-1.90 \cdot 10^{-3}$	0.7%
θ_{y3}	$-6.29 \cdot 10^{-3}$	$-6.27 \cdot 10^{-3}$	0.3%
θ_{z3}	$-2.65 \cdot 10^{-2}$	$-2.64 \cdot 10^{-2}$	0.5%

Table C.2: Comparison between global displacement results from ANSYS and MATLAB of node 2 and 3. Percentage differences are determined from non-rounded values.

Similar results are obtained for the remaining free DOFs. Based on the percentage deviation listed in Table C.2, the global stiffness and the transformation matrices have been verified. Furthermore, the check hints that the different theories have a higher influence on the mass matrix than on the stiffness matrix, see percentage difference of Table C.1. To examine the different theories, the tip deflection of a cantilevered beam with constant length and changing diameter is examined using ANSYS and MATLAB. The percentage difference between the obtained results may be seen in Figure C.11.

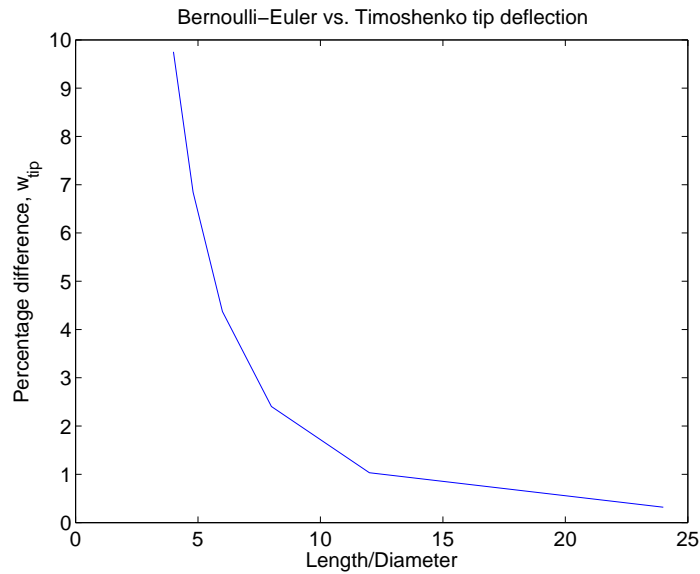


Figure C.11: The percentage difference between the tip deflection for a cantilevered beam, determined using ANSYS and MATLAB, as function of the slenderness ratio.

As seen from Figure C.11 the percentage difference between the two theories is lowered as the beam becomes more slender as expected. It is seen that the general rule of thumbs for using the Bernoulli-Euler theory, a slenderness ratio of 1/10, will result in an approximate deviation of 1 – 2%. The final result comparison will aim at validating the found stress components.

C.4.3 Stress results

Initially, a comparison between the normal stresses from the two different analyses is made followed by a comparison of the shear stresses. The stress values from different cross sectional sample points are compared between ANSYS and MATLAB. For the shear stresses a comparison to an analytical results is made as well.

Normal stresses

The normal stresses are compared for eight cross sectional sample points in each end of the element, seen in Figure C.12. The cross sectional normal stresses obtained in node two element four of the house, see Figure C.9 are compared in Table C.3.

Element	Element 4							
Node	Node 2							
α [deg.]	0	45	90	135	180	225	270	315
MATLAB result [MPa]	0.867	-252.1	-356.2	-250.4	3.3	256.2	360.3	254.5
ANSYS result [MPa]	0.875	-252.4	-356.7	-250.7	3.3	256.6	360.8	254.9
Difference, %	0.9	0.1	0.1	0.1	0.2	0.2	0.1	0.2

Table C.3: Normal stresses in eight cross sectional sampling points with $\alpha_{initial} = 0$. Note, percentage difference is calculated from non-rounded values.

As seen from Table C.3 the MATLAB FE program is capable of calculating the normal stress in the cross sectional sampling points with only a small difference to the commercial software ANSYS. Next, the shear stresses are examined.

Shear stresses

Comparing the shear stresses found by the MATLAB FE program directly with results obtained using ANSYS is difficult due to the different post processing used to calculate the shear stress values. Thus, a simple prismatic cantilevered beam model is used to verify the shear stresses. The cantilever beam has a length of 0.6 m. The beam consists of five elements with a diameter of 0.05 m and a thickness of 0.01 m. A vertical force of -1 N is applied at the end. The results of the ANSYS and the MATLAB analysis are compared in Table C.4.

Shear stress component	τ_{xy}	τ_{xz}
ANSYS result [Pa]	-1532.4	0
MATLAB result [Pa]	-1529.1	0
Difference, percentage	0.2%	-

Table C.4: Comparison between shear stress obtained from an ANSYS and a MATLAB analysis of a simple prismatic cantilever beam.

In both cases the shear stresses are constant along the length of the beam as expected. The ANSYS result has been obtained by averaging the values of cross sectional nodes 22, 24, 25, and 27, see Figure C.12, since these lie on an axis perpendicular to the direction of the applied force. In Figure C.12 the force is applied in the negative y' -direction.

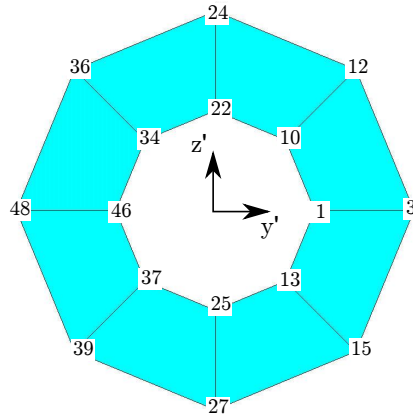


Figure C.12: The cross sectional nodes of the ANSYS beam element.

A difference of 0.21% was found between the shear stress from the ANSYS and the MATLAB analysis. Thus, the MATLAB FE program is capable of calculating the shear stresses of the model within an acceptable range of a commercial available software. Note, the result obtained using ANSYS is highly affected by the number of circumferential elements used in the cross section. The ANSYS result shown in Table C.4 is obtained for 64 circumferential elements, but averaged along to section nodes 22, 24, 25, and 27 as explained above. The use of just eight circumferential elements yields a shear stress result of -1634.6 Pa

Only a simple example between MATLAB and ANSYS was suitable for the comparison between the shear stresses. An example with a known analytical solution will be used to check that the FE program calculates the shear stresses properly. Four cross sectional sample points will be used. For the special case of a full half circle, $\beta = \frac{\pi}{2}$ an analytical solution, yielding the maximum shear stress, is available. The analytical solution for the full half circle is, [Goodno and Gere, 2009, P. 398]:

$$\tau_{max} = \frac{4V}{3A} \left(\frac{r_2^2 + r_2 r_1 + r_1^2}{r_2^2 + r_1^2} \right) \quad (\text{C.4.2})$$

The shear stresses in the four cross sectional sample points of node two in element four of the small house model are examined. Since torsion is present in the given element, this is taken into account as well by the use of equation (C.3.8). The shear stresses determined by MATLAB using equation (4.3.2), should be equal to the maximum shear values of the cross section in the four

sample points when $\alpha_{Initial} = 0$. A comparison of the analytical and the MATLAB shear stresses can be seen in Table C.5.

Element	Element 4			
Node	Node 2			
α [deg.]	0	90	180	270
MATLAB [MPa]	19.4	-30.4	-41.3	30.3
Analytical [MPa]	19.1	-30.4	-41.6	30.3
Difference, %	1.5	0	0.7	0

Table C.5: Comparison of MATLAB and analytical shear stress results in four cross sectional sample points with $\alpha_{Initial} = 0$ of the small house model. Percentage differences calculated from non-rounded values.

As seen from Table C.5 the shear stress distribution calculated in MATLAB is able to represent the maximum values in the cross sectional sample points for the case, where the analytical solution is available.

This concludes the MATLAB FE program verification. Through this verification, it was shown that the MATLAB code is capable of determining the eigenfrequencies of the structure being analyzed, the global displacement vector can be established, and the normal and shear stresses in each cross sectional sample point can be obtained.

Appendix D

Modeling Limitations

The purpose of this appendix is to determine the domain where the model is feasible. The jacket structure is designed such that the primary load condition is tension and compression in the frame elements. However, bending and shear may still be present and have an effect on the structure. In order to examine the effect from bending and shear, a cantilevered prismatic beam benchmark example, shown on Figure D.1 is set up. The situation should simulate one of the frame elements in the jacket model subjected to a shear/bending force, with fixed/free BCs. The example is a worst case scenario since bending and shear force are more severe in this example than in the frame elements in the jacket model.

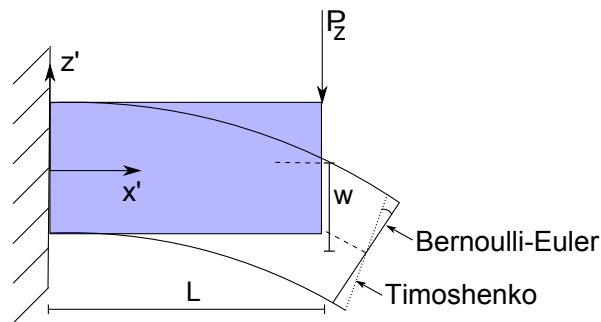


Figure D.1: Sketch of the benchmark example of a stubby cantilevered beam. The deformed shape is shown for both Timoshenko and Bernoulli-Euler beam theory.

The Bernoulli-Euler formulation of the frame elements does not include the effect of shear deformation. For short stubby beams the contribution from the shear deformation cannot be neglected. The Timoshenko theory accounts for

the shear contribution as explained in [Dym and Shames, 1991, P. 197]. The classical rules of thumb can be stated by the following list:

1. The Bernoulli-Euler beam theory will give acceptable results if the beam length is $L > 10 \cdot d$. Otherwise the Timoshenko theory will yield more accurate results.
2. The Bernoulli-Euler solution converges to the Timoshenko when the beam becomes more slender.

The tip deflection for the analytic Bernoulli-Euler beam can be stated as:

$$w_{cBE} = \frac{-P_z L^3}{3EI_y} \quad (\text{D.0.1})$$

while the tip deflection according to the analytic Timoshenko beam theory can be written as:

$$w_{cTimoshenko} = \frac{-P_z L}{\kappa GA} - \frac{P_z L^3}{3EI_y} \quad (\text{D.0.2})$$

It has been checked that the tip deflection obtained by the analytic Bernoulli-Euler solution seen in equation (D.0.1) is equal to the tip deflection found from the FE program as expected. It is seen from equation (D.0.1) and (D.0.2) that the only difference is the shear term in (D.0.2). Here κ is the shear correction factor, which for a hollow cylinder is given as:

$$\begin{aligned} \kappa &= \frac{6(1 + \nu)(1 + \Phi)^2}{(7 + 6\nu)(1 + \Phi)^2 + (20 + 12\nu)\Phi^2} \\ \Phi &= \frac{(d - 2t)/2}{d/2} \end{aligned} \quad (\text{D.0.3})$$

The guidelines stated above are examined further by the use of the benchmark example of Figure D.1.

D.1 Comparison of Results

The tip deflection for the analytic Timoshenko beam and the FE program, based on Bernoulli-Euler assumptions, is compared. First, the two parameters diameter and length are varied for a fixed thickness of 0.02 m. The relative deviation between the found tip displacements is plotted as a function of these two parameters, see Figure D.2a. From Figure D.2a it can be seen that a factor

of ten between the diameter and the length, results in a deviation of less than 2%, which is considered to be acceptable.

Next, the influence of a thickness variation on the tip displacement is checked. The diameter and the thickness are varied for a fixed length of 10 m and the relative error between the found displacements is plotted as a function of these, see Figure D.2b. The figure shows, that the variation of the thickness has little if any influence on the relative error between the calculated displacements. Again, it is seen that the relative error increases above two percent as the diameter exceeds 1 m, thus violating the 1/10 relationship with the length set by the Bernoulli-Euler theory.

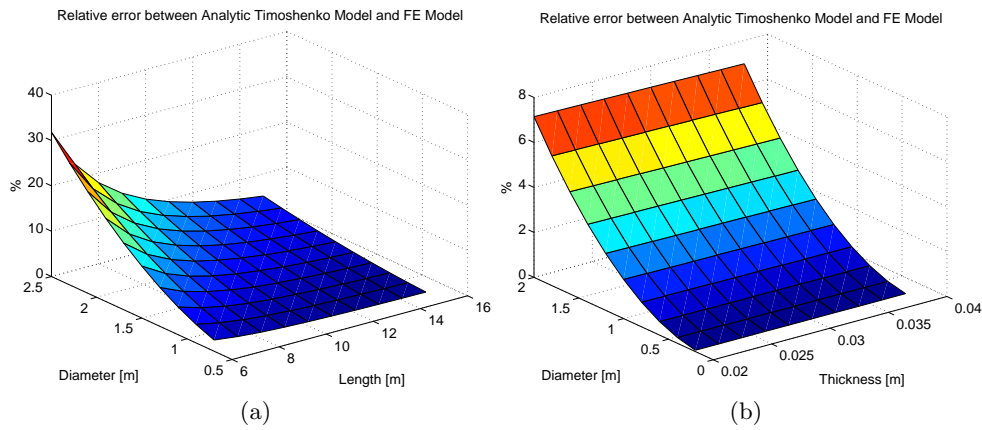


Figure D.2: Relative deviation of tip displacements between the analytic Timoshenko Model and the FE model for a study of: (a) Diameter and length with a fixed thickness and 0.002 m and (b) diameter and thickness with fixed length of 10 m.

Appendix E

Fatigue

This appendix includes a description of the rainflow method and a benchmark example to verify that the implementation of the damage estimation has been made successfully.

E.1 Benchmark Example of Damage Estimation

In order to test the rainflow count, the sorting algorithm, and the calculation of the accumulated damage, a benchmark example from [Stephens et al., 2001, P. 293] with known damage quantity, is used. The stress history of the example can be seen in Figure E.1.

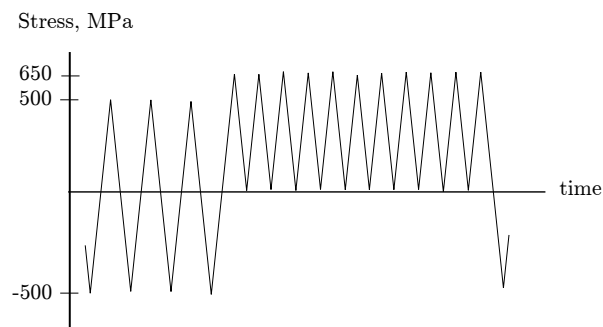


Figure E.1: The stress history of the benchmark example used for the verification of the fatigue procedure, [Stephens et al., 2001, Figure 9.16].

E.1.1 Rainflow Counting

First a rainflow count of the stress history of Figure 5.3 is conducted. The result from the rainflow count can be condensed to the results seen in Table E.1.

Stress amplitude [MPa]	500	325	575
Stress mean [MPa]	0	325	75
No. cycles	3	10	1

Table E.1: Rainflow count result on the stress history seen in Figure 5.3.

A quick manual rainflow count and a comparison to the results obtained in [Stephens et al., 2001, P. 292] reveals that the rainflow count is correct. A larger stress history, containing approximately 50 stress peaks, with known rainflow counting results is tested as well and again the rainflow script proved to give accurate results. This is however not shown in the report. Next, the sorting algorithm is tested.

E.1.2 Sorting Algorithm

The purpose of the sorting algorithm is to divide the raw output data from the rainflow counting script into a number of intervals. The number of intervals may be specified by the user, and for this example $N_{Amp} = 5$ and $N_{Mean} = 5$ are chosen. This will give the amplitude intervals: $0 < A_0 \leq 115$, $115 < A_0 \leq 230$, $230 < A_0 \leq 345$, $345 < A_0 \leq 460$, and $460 < A_0 \leq 575$. The obtained mean intervals are: $0 < A_0 \leq 65$, $65 < A_0 \leq 130$, $130 < A_0 \leq 195$, $195 < A_0 \leq 260$, and $260 < A_0 \leq 325$. An example output from the sorting algorithm is shown in Table E.2, where the maximum method introduced in section 5.3 is used.

Stress amplitude [MPa]	575	345	575
Stress mean [MPa]	65	325	130
No. cycles	3	10	1

Table E.2: Results of the sorting algorithm. Only intervals with non-zero cycle numbers are shown.

A comparison between Tables E.1 and E.2 reveals that the sorting routine

has an influence on the obtained results. Stress cycles with an actual amplitude of 325 MPa, column three of Table E.1, will now appear to have an amplitude on 345 MPa. Similar observations may be made for mean results, where a mean value of 75 MPa will change to 130 MPa as a result of the sorting intervals. Thus, the number of intervals for the sorting algorithm should be chosen carefully in order to reduce the influence from the sorting on the obtained accumulated damage. Only an output table using the maximum approach is shown, but the same argument goes for all three approaches used to determine the amplitude value in the sorted rainflow table. See section 5.6.1 for an in-depth discussion.

E.1.3 Damage Calculation

For the benchmark example the effect of the mean stress is taken into account using the procedure described in section 5.4. According to [Stephens et al., 2001, P. 295] the actual accumulated damage is 0.0139 for the examined benchmark example. The accumulated damage calculated in the MATLAB FE program using the maximum damage approach is 0.0338 as a result of the overestimation of the stress values due to the sorting algorithm. By manually overwriting the results from the sorting algorithm to the exact stress amplitude and mean values yields an accumulated damage on 0.0139 as expected. This shows that the accumulated damage may be determined by the use of the MATLAB FE program.

Appendix F

DSA Methods

This chapter contains the description of three methods used for DSA. This includes OFD, DDM, and AM. Parenthesis in this section is used to emphasize the dependency among the variables. When equations from this appendix are used in the report they will be written in compact form without dependencies.

F.1 Overall Finite Difference Method

One approach for the DSA is to use a FD approximation, which is based on a Taylor series. The simplest method to obtain the derivative is the forward FD approach, which is a first order approximation to the derivative and it is written as:

$$\frac{dg_k}{dx_j} = \frac{g_k(\bar{U}(\bar{x} + \Delta x_j), \bar{x} + \Delta x_j) - g_k(\bar{U}(\bar{x}), \bar{x})}{\Delta x_j} + o(\Delta x_j) \quad (\text{F.1.1})$$

The central FD approximation needs another evaluation of the function for each approximation to the gradient. The central FD approach to approximate the gradient is a second order accurate method, and it can be written as (F.1.2).

$$\frac{dg_k}{dx_j} = \frac{g_k(\bar{U}(\bar{x} + \Delta x_j), \bar{x} + \Delta x_j) - g_k(\bar{U}(\bar{x} - \Delta x_j), \bar{x} - \Delta x_j)}{2\Delta x_j} + o^2(\Delta x_j) \quad (\text{F.1.2})$$

The two major contributors to errors are truncation- and condition errors. The truncation error is a result of the neglected terms in the Taylor series. This error can be reduced by using a small perturbation Δx or by using

higher order FD schemes. As a result, the central FD has a smaller truncation error than the forward FD. The condition error is the difference between the numerical evaluation of the function and its exact value [Haftka and Gürdal, 1992]. Condition errors are typically due to computational rounding. Thus, selecting a small perturbation lowers the truncation error, but increases the condition error.

OFD approximations are in general computationally inefficient, but popular since they are easy to implement. The need for an extra analysis for each perturbation of the design variables makes the OFD approximations computationally heavy. One implication is also to overcome the challenge of determining a suitable perturbation. Furthermore, the accuracy of the method can also be difficult to establish.

F.2 Direct Differentiation Method

This section is based on Michaleris and Tortorelli [1994]. The equilibrium equation is defined by equation (F.2.1).

$$\mathbf{K}(\bar{x})\bar{U}(\bar{x}) = \bar{P}(\bar{x}) \quad (\text{F.2.1})$$

$\mathbf{K}(\bar{x})$ is an explicit function of \bar{x} . The load vector \bar{P} is independent of the design variables for all examples used in this report. $\bar{U}(\bar{x})$ is an implicit function of design \bar{x} since equation (F.2.1) is a linear system of equations, which needs to be solved to determine $\bar{U}(\bar{x})$. $\bar{U}(\bar{x})$ and \bar{P} have length equal to the number of free DOFs in the FE model and $\mathbf{K}(\bar{x})$ is a square matrix of equal dimensions.

When using the FE method the system response $\bar{U}(\bar{x})$ must be determined first since it is needed to evaluate the constraint function, which will be defined through:

$$g_k(\bar{x}) = g_k(\bar{U}(\bar{x}), \bar{x}) \quad (\text{F.2.2})$$

To obtain the sensitivity of the constraint function $g_k(\bar{U}(\bar{x}), \bar{x})$ the chain rule can be used:

$$\frac{dg_k}{dx_j}(\bar{x}) = \frac{\partial g_k}{\partial x_j}(\bar{U}(\bar{x}), \bar{x}) + \frac{\partial g_k^T}{\partial \bar{U}}(\bar{U}(\bar{x}), \bar{x}) \frac{d\bar{U}}{dx_j}(\bar{x}) \quad (\text{F.2.3})$$

The challenging part of determining $\frac{dg_k}{dx_j}(\bar{x})$ in equation (F.2.3) is to evaluate the the term $\frac{d\bar{U}}{dx_j}(\bar{x})$. In order to find the last term in (F.2.3) the

equilibrium equation must be differentiated and rearranged as:

$$\begin{aligned} \frac{\partial \mathbf{K}}{\partial x_j}(\bar{x})\bar{U}(\bar{x}) + \mathbf{K}(\bar{x})\frac{d\bar{U}}{dx_j}(\bar{x}) &= \frac{\partial \bar{P}}{\partial x_j} \downarrow \\ \mathbf{K}(\bar{x})\frac{d\bar{U}}{dx_j}(\bar{x}) &= \left(\frac{\partial \bar{P}}{\partial x_j} - \frac{\partial \mathbf{K}}{\partial x_j}(\bar{x})\bar{U}(\bar{x}) \right) \end{aligned} \quad (\text{F.2.4})$$

The derivative of the global stiffness matrix w.r.t. design variables may be assembled from the derivative of the element stiffness matrix, similar to the assembly of the global stiffness matrix from several element stiffness matrices. Often this procedure is quite fast, since a given design variable usually only affects a few elements in the entire model. For the present example the applied loads are not dependent on the design variables. Hence the derivative of the global displacements w.r.t. design variables may be established by:

$$\mathbf{K}(\bar{x})\frac{d\bar{U}}{dx_j}(\bar{x}) = \left(-\frac{\partial \mathbf{K}}{\partial x_j}(\bar{x})\bar{U}(\bar{x}) \right) \quad (\text{F.2.5})$$

Equation (F.2.5) can be solved for $\frac{d\bar{U}}{dx_j}(\bar{x})$ by solving a linear system of equations. Thus, the sensitivity of the constraint functions w.r.t. the design variables may now be determined by the DDM presented in equation (F.2.3).

F.3 Adjoint Method

In the adjoint method the derivative $\frac{d\bar{U}}{dx_j}(\bar{x})$ is eliminated by introducing a Lagrange multiplier:

$$\hat{g}_k(\bar{x}) = g_k(\bar{U}(\bar{x}), \bar{x}) - \bar{\lambda}(\bar{x})^T \bar{R}(\bar{U}(\bar{x}), \bar{x}) \quad (\text{F.3.1})$$

$\bar{\lambda}(\bar{x})$ acts as a Lagrange multiplier vector and may be chosen arbitrary. The residual is given by $\bar{R} = \bar{P} - \mathbf{K}\bar{U} = \bar{0}$. Differentiation of equation (F.3.1) and rearranging yields:

$$\begin{aligned} \frac{d\hat{g}_k}{dx_j}(\bar{x}) &= \frac{\partial g_k}{\partial x_j}(\bar{U}(\bar{x}), \bar{x}) - \bar{\lambda}(\bar{x})^T \cdot \left(\frac{\partial \mathbf{K}}{\partial x_j}(\bar{x})\bar{U}(\bar{x}) - \frac{\partial \bar{P}}{\partial x_j}(\bar{x}) \right) + \\ &\quad \frac{d\bar{U}}{dx_j}(\bar{x}) \left(\frac{\partial g_k}{\partial \bar{U}}(\bar{U}(\bar{x}), \bar{x}) - \mathbf{K}^T(\bar{x})\bar{\lambda}(\bar{x}) \right) \end{aligned} \quad (\text{F.3.2})$$

The Lagrange multiplier must be determined to eliminate the $\frac{d\bar{U}}{dx_j}(\bar{x})$.

Thus, the following adjoint problem must be solved in order to determine $\bar{\lambda}(\bar{x})$ term.

$$\mathbf{K}^T(\bar{x})\bar{\lambda}(\bar{x}) = \frac{\partial g_k}{\partial \bar{U}}(\bar{U}(\bar{x}), \bar{x}) \quad (\text{F.3.3})$$

Once $\bar{\lambda}(\bar{x})$ is determined, equation (F.3.2) will be reduced to:

$$\frac{d\hat{g}_k}{dx_j}(\bar{x}) = \frac{\partial g_k}{\partial x_j}(\bar{U}(\bar{x}), x) - \bar{\lambda}(\bar{x}) \cdot \left(\frac{\partial \mathbf{K}}{\partial x_j}(\bar{x})\bar{U}(\bar{x}) - \frac{\partial \bar{P}}{\partial x_j}(\bar{x}) \right) \quad (\text{F.3.4})$$

Again the last term in equation (F.3.4) is zero since the load is constant with respect to \bar{x} . It should be noted, that a more comprehensive presentation of the DDM and AM, and examples of these can be read in details in Michaleris and Tortorelli [1994].

Appendix G

Normal Stress Sensitivity

This section contains the derivatives of the normal stresses. In the first subsection it is described how the DSA is made according to the design variables, while in the second subsection is described how the derivatives of normal stresses w.r.t. global displacements are performed.

G.0.1 Normal Stress Derivatives w.r.t Design Variables

The normal stress is obtained as a combination of two moments and one normal force as shown by (4.3.1). This can also be written as:

$$\sigma(d, t) = \frac{P}{A} - \frac{M_y d \sin(\alpha + \alpha_{Initial})}{2I_y} - \frac{M_z d \cos(\alpha + \alpha_{Initial})}{2I_z} \quad (G.0.1)$$

The following variables in equation (G.0.1) depends on the design variables, \bar{x} : M_y , M_z , I_y , I_z , d , and A . In the following $\sigma(d, t)$ will be written as σ for simplicity. First it will be derived with regards to the variables mentioned:

$$\frac{\partial \sigma}{\partial x} = \frac{\partial \sigma}{\partial M_y} \frac{\partial M_y}{\partial x} + \frac{\partial \sigma}{\partial M_z} \frac{\partial M_z}{\partial x} + \frac{\partial \sigma}{\partial d} \frac{\partial d}{\partial x} + \frac{\partial \sigma}{\partial I_y} \frac{\partial I_y}{\partial x} + \frac{\partial \sigma}{\partial I_z} \frac{\partial I_z}{\partial x} + \frac{\partial \sigma}{\partial P} \frac{\partial P}{\partial x} + \frac{\partial \sigma}{\partial A} \frac{\partial A}{\partial x} \quad (G.0.2)$$

The derivatives of the stress with respect to the dependent variables are

obtained as:

$$\frac{\partial \sigma}{\partial M_y} = -\frac{d \sin(\alpha + \alpha_{Initial})}{2I_y} \quad (G.0.3)$$

$$\frac{\partial \sigma}{\partial M_z} = -\frac{d \cos(\alpha + \alpha_{Initial})}{2I_z} \quad (G.0.4)$$

$$\frac{\partial \sigma}{\partial I_y} = \frac{M_y d \sin(\alpha + \alpha_{Initial})}{2I_y^2} \quad (G.0.5)$$

$$\frac{\partial \sigma}{\partial I_z} = \frac{M_z d \cos(\alpha + \alpha_{Initial})}{2I_z^2} \quad (G.0.6)$$

$$\frac{\partial \sigma}{\partial d} = -\frac{M_y \sin(\alpha + \alpha_{Initial})}{2I_y} - \frac{M_z \cos(\alpha + \alpha_{Initial})}{2I_z} \quad (G.0.7)$$

$$\frac{\partial \sigma}{\partial P} = \frac{1}{A} \quad (G.0.8)$$

$$\frac{\partial \sigma}{\partial A} = -\frac{P}{A^2} \quad (G.0.9)$$

The derivative $\frac{\partial A}{\partial x}$ can be written as:

$$\frac{\partial A}{\partial d} = \pi t \quad \frac{\partial A}{\partial t} = \pi(d - 2t) \quad (G.0.10)$$

The derivative $\frac{\partial P}{\partial x}$ is independent of the design variables.

The derivative $\frac{\partial I}{\partial x}$ in (G.0.13) is obtained by deriving:

$$I_y = I_z = \frac{\pi}{4} \left(\left(\frac{d}{2} \right)^4 - \left(\frac{d}{2} - t \right)^4 \right) \quad (G.0.11)$$

which can be written as:

$$\frac{\partial I_y}{\partial d} = \frac{\partial I_z}{\partial d} = \frac{\pi}{4} \left(\frac{1}{4} d^3 - 2 \left(\frac{1}{2} d - t \right)^3 \right) \quad (G.0.12)$$

$$\frac{\partial I_y}{\partial t} = \frac{\partial I_z}{\partial t} = \pi \left(\frac{1}{2} d - t \right)^3 \quad (G.0.13)$$

The derivative $\frac{\partial d}{\partial x}$ can be written as:

$$\frac{\partial d}{\partial d} = 1 \quad \frac{\partial d}{\partial t} = 0 \quad (G.0.14)$$

The derivative $\frac{\partial M}{\partial x}$ depends on the node number in the frame element. It can be written for node one as:

$$\frac{\partial M_{y1}}{\partial d} = E \frac{\partial I_y}{\partial d} \left(-\frac{6}{L^2} w'_1 + \frac{4}{L} \theta'_{y1} + \frac{6}{L^2} w'_2 + \frac{2}{L} \theta'_{y2} \right) \quad (\text{G.0.15})$$

$$\frac{\partial M_{y1}}{\partial t} = E \frac{\partial I_y}{\partial t} \left(-\frac{6}{L^2} w'_1 + \frac{4}{L} \theta'_{y1} + \frac{6}{L^2} w'_2 + \frac{2}{L} \theta'_{y2} \right) \quad (\text{G.0.16})$$

$$\frac{\partial M_{z1}}{\partial d} = E \frac{\partial I_y}{\partial d} \left(\frac{6}{L^2} v'_1 + \frac{4}{L} \theta'_{z1} - \frac{6}{L^2} v'_2 + \frac{2}{L} \theta'_{z2} \right) \quad (\text{G.0.17})$$

$$\frac{\partial M_{z1}}{\partial t} = E \frac{\partial I_y}{\partial t} \left(\frac{6}{L^2} v'_1 + \frac{4}{L} \theta'_{z1} - \frac{6}{L^2} v'_2 + \frac{2}{L} \theta'_{z2} \right) \quad (\text{G.0.18})$$

and for node two as:

$$\frac{\partial M_{y2}}{\partial d} = E \frac{\partial I_y}{\partial d} \left(-\frac{6}{L^2} w'_1 + \frac{2}{L} \theta'_{y1} + \frac{6}{L^2} w'_2 + \frac{4}{L} \theta'_{y2} \right) \quad (\text{G.0.19})$$

$$\frac{\partial M_{y2}}{\partial t} = E \frac{\partial I_y}{\partial t} \left(-\frac{6}{L^2} w'_1 + \frac{2}{L} \theta'_{y1} + \frac{6}{L^2} w'_2 + \frac{4}{L} \theta'_{y2} \right) \quad (\text{G.0.20})$$

$$\frac{\partial M_{z2}}{\partial d} = E \frac{\partial I_y}{\partial d} \left(\frac{6}{L^2} v'_1 + \frac{2}{L} \theta'_{z1} - \frac{6}{L^2} v'_2 + \frac{4}{L} \theta'_{z2} \right) \quad (\text{G.0.21})$$

$$\frac{\partial M_{z2}}{\partial t} = E \frac{\partial I_y}{\partial t} \left(\frac{6}{L^2} v'_1 + \frac{2}{L} \theta'_{z1} - \frac{6}{L^2} v'_2 + \frac{4}{L} \theta'_{z2} \right) \quad (\text{G.0.22})$$

G.0.2 Normal Stress Derivatives w.r.t. Displacements

The derivatives of (G.0.1) w.r.t. the displacements can be obtained as:

$$\frac{\partial \sigma}{\partial \bar{U}} = \frac{\partial \sigma}{\partial M_y} \frac{\partial M_y}{\partial \bar{U}} + \frac{\partial \sigma}{\partial M_z} \frac{\partial M_z}{\partial \bar{U}} + \frac{\partial \sigma}{\partial P} \frac{\partial P}{\partial \bar{U}} \quad (\text{G.0.23})$$

The displacement dependent variables in (G.0.1) includes: M_y , M_z , and P . The derivatives of the normal stress with respect to the dependent variables are obtained in (G.0.3) to (G.0.9). The derivatives w.r.t. the displacements

are obtained as:

$$\frac{\partial M_{y1}}{\partial \bar{U}'} = EI_y \frac{\partial}{\partial \bar{U}} \left(\frac{-6}{L^2} w'_1 + \frac{4}{L} \theta'_{y1} + \frac{6}{L^2} w'_2 + \frac{2}{L} \theta'_{y2} \right) \quad (\text{G.0.24})$$

$$\frac{\partial M_{y2}}{\partial \bar{U}'} = EI_y \frac{\partial}{\partial \bar{U}} \left(\frac{-6}{L^2} w'_1 + \frac{2}{L} \theta'_{y1} + \frac{6}{L^2} w'_2 + \frac{4}{L} \theta'_{y2} \right) \quad (\text{G.0.25})$$

$$\frac{\partial M_{z1}}{\partial \bar{U}'} = EI_z \frac{\partial}{\partial \bar{U}} \left(\frac{6}{L^2} v'_1 + \frac{4}{L} \theta'_{z1} + \frac{-6}{L^2} v'_2 + \frac{2}{L} \theta'_{z2} \right) \quad (\text{G.0.26})$$

$$\frac{\partial M_{z2}}{\partial \bar{U}'} = EI_z \frac{\partial}{\partial \bar{U}} \left(\frac{6}{L^2} v'_1 + \frac{2}{L} \theta'_{z1} + \frac{-6}{L^2} v'_2 + \frac{4}{L} \theta'_{z2} \right) \quad (\text{G.0.27})$$

$$\frac{\partial P}{\partial \bar{U}'} = EA \frac{\partial}{\partial \bar{U}} \left(\frac{-1}{L} u'_1 + \frac{1}{L} u'_2 \right) \quad (\text{G.0.28})$$

Thus, the entries in the local stiffness matrices defined in (C.0.10) and (C.0.11) have been used. The entries are only used when the corresponding DOF is active. All the necessary equations for the analytical DSA for the normal stresses have now been obtained.

Appendix H

Shear Stress Sensitivity

As seen in equation (4.3.2) both the shear force and the torsional moment add to the total shear stress in the cross sectional sample points. It was seen earlier that the shear stress stemming from the shear force may be determined by:

$$\begin{aligned}\tau_y &= \frac{V_y Q_y}{I_z \cdot 2t} \\ \tau_z &= \frac{V_z Q_z}{I_y \cdot 2t}\end{aligned}\tag{H.0.1}$$

The shear stress stemming from the torsional moment is found from:

$$\begin{aligned}\tau_{Ty} &= -\frac{Td}{2I_p} \cdot \sin(\alpha + \alpha_{Initial}) \\ \tau_{Tz} &= \frac{Td}{2I_p} \cdot \cos(\alpha + \alpha_{Initial})\end{aligned}\tag{H.0.2}$$

By superposition of equations (H.0.1) and (H.0.2), the total shear stress in the cross sectional sample points are determined:

$$\tau_{tot} = \tau_y + \tau_z + \tau_{Ty} + \tau_{Tz}\tag{H.0.3}$$

The torsional moment is given as:

$$T = GI_p \left(\frac{\theta_{x2}' - \theta_{x1}'}{L} \right)\tag{H.0.4}$$

The two shear forces V_y and V_z are given as:

$$\begin{aligned}V_y &= EI_z \left(\frac{12}{L^3} v_1' + \frac{6}{L^2} \theta_{z1}' - \frac{12}{L^3} v_2' + \frac{6}{L^2} \theta_{z2}' \right) \\ V_z &= EI_y \left(\frac{12}{L^3} w_1' - \frac{6}{L^2} \theta_{y1}' - \frac{12}{L^3} w_2' - \frac{6}{L^2} \theta_{y2}' \right)\end{aligned}\tag{H.0.5}$$

The first- and second area moment of inertia are determined from:

$$\begin{aligned}
I_y = I_z &= \frac{\pi}{64} \left(d^4 - (d - 2 \cdot t)^4 \right) \\
Q_y &= 2t \sin(\beta) \cdot \left(\frac{d}{2} - \frac{t}{2} \right)^2 \\
Q_z &= 2t \sin\left(\beta + \frac{\pi}{2}\right) \cdot \left(\frac{d}{2} - \frac{t}{2} \right)^2
\end{aligned} \tag{H.0.6}$$

and the polar moment of inertia for a circular hollow cross section is given as:

$$I_p = \frac{\pi}{32} \left(d^4 - (d - 2t)^4 \right) \tag{H.0.7}$$

In order to determine the sensitivity of the damage constraints the partial derivative of the shear stress w.r.t. both the design variables and the global displacements must be determined. First, the partial derivative of the shear stress w.r.t. the design variables x_j are determined.

$$\begin{aligned}
\frac{\partial \tau_{tot}}{\partial x_j} &= \frac{\partial \tau_{tot}}{\partial V_y} \frac{\partial V_y}{\partial x_j} + \frac{\partial \tau_{tot}}{\partial Q_y} \frac{\partial Q_y}{\partial x_j} + \frac{\partial \tau_{tot}}{\partial I_z} \frac{\partial I_z}{\partial x_j} + \frac{\partial \tau_{tot}}{\partial t} \frac{\partial t}{\partial x_j} + \\
&\quad \frac{\partial \tau_{tot}}{\partial V_z} \frac{\partial V_z}{\partial x_j} + \frac{\partial \tau_{tot}}{\partial Q_z} \frac{\partial Q_z}{\partial x_j} + \frac{\partial \tau_{tot}}{\partial I_y} \frac{\partial I_y}{\partial x_j} + \frac{\partial \tau_{tot}}{\partial T} \frac{\partial T}{\partial x_j} + \\
&\quad \frac{\partial \tau_{tot}}{\partial d} \frac{\partial d}{\partial x_j} + \frac{\partial \tau_{tot}}{\partial I_p} \frac{\partial I_p}{\partial x_j}
\end{aligned} \tag{H.0.8}$$

The partial derivatives of the first-, second and polar moments of inertia w.r.t. the design variables d and t are determined next. The sensitivity of the first area moment of inertia is given as:

$$\begin{aligned}
\frac{\partial Q_y}{\partial d} &= 2t \sin(\beta) \cdot \left(\frac{d}{2} - \frac{t}{2} \right) \quad ; \quad \frac{\partial Q_z}{\partial d} = 2t \sin\left(\beta + \frac{\pi}{2}\right) \cdot \left(\frac{d}{2} - \frac{t}{2} \right) \\
\frac{\partial Q_y}{\partial t} &= 2 \sin(\beta) \cdot \left(\frac{d}{2} - \frac{t}{2} \right)^2 - 2t \sin(\beta) \cdot \left(\frac{d}{2} - \frac{t}{2} \right) \\
\frac{\partial Q_z}{\partial t} &= 2 \sin\left(\beta + \frac{\pi}{2}\right) \cdot \left(\frac{d}{2} - \frac{t}{2} \right)^2 - 2t \sin\left(\beta + \frac{\pi}{2}\right) \cdot \left(\frac{d}{2} - \frac{t}{2} \right)
\end{aligned} \tag{H.0.9}$$

The sensitivities of the second area moments of inertia are given as:

$$\begin{aligned}
\frac{\partial I_y}{\partial d} = \frac{\partial I_z}{\partial d} &= \frac{\pi}{64} \left(4d^3 - 4(d - 2t)^3 \right) \\
\frac{\partial I_y}{\partial t} = \frac{\partial I_z}{\partial t} &= \frac{\pi}{64} \left(8(d - 2t)^3 \right) = \frac{\pi}{8} (d - 2t)^3
\end{aligned} \tag{H.0.10}$$

The sensitivities of the polar area moment of inertia are found from:

$$\begin{aligned}\frac{\partial I_p}{\partial d} &= \frac{\pi}{32} \left(4d^3 - 4(d-2t)^3 \right) \\ \frac{\partial I_p}{\partial t} &= \frac{\pi}{32} \left(8(d-2t)^3 \right) = \frac{\pi}{4} (d-2t)^3\end{aligned}\quad (\text{H.0.11})$$

Next, the sensitivities of the applied shear forces and the torsional moment are determined. The sensitivity of the torsional moment is given as:

$$\frac{\partial T}{\partial x_j} = G \left(\frac{\theta_{x_2}' - \theta_{x_1}'}{L} \right) \cdot \frac{\partial I_p}{\partial x_j} \quad (\text{H.0.12})$$

The derivatives of the two shear forces w.r.t. the diameter and the thickness are found to be:

$$\begin{aligned}\frac{\partial V_y}{\partial x_j} &= E \left(\frac{12}{L^3} v_1' + \frac{6}{L^2} \theta_{z_1}' - \frac{12}{L^3} v_2' + \frac{6}{L^2} \theta_{z_2}' \right) \cdot \frac{\partial I_z}{\partial x_j} \\ \frac{\partial V_z}{\partial x_j} &= E \left(\frac{12}{L^3} w_1' - \frac{6}{L^2} \theta_{y_1}' - \frac{12}{L^3} w_2' - \frac{6}{L^2} \theta_{y_2}' \right) \cdot \frac{\partial I_y}{\partial x_j}\end{aligned}\quad (\text{H.0.13})$$

Naturally, the derivatives of the diameter and thickness w.r.t. the design variables are:

$$\begin{aligned}\frac{\partial d}{\partial d} &= 1 & \frac{\partial d}{\partial t} &= 0 \\ \frac{\partial t}{\partial d} &= 0 & \frac{\partial t}{\partial t} &= 1\end{aligned}\quad (\text{H.0.14})$$

Next, the derivatives of the shear stress w.r.t. to parameters dependent on the design variables are determined. The derivative of the shear stress w.r.t. the shear forces and the torsional moment are given as:

$$\begin{aligned}\frac{\partial \tau_{tot}}{\partial V_y} &= \frac{Q_y}{I_z \cdot 2t} & ; & & \frac{\partial \tau_{tot}}{\partial V_z} &= \frac{Q_z}{I_y \cdot 2t} \\ \frac{\partial \tau_{tot}}{\partial T} &= -\frac{d}{2I_p} \cdot \sin(\alpha + \alpha_{Initial}) + \frac{d}{2I_p} \cdot \cos(\alpha + \alpha_{Initial})\end{aligned}\quad (\text{H.0.15})$$

The partial derivatives of the shear stresses w.r.t. the various area moments of inertia are given as:

$$\begin{aligned}\frac{\partial \tau_{tot}}{\partial Q_y} &= \frac{V_y}{I_z \cdot 2t} & \frac{\partial \tau_{tot}}{\partial I_z} &= -\frac{V_y Q_y}{I_z^2 \cdot 2t} \\ \frac{\partial \tau_{tot}}{\partial Q_z} &= \frac{V_z}{I_y \cdot 2t} & \frac{\partial \tau_{tot}}{\partial I_y} &= -\frac{V_z Q_z}{I_y^2 \cdot 2t} \\ \frac{\partial \tau_{tot}}{\partial I_p} &= \frac{Td}{2I_p^2} \sin(\alpha + \alpha_{Initial}) - \frac{Td}{2I_p^2} \cos(\alpha + \alpha_{Initial})\end{aligned}\quad (\text{H.0.16})$$

Next, the sensitivity of the shear stress w.r.t. the diameter and thickness is found:

$$\begin{aligned}\frac{\partial \tau_{tot}}{\partial d} &= -\frac{T}{2I_p} \sin(\alpha + \alpha_{Initial}) + \frac{T}{2I_p} \cos(\alpha + \alpha_{Initial}) \\ \frac{\partial \tau_{tot}}{\partial t} &= -\frac{V_y Q_y}{I_z \cdot 2t^2} - \frac{V_z Q_z}{I_y \cdot 2t^2}\end{aligned}\quad (\text{H.0.17})$$

At this point, all derivatives to carry out the analytical sensitivity calculation using equation (H.0.8) have been found. Next, the derivative of the shear stress w.r.t. the global displacement vector is examined.

$$\frac{\partial \tau_{tot}}{\partial \bar{U}} = \frac{\partial \tau_{tot}}{\partial V_y} \frac{\partial V_y}{\partial \bar{U}} + \frac{\partial \tau_{tot}}{\partial V_z} \frac{\partial V_z}{\partial \bar{U}} + \frac{\partial \tau_{tot}}{\partial T} \frac{\partial T}{\partial \bar{U}} \quad (\text{H.0.18})$$

The derivatives of the shear stress w.r.t. the two shear forces and the torsional moment were determined in equation (H.0.15). Thus, only the derivatives of the shear forces and the torsional moment w.r.t. the global displacements must be determined in order to calculate the shear stress sensitivity from equation (H.0.18). These are given as:

$$\begin{aligned}\frac{\partial V_y}{\partial \bar{U}} &= EI_z \cdot \frac{\partial}{\partial \bar{U}} \left(\frac{12}{L^3} v'_1 + \frac{6}{L^2} \theta'_{z1} - \frac{12}{L^3} v'_2 + \frac{6}{L^2} \theta'_{z2} \right) \\ \frac{\partial V_z}{\partial \bar{U}} &= EI_y \cdot \frac{\partial}{\partial \bar{U}} \left(\frac{12}{L^3} w'_1 - \frac{6}{L^2} \theta'_{y1} - \frac{12}{L^3} w'_2 - \frac{6}{L^2} \theta'_{y2} \right) \\ \frac{\partial T}{\partial \bar{U}} &= GI_p \cdot \frac{\partial}{\partial \bar{U}} \left(\frac{\theta'_{x2} - \theta'_{x1}}{L} \right)\end{aligned}\quad (\text{H.0.19})$$

Thus, the shear stress sensitivities w.r.t. the global displacements may be determined from equation (H.0.18). The terms in (H.0.19) are only used when the corresponding DOF is active. This concludes the sensitivity analysis of the shear stresses.

Appendix I

Calculation Time

The purpose of this section is to clarify where in the program the calculation time is spent, and to make suggestions to where reductions in the calculation time may be found. First the calculation time of one iteration of the optimization of the jacket structure will be examined. Next, the calculation time of the DSA is examined. It should be noted, that no extraordinary attempts of writing the code efficiently by the use of vectorization or compiling the code to .mex files are made.

I.0.3 Calculation Time in Optimization

One iteration of the optimization algorithm is performed for the jacket model where the gradients are computed with the forward FD, and it is investigated where in the program the computational time is spent. It should be noted that the calculation time is dependent on the model used. For this study the jacket model is used. The study is made for two cases: one where gradients are determined using a single cpu core, and another where two cpu cores are used. During one iteration one call is made to the structural analysis to determine the damage, while 14 calls to the structural analysis is made to compute the gradients by the forward FD. The stress calculation is called 11,250 times since 750 load sample points is used, which corresponds to the 15 calls to the structural analysis since $11,250/750 = 15$. The results of the two cases are shown on Figure I.1.

The main conclusion is that 88% of the calculation time is spent on computing the gradients, if the gradients are calculated using parallel computing. 12% of the calculation time is spent on computing the damage,

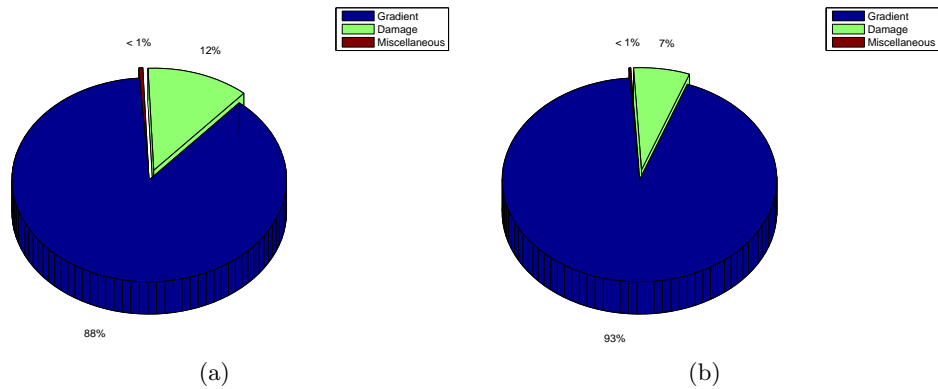


Figure I.1: (a) Calculation time spent on different processes for parallel cpu. (b) Calculation time spent on different processes for single cpu.

while less than a half percent is spent on solving the optimization problem. When using a single cpu, 93% of the time is spent computing the gradients, while 7% is spent on computing the damage. Less than 0.2% is spent on solving the optimization problem for this case. The stress calculation used in the determination of the gradients and the damage uses 62% of the total execution time.

It can be concluded, that the major part of the calculation time is spent on computing the gradients. Thus, this is the area with the largest potential for reducing the computational time. It is determined, that the computational time was reduced by 46% by the using of two cpu cores instead of one. Thus, it can be concluded that it may be beneficial to use parallel computing when determining the gradients even though some time is spent on establishing the connection to multiple cpu cores. It would be beneficial to rewrite the scripts for the stress calculation to allow for parallel computing since it is called many times for even a small number of load- and cross sectional sample points.

It should be noted, that the number of sub-function calls and the amount of data, which must be stored, is significant even for small models and load spectra.

I.0.4 Calculation Time in DSA

In this section the calculation time between the different DSA methods is investigated further, since it is determined, that the DSA is the most time consuming part of the optimization. The example of Figure 8.3 is used. Six

tip loads are applied and 750 load sample points are used. The distribution of time spent for the different methods can be seen on Figure I.2.

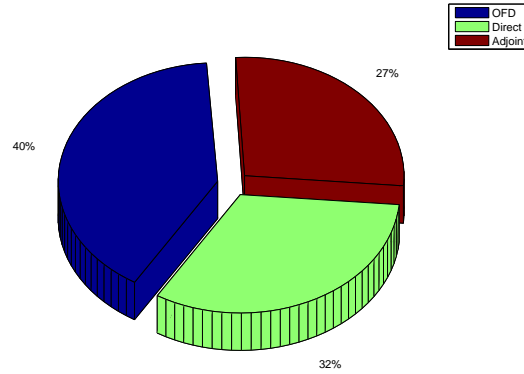


Figure I.2: Comparison between calculation times using the DDM, AM, and central OFD methods.

Figure I.2 is made by calculating the DSA by a central FD scheme, a DDM, and an AM. The combined time of calculating the three is 100%. Thus, the calculation time of the various methods may be compared by Figure I.2.

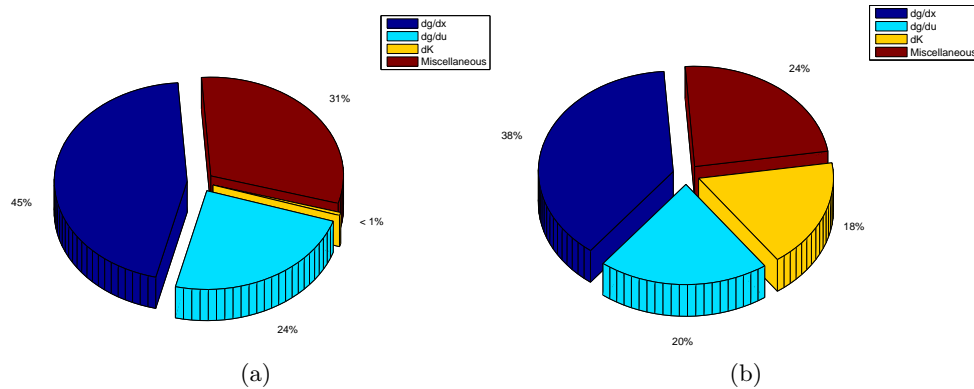


Figure I.3: Execution time spent on different analytical methods for DSA: (a) AM. (b) DDM.

A further comparison of the analytical methods are made on Figure I.3. For the adjoint method the derivative of the stiffness matrix is called 400 times (10 design variables and 40 cross sectional sample points), while it is called 17,600 times for the direct method. $\frac{\partial g_k}{\partial x_j}$ and $\frac{\partial g_k}{\partial U}$ are called 1760 times for both methods. The most severe differences are the calculations in the matrix

operations in the end of both methods. The loop in the end of the DDM, where the derivative of the stiffness matrix is used several times are very time consuming compared to the determination of the $\bar{\lambda}$ in the AM. This is also the reason why the AM is faster than the DDM for the present example even though the number of cross sectional sample points are 40 and the number of design variables are 10 (if both the gradients for the thickness and diameter sensitivities are computed). It can be concluded, that one of the main hurdles in the analytical DSA is the huge amount of data storage since large matrices are generated through the approach.

Appendix J

Parametric Study of Stress Constraints

An example is defined in order to examine if a simple optimization using a stress constraint yields similar results as an optimization using the fatigue constraint. This example uses a static stress constraint for the optimization. Thus, an equivalent load is determined from the non-proportional load series shown on Figure 10.1a. By the use of the equivalent amplitude approach in section 5.3.3 an equivalent static force is determined to 1542.7 N and applied to the cantilevered beam model as a P_y force. It should be noted that this approach is only applicable since it is a simple cantilevered beam. The stress constraint is normalized w.r.t. yield stress, $\sigma_y = 883$ MPa, and the results of the parametric study can be seen on Figure J.1.

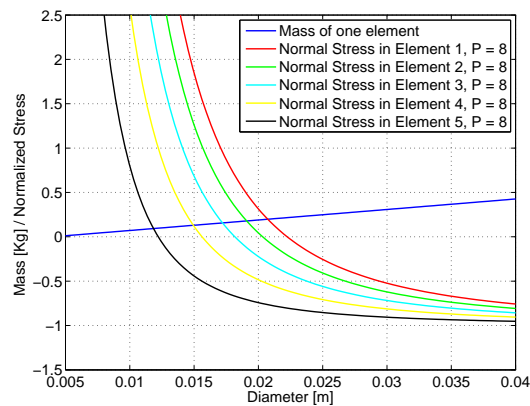


Figure J.1: Parametric study of the stress distribution for $P_y = 1542.7$ N and the stress constraint normalized w.r.t. σ_y .

Figure J.1 can be compared with Figure 10.1b. It can be seen that the damage constraint is steeper than the stress constraint. Hence, it might be easier for an optimization w.r.t. stresses to reach an optimum within the feasible domain. Furthermore, this optimization gives a design with lower diameters than for the optimization with the damage as a constraint. This may be due to mean stress effects since these are neglected in the current example, and due to a high yield stress. Thus, it can be concluded, that an optimization with static stresses as a constraint does not yield a design similar to the optimization using fatigue constraints.

Appendix K

Deficiencies in the Current Analytical DSA

The analytical DSA is in its current state capable of providing reliable sensitivity results for a number of various load cases and load combinations. However, excessive testing has showed, that unreliable results are obtained for some load scenarios as well. One example of a load scenario, which is causing problems in the analytical DSA, is shown in the following. The deficiencies in the DSA may correlate to the assumptions made in the bookkeeping. This is treated further in the discussion in Chapter 12.

K.1 Different Spectra

The simple cantilevered beam model introduced in section 8.4.1 is used for the examination. A number of various load spectra will be applied to the tip end of the prismatic beam model. As seen in section 8.4, both the DDM and the AM are capable of determining reliable sensitivities for a non-proportional load series applied to all tip loads. However, this may change whenever different load series are applied to the different applied loads as will be shown. As in section 8.4, a comparison between the sensitivities obtained using a DDM, an AM, and a central FD scheme will be used for the examination.

This test will use two different spectra for the forces P_y and P_z . The cantilevered beam model of Figure 8.3 is used for the examination. The spectra can be seen in Figure K.1.

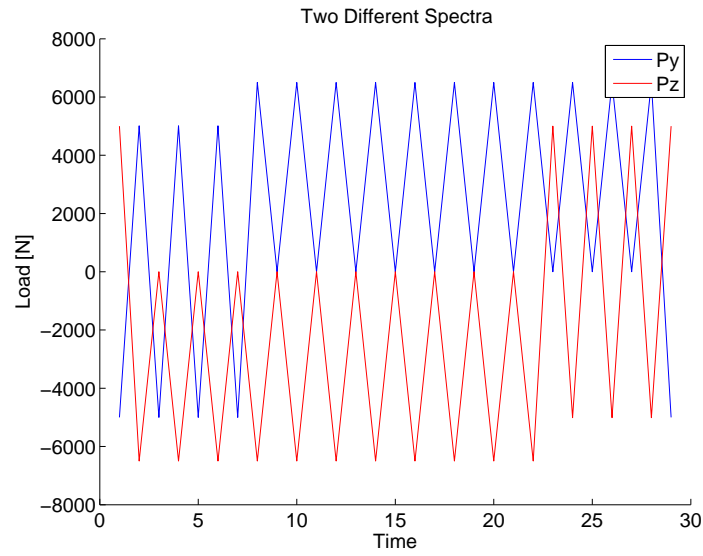


Figure K.1: Two different load series applied as P_y and P_z .

It is seen from Figure K.1, that the used spectra are not just a scale of the same spectra as it is the case for the example in section 8.4, but two different spectra. The percentage deviation between the analytical methods and the central FD approximation can be seen in Table K.1 for the DDM and Table K.2 for the AM.

		Diameter				Thickness			
Element 1	Node 1	0.6%				0.6%			
		-0.2%				-0.2%			
		2.1%				2.1%			
		29.3%				29.3%			
	Node 2	0.5%				0.5%			
		2.6%				2.6%			
		1.8%				1.8%			
		26.0%			26.0%				
Element 2	Node 1		0.5%				0.5%		
			2.6%				2.6%		
			1.8%				1.8%		
			26.0%				26.0%		
	Node 2		0.4%				0.4%		
			5.4%				5.4%		
			1.4%				1.4%		
		22.8%				22.8%			

Table K.1: The percentage deviations between sensitivities obtained using the DDM and the central FD scheme.

		Diameter				Thickness			
Element 1	Node 1	0.6%				0.6%			
		-0.2%				-0.2%			
		2.1%				49.2%			
		29.3%				29.3%			
	Node 2	0.5%				0.5%			
		2.6%				2.6%			
		1.8%				88.9%			
		26.0%				26.0%			
Element 2	Node 1	0.5%				0.5%			
		2.6%				2.6%			
		1.8%				36.9%			
		26.0%				26.0%			
	Node 2	0.4%				0.4%			
		5.4%				5.4%			
		1.4%				9.6%			
		22.8%				22.8%			

Table K.2: The percentage deviations between sensitivities obtained using the AM and the central FD scheme.

From Table K.1 it is seen that an unacceptable percentage deviation is introduced in the fourth cross sectional sample point for the case of two different load series. Due to the placement of the four sample points on the cross section, the inaccuracy in the fourth cross sectional sample points seems to be related to the P_z force. This is supported by the observation made when reversing the sign on the load series applied to P_z which switches the position of the inaccuracy from sample point four to sample point two. Thus, either the combination of the two different load series, or the applied P_z load series alone introduce the seen inaccuracies.

Removing the P_y force from the present example will reveal whether the load series used for P_z alone will introduce an error in the analytical calculations. All inaccuracies on the diameter sensitivities are however removed when P_y is removed, and only P_z is applied. This suggests that the high percentage deviations are not caused by the use of a bad choice of load spectrum but from the combination of different non-proportional spectra.

It can be seen from a comparison between Tables K.1 and K.2 that the two analytical methods calculate the same diameter sensitivities. However, a much larger percentage deviation is seen for the AM, Table K.2, for some of the thickness sensitivities. A percentage deviation of up to 89% is seen in some of the thickness sensitivities, which is unacceptable. Note, that a similar inaccuracy is not seen in the diameter sensitivities. The tendency seems to be, that the inaccuracies in the thickness sensitivities of the AM is somehow linked to

the P_y force, since only cross section sample point three seems to be affected. Reversing the applied P_y removes the inaccuracy in sample point three and introduces an inaccuracy in sample point one instead. Note, the inaccuracy in thickness sensitivities was not seen for the cantilevered beam example set up in section 8.4.

Through this appendix the current deficiencies in the analytical methods for the DSA have been highlighted. Two major deficiencies were shown by the use of two non-proportional load series for a P_y and P_z tip load. It was seen how the AM introduced some inaccuracies in the thickness sensitivity analysis in one of the four cross sectional sample points. These inaccuracies were not seen in the DDM.

Both the DDM and the AM yielded equal diameter sensitivities. However, for both methods an unacceptably large inaccuracy of approximately 30% was seen in one of the four cross sectional sample points. The inaccuracy seemed to be linked to the P_z force. However, an analysis using only an applied P_z force showed no inaccuracies.

Thus, in its current state, the analytical DSA is not capable of providing acceptable results for the DSA whenever different load series must be applied for the different forces. Furthermore, care should be taken when the AM is used for determination of the thickness sensitivities, or the DDM should always be preferred.

A further discussion of the causes for the current deficiencies is made in Chapter 12.

Appendix L

Optimization of Beam with Six Applied Loads

A second beam example, much like the example introduced in section 10.1, is set up. Note, the gradients will be determined using the analytical DSA. However, in this example six loads, P_x , P_y , P_z , M_x , M_y , and M_z are all applied at the tip of the beam. Again, the model introduced in Figure 8.3 is used for the optimization. The cross sectional sample point with the maximum damage is chosen for each element. The initial diameter is set to 0.11 m and the initial thickness is set to 0.004 m. Thus, the initial weight of the beam is determined to approximately 6.3 kg. The load spectra seen in Figure L.1a is applied to all six loads and changes to the fatigue constraints as a function of the diameter can be seen on Figure L.1b.

The optimum solution, towards which the SLP algorithm should converge, is again seen as the diameters for which the constraint function value in the given element equals zero. Note, the length of the beam is maintained at 0.6 m which means the 1/10 length-diameter ratio is not maintained in the current example. Thus, slight inaccuracies can be expected in the stress calculations. The adaptive move limit strategy for this problem is defined as:

- For a change in constraint function value larger than 5%, decrease the move limit by 80%.
- For a change in constraint function value less than 1%, increase the move limit by 10%.

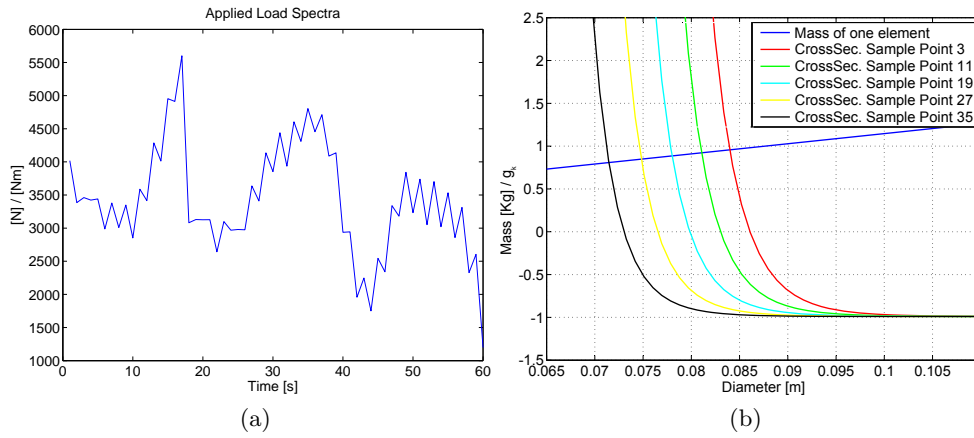


Figure L.1: (a) The load spectra used for all six applied loads in the second optimization problem. (b) The maximum constraint function value in each of the five elements and the mass of a single element.

Note, the move limit is set to a low initial value due to the highly non-linear behavior of the optimization problem, cf. Figure L.1b. The solution obtained using the SLP algorithm may be seen in Table L.1.

Element	Diameter, [m]	g_k
1	0.087	-0.18
2	0.084	-0.19
3	0.081	-0.20
4	0.077	-0.21
5	0.074	-0.22

Table L.1: Optimized solution for the cantilevered beam model with six applied tip loads.

A comparison between Figure L.1b and Table L.1 reveals that the SLP algorithm is stopped near the expected result. As for the example in section 10.1, the optimization algorithm converges before the bounds on each fatigue constraint is reached, due to the very small design changes near the bounds. As expected, the diameters of the elements in the beam must be significantly larger when six loads are applied than when only a single load is applied. The weight of the optimum design is approximately 4.5 kg, resulting in an overall reduction of nearly 30%. The lower weight reduction for this example compared to the example in section 10.1 is a result of the starting point being closer to the optimized design.

Appendix M

Generalized Mean Methods

This appendix serves as a support for section 10.1.3, and it contains a parametric study of the beam according to the damage estimation from the choice of p-value.

M.1 Parametric Study of Generalized Mean Method

A parametric study of the influence of the p-value is performed for $p = 1, 2, 4, 8, 15, 30$ using a cantilevered beam with the spectrum shown on Figure 10.1a applied as a P_y force. In Figures M.1a to M.1f the constraint function value is plotted as a function of diameter with a fixed thickness of 0.004 m. Note, that the results of the figures agrees well with the result of Table M.1. Furthermore, it can be seen, that for the higher p-values a larger diameter is needed in order to keep the damage at the same level. This agrees with the theory presented in section 9.2.2 since a larger p-value has shown to result in a larger weighted damage.

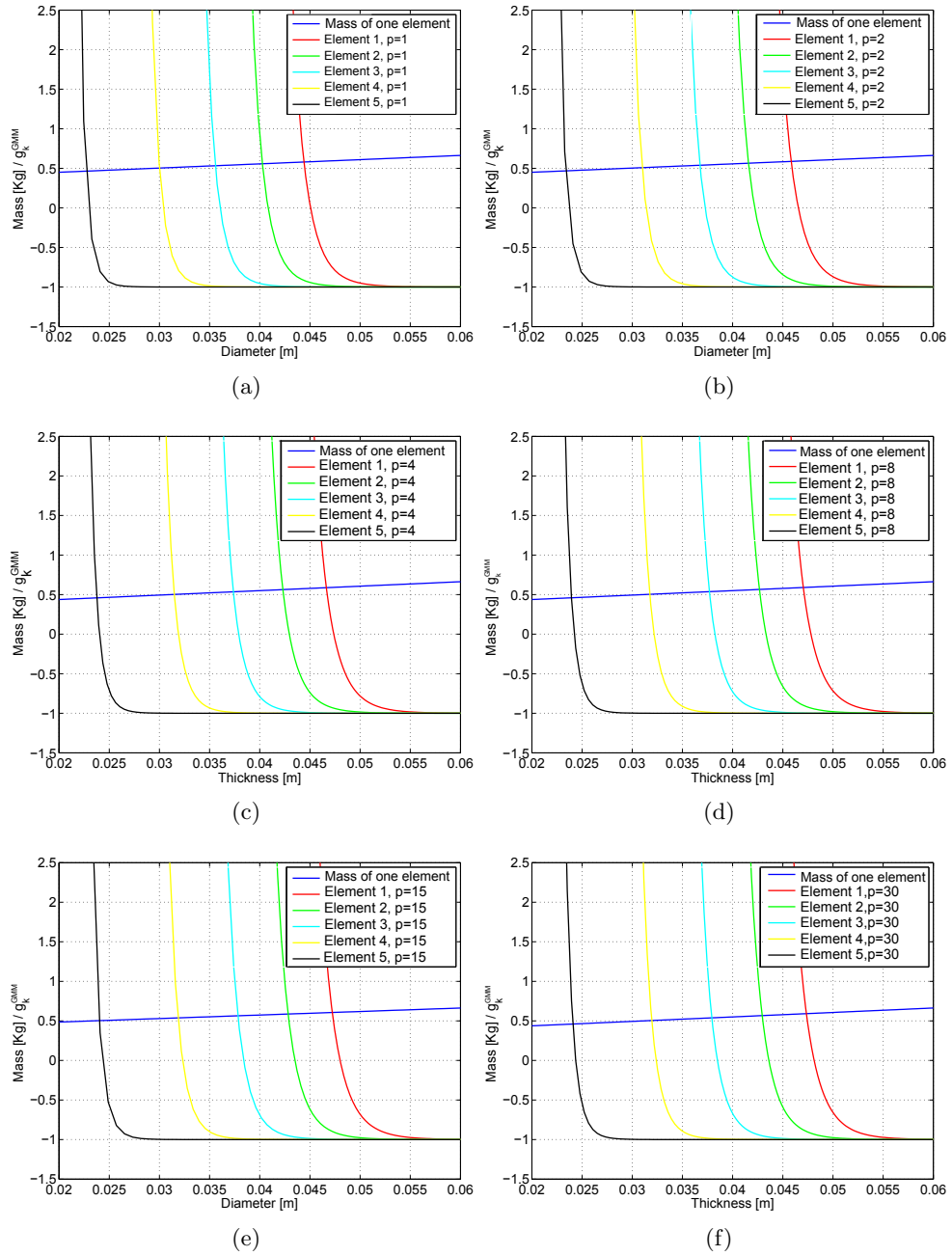


Figure M.1: Parametric study of the damage constraint as a function of diameter for p -values of: (a) $p=1$, (b) $p=2$, (c) $p=4$, (d) $p=8$, (e) $p=15$, and (f) $p=30$. The thickness is fixed to 0.004 m.

M.2 Optimization Results

Table M.1 contain the optimization results for the beam in section 10.1.3.

p	<i>I</i>	Time, [s]	Constraint function					Diameter				
1	61	568	-0.60	-0.62	-0.61	-0.64	-0.20	0.05	0.04	0.04	0.03	0.02
2	65	603	-0.59	-0.61	-0.63	-0.50	-0.69	0.05	0.04	0.04	0.03	0.02
3	65	598	-0.58	-0.60	-0.61	-0.65	-0.69	0.05	0.04	0.04	0.03	0.02
4	63	594	-0.57	-0.60	-0.61	-0.66	-0.69	0.05	0.04	0.04	0.03	0.02
5	64	588	-0.58	-0.60	-0.62	-0.65	-0.67	0.05	0.04	0.04	0.03	0.02
6	64	586	-0.57	-0.59	-0.61	-0.64	-0.69	0.05	0.04	0.04	0.03	0.03
7	63	579	-0.56	-0.59	-0.61	-0.63	-0.69	0.05	0.04	0.04	0.03	0.02
8	64	609	-0.57	-0.57	-0.60	-0.66	-0.68	0.05	0.04	0.04	0.03	0.02
9	64	588	-0.56	-0.59	-0.62	-0.65	-0.69	0.05	0.04	0.04	0.03	0.03
10	63	580	-0.57	-0.59	-0.62	-0.65	-0.69	0.05	0.04	0.04	0.03	0.03
11	63	577	-0.56	-0.59	-0.61	-0.65	-0.68	0.05	0.04	0.04	0.03	0.03
12	62	568	-0.57	-0.59	-0.61	-0.65	-0.68	0.05	0.04	0.04	0.03	0.03
13	62	568	-0.56	-0.58	-0.61	-0.64	-0.69	0.05	0.04	0.04	0.03	0.03
14	62	568	-0.56	-0.59	-0.61	-0.65	-0.67	0.05	0.04	0.04	0.03	0.03
15	64	595	-0.57	-0.58	-0.61	-0.63	-0.68	0.05	0.04	0.04	0.03	0.03
30	64	588	-0.57	-0.61	-0.60	-0.64	-0.68	0.05	0.05	0.04	0.03	0.03

Table M.1: Results obtained by optimization process with different p-values for the gradient and the constraint function.

Appendix N

CD

The enclosed CD contains:

- A DSA Test example
- The optimization framework for jacket structure
- The used rainflow count script
- The ANSYS model of jacket structure
- The report in PDF-format
- The used literature